Drift: Drude model

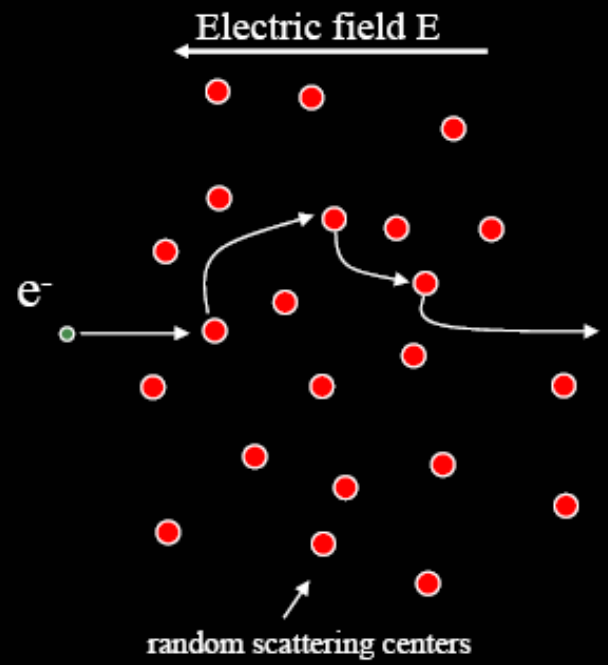

$$F = ma$$

$$eE = m\frac{\partial v}{\partial t}$$

$$v_{avg} = \underbrace{\frac{e\tau}{m}}_{\mu} E$$

$$j = nev_{avg} = \underbrace{\frac{ne^2\tau}{m}}_{\sigma} E$$

$$m\frac{\partial}{\partial t}\langle\vec{v}\rangle = q\vec{E} - \gamma\langle\vec{v}\rangle$$

$$\sigma(\omega) = \frac{\sigma_0}{1 + i\omega\tau}$$

AC Dielectric Response

$$\varepsilon_m = 1 - \frac{\omega_p^2}{\omega^2}$$

Plasma frequency

polarizability of a small metal sphere with dielectric function $\varepsilon(\lambda)$

$$\alpha = R^3 \frac{\varepsilon - 1}{\varepsilon + 2}\,.$$

$$\varepsilon = \varepsilon_\mathrm{b} + 1 - \frac{\omega_\mathrm{p}^2}{\omega^2 + \mathrm{i}\omega\gamma}\,,$$

$$\alpha = \frac{R^3(\varepsilon_\mathrm{b}\omega^2 - \omega_\mathrm{p}^2) + i\omega\gamma\varepsilon_\mathrm{b}}{[(\varepsilon_\mathrm{b} + 3)\omega^2 - \omega_\mathrm{p}^2] + i\omega\gamma(\varepsilon_\mathrm{b} + 3)}\,.$$

$$\omega_\mathrm{R} = \frac{\omega_\mathrm{p}}{\sqrt{\varepsilon_\mathrm{b}+3}} \qquad\qquad \gamma(\varepsilon_\mathrm{b} + 3)$$

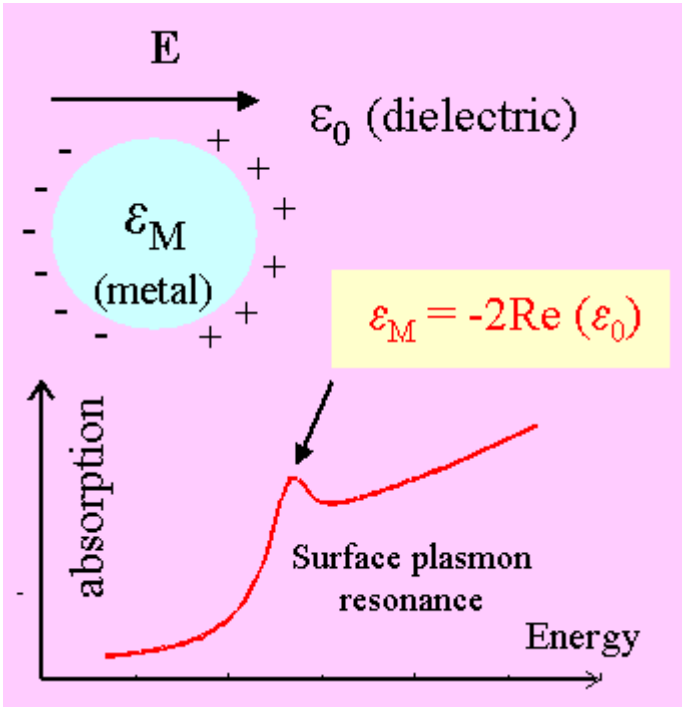

$$\varepsilon_{eff} = \varepsilon_0 + 3N\varepsilon_0 \frac{\varepsilon_M - \varepsilon_0}{\varepsilon_M + 2\varepsilon_0}$$

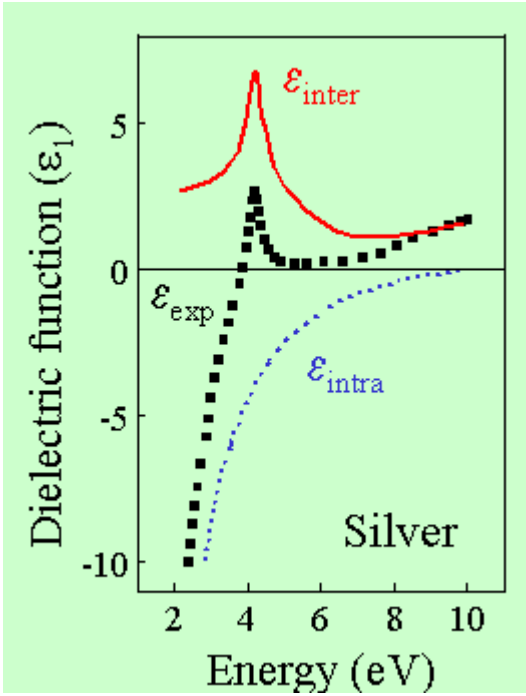

Surface Plasmon

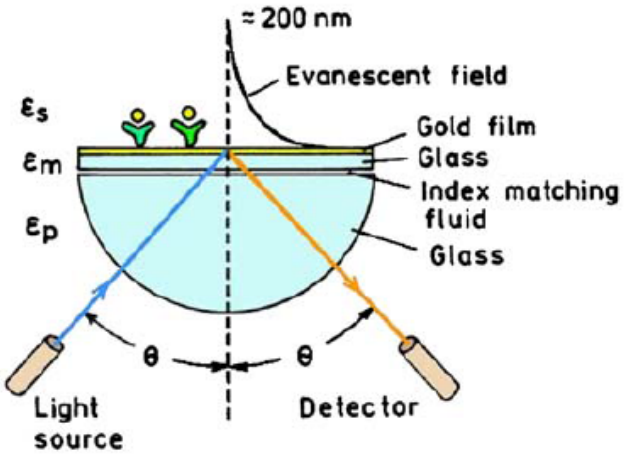

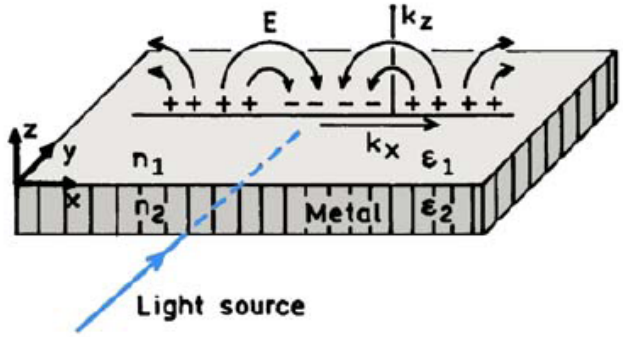

Figure 3. Schematics of an SPR experiment (top) and of the light-induced surface plasmons (bottom).

(b)

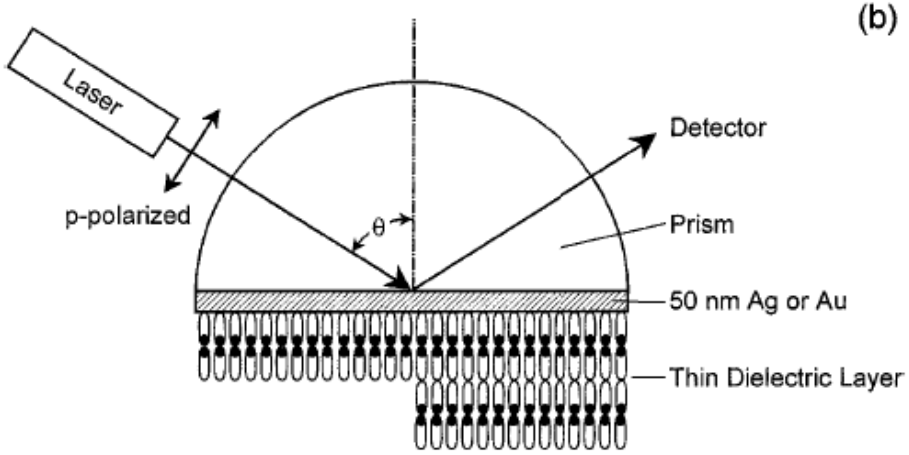

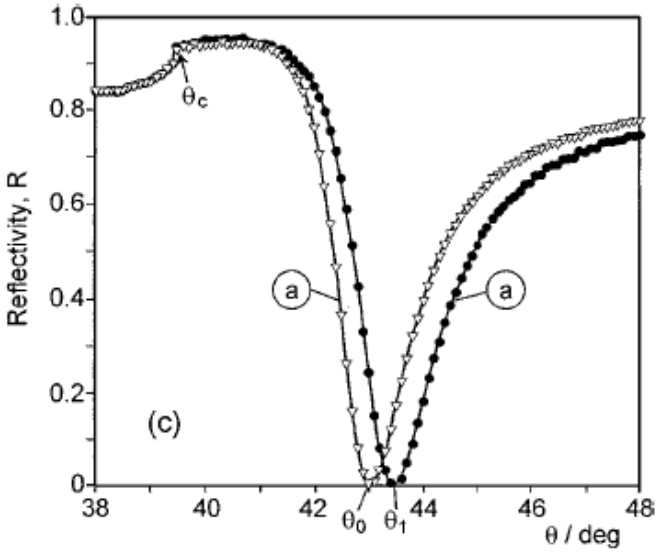

Biomolecular Binding in Real Time

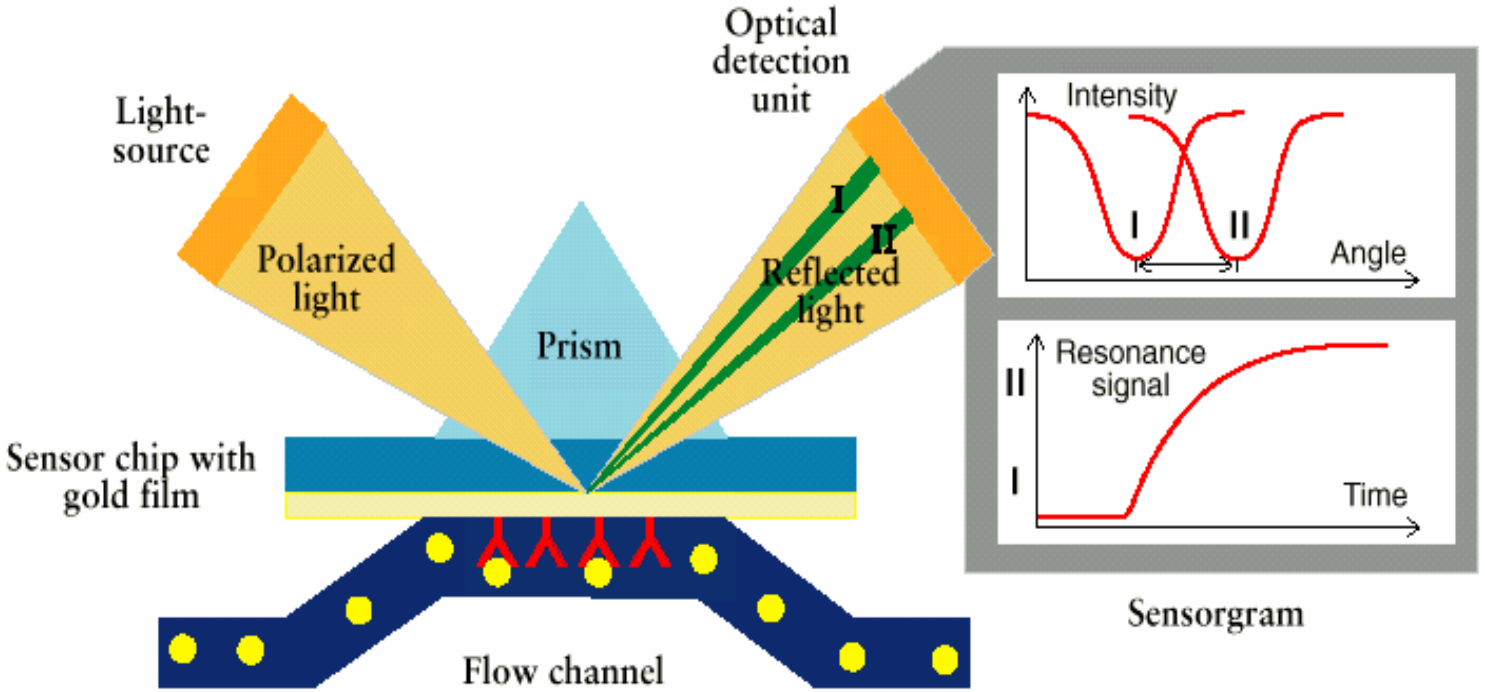

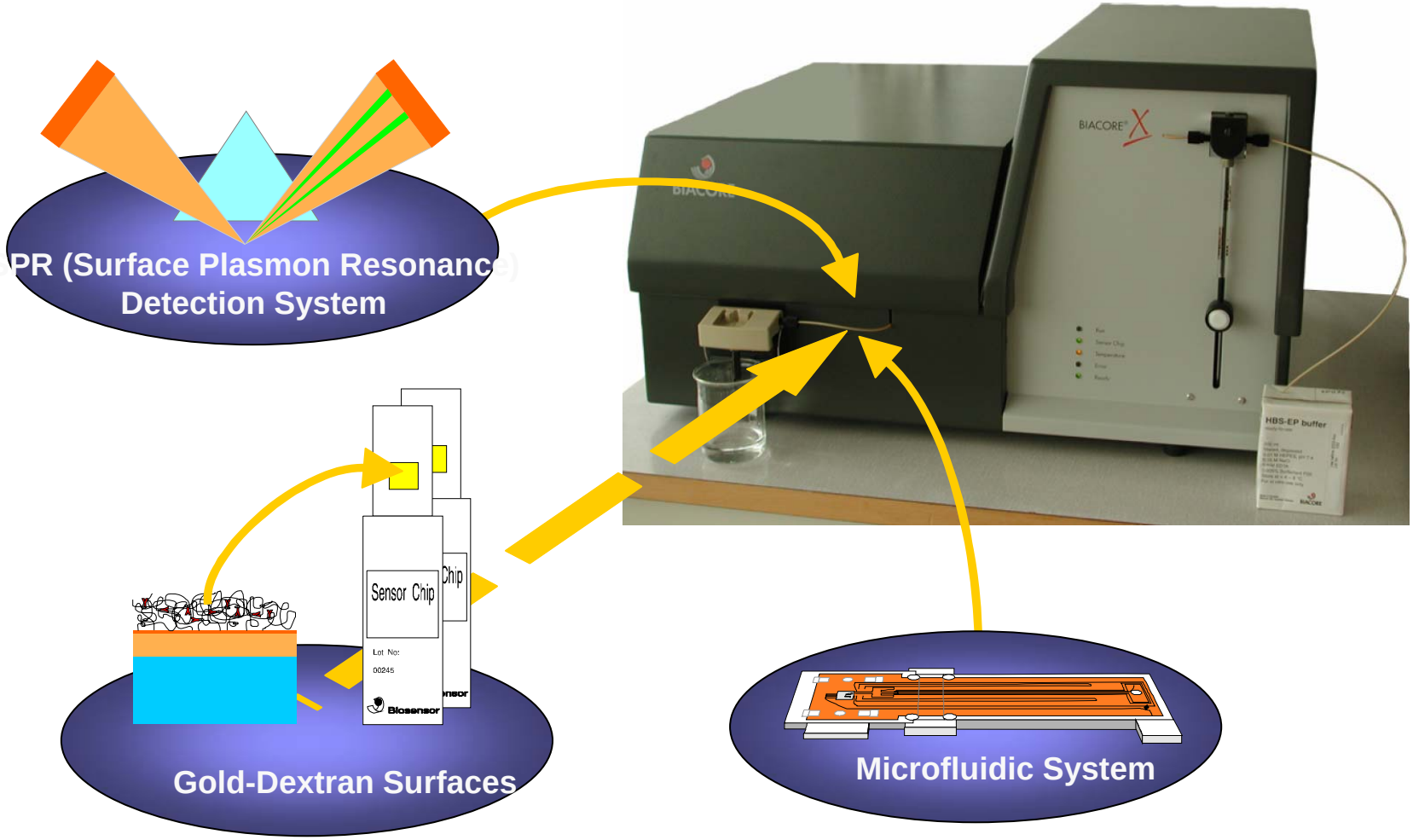
SPR (Surface Plasmon Resonance)
Detection System
BIACORE X
HBS-EP buffer
Sensor Chip
Lot No:
00245
Biosensor
Gold-Dextran Surfaces
Microfluidic System

SPR Imaging Apparatus

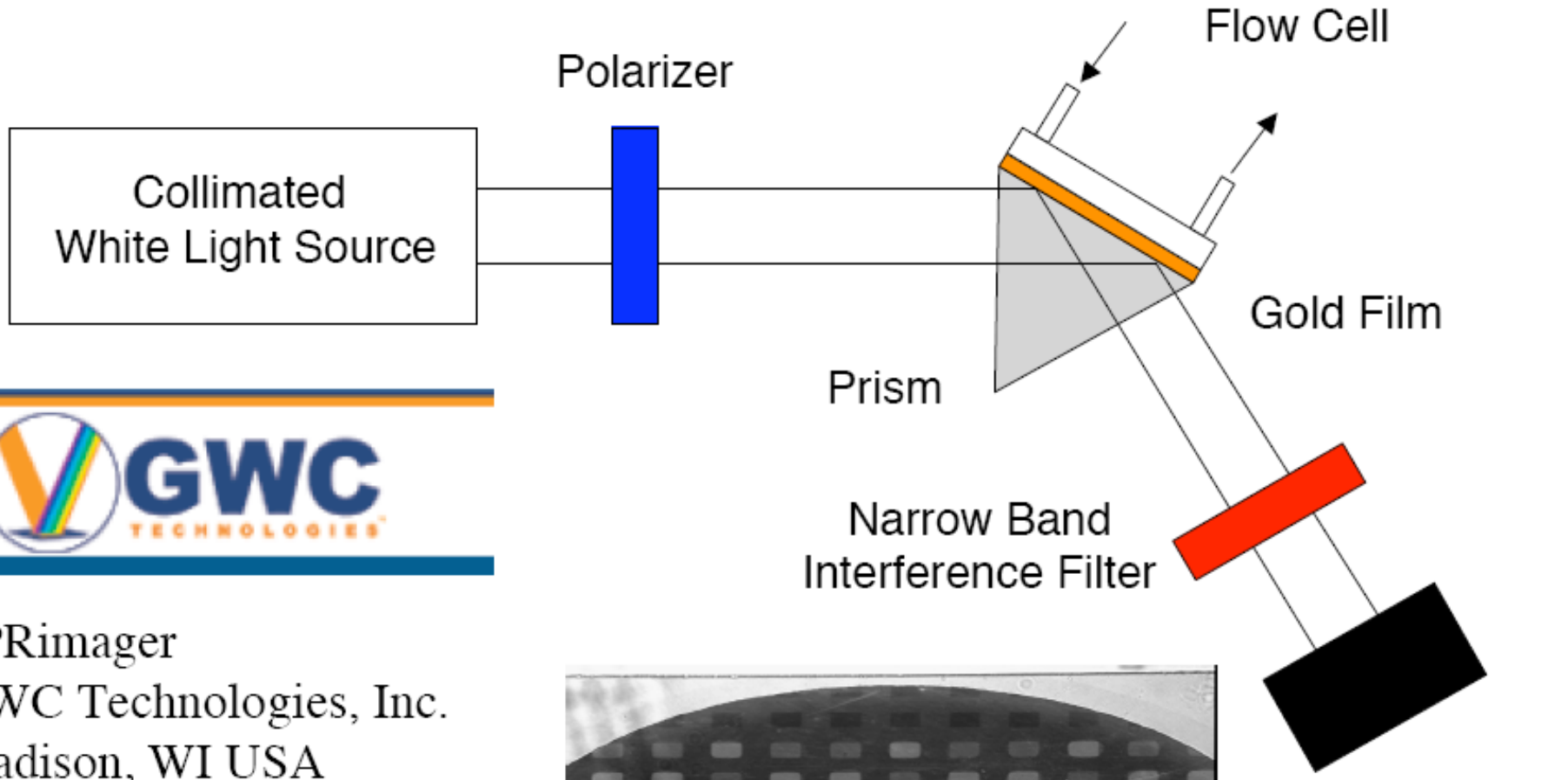

SPRimager
GWC Technologies, Inc.
Madison, WI USA

www.gwctechnologies.com

Raw Image

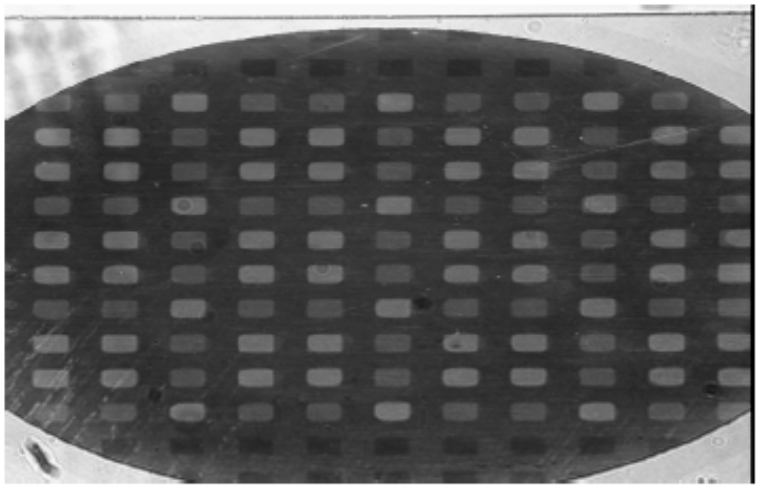

UCIrvin
University of California, I

Localized Plasmon

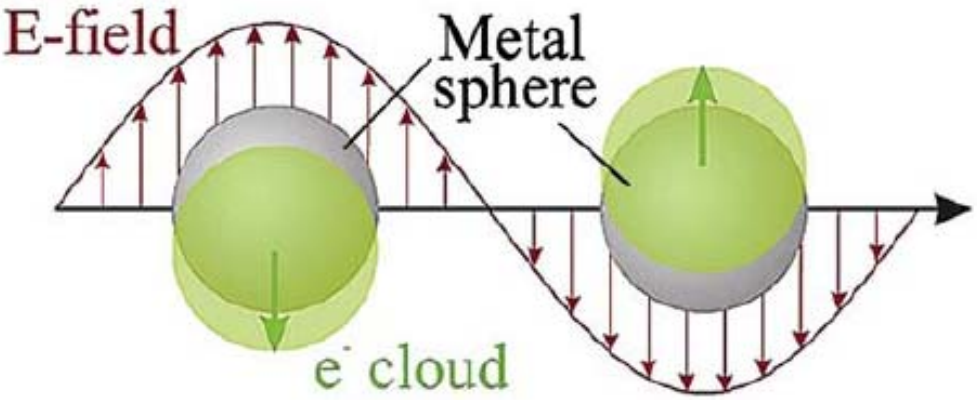

Figure 6. Schematic of plasmon oscillation for a sphere. From [39].

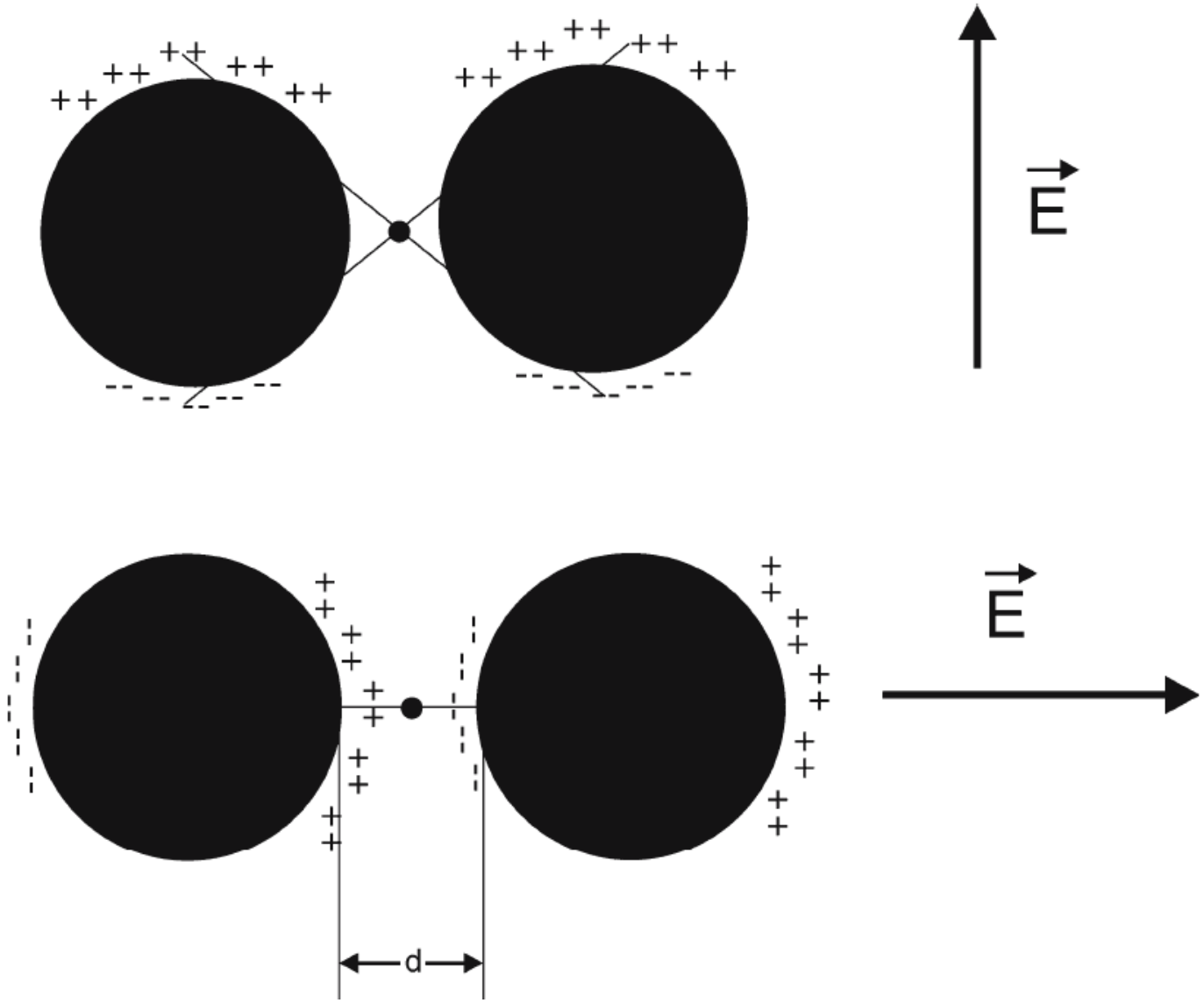
E
E
d

field enhancement

$E_s = gE_0$, where E_0 is the magnitude of the incident field

$$E_R \propto \alpha_R E_s \propto \alpha_R g E_0$$

$$E_{SERS} \propto \alpha_R g g' E_0$$

$$I_{SERS} \propto |\alpha_R|^2 |gg'|^2 I_0$$

$$g \cong g'$$

$$|E_L|^4 = |g|^4$$

Probing Single Molecules and Single Nanoparticles by Surface-Enhanced Raman Scattering

SCIENCE • VOL. 275 • 21 FEBRUARY 1997

Shuming Nie* and Steven R. Emory

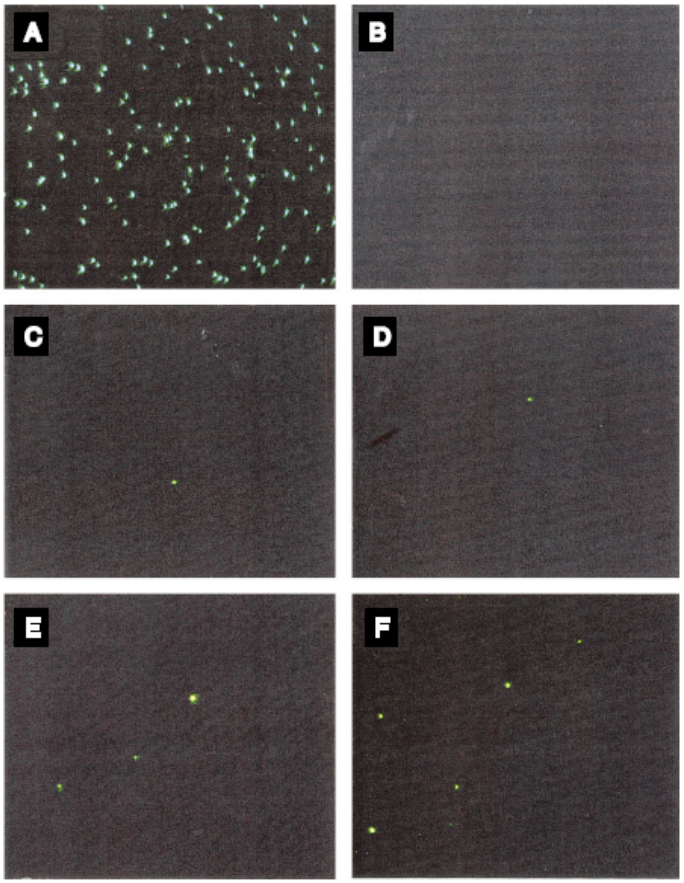

Fig. 1. Single Ag nanoparticles imaged with evanescent-wave excitation. Total internal reflection of the laser beam at the glass-liquid interface was used to reduce the laser scattering background. The instrument setup for evanescent-wave microscopy was adapted from Funatsu *et al.* (*11*). The images were directly recorded on color photographic film (ASA-1600) with a 30-s exposure by a Nikon 35-mm camera attached to the microscope. (**A**) Unfiltered photograph showing scattered laser light from all particles immobilized on a polylysine-coated surface. (**B**) Filtered photographs taken from a blank Ag colloid sample (incubated with 1 mM NaCl and no R6G analyte molecules). (**C**) and (**D**) Filtered photographs taken from a Ag colloid sample incubated with 2×10^{-11} M R6G. These images were selected to show at least one Raman scattering particle. Different areas of the cover slip were rapidly screened, and most fields of view did not contain visible particles. (**E**) Filtered photograph taken from Ag colloid incubated with 2×10^{-10} M R6G. (**F**) Filtered photograph taken from Ag colloid incubated with 2×10^{-9} M R6G. A high-performance bandpass filter was used to remove the scattered laser light and to pass Stokes-shifted Raman signals from 540 to 580 nm (920 to 2200 cm^{-1}). Continuous-wave excitation at 514.5 nm was provided by an Ar ion laser. The total laser power at the sample was 10 mW. Note the color differences between the scattered laser light in (A) and the red-shifted light in (C) through (F).

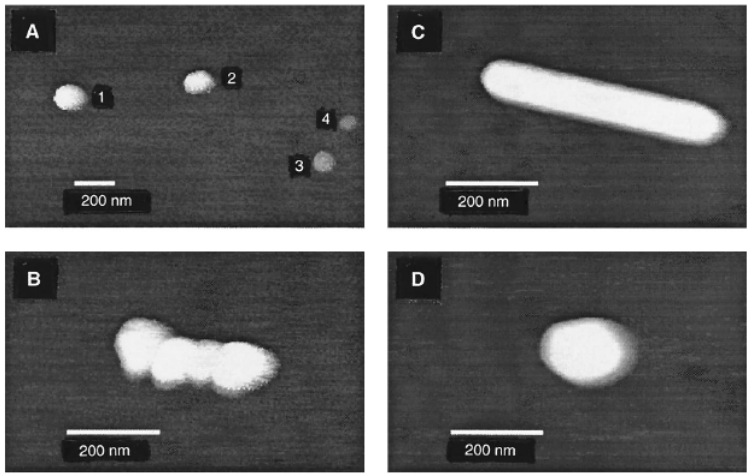

Fig. 2. Tapping-mode AFM images of screened Ag nanoparticles. (**A**) Large area survey image showing four single nanoparticles. Particles 1 and 2 were highly efficient for Raman enhancement, but particles 3 and 4 (smaller in size) were not. (**B**) Close-up image of a hot aggregate containing four linearly arranged particles. (**C**) Close-up image of a rod-shaped hot particle. (**D**) Close-up image of a faceted hot particle.

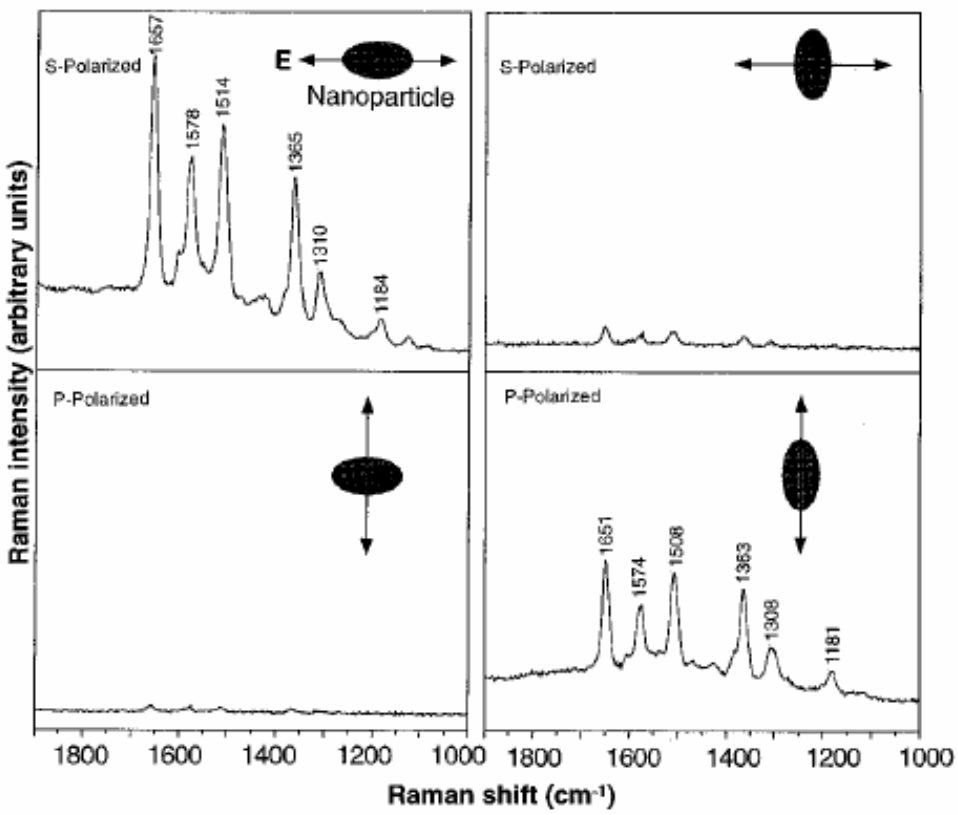

Fig. 3. Surface-enhanced Raman spectra of R6G obtained with a linearly polarized confocal laser beam from two Ag nanoparticles. The R6G concentration was 2×10^{-11} M, corresponding to an average of 0.1 analyte molecule per particle. The direction of laser polarization and the expected particle orientation are shown schematically for each spectrum. Laser wavelength, 514.5 nm; laser power, 250 nW; laser focal radius, ~250 nm; integration time, 30 s. All spectra were plotted on the same intensity scale in arbitrary units of the CCD detector readout signal.

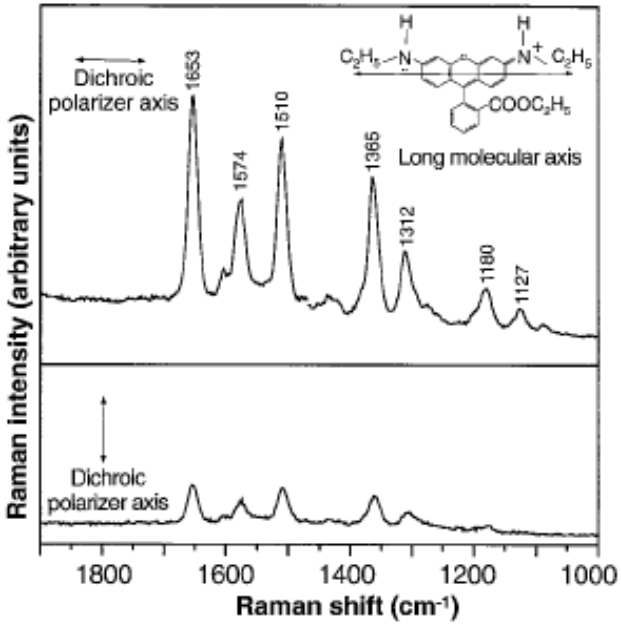

Fig. 4. Emission-polarized surface-enhanced Raman signals of R6G observed from a single Ag nanoparticle with a polarization-scrambled confocal laser beam. A dichroic sheet polarizer was rotated 90° to select Raman scattering signals polarized parallel (upper spectrum) or perpendicular (lower spectrum) to the long molecular axis of R6G. (**Inserts**) Structure of R6G, the electronic transition dipole (along the long axis when excited at 514.5 nm), and the dichroic polarizer orientations. Other conditions as in Fig. 3.

troscopic signatures of adsorbed molecules. For single rhodamine 6G molecules adsorbed on the selected nanoparticles, the intrinsic Raman enhancement factors were on the order of 10^{14} to 10^{15}, much larger than the ensemble-averaged values derived from conventional measurements. This enormous enhancement leads to vibrational Raman signals that are more intense and more stable than single-molecule fluorescence.

Electromagnetic contributions to single-molecule sensitivity in surface-enhanced Raman scattering

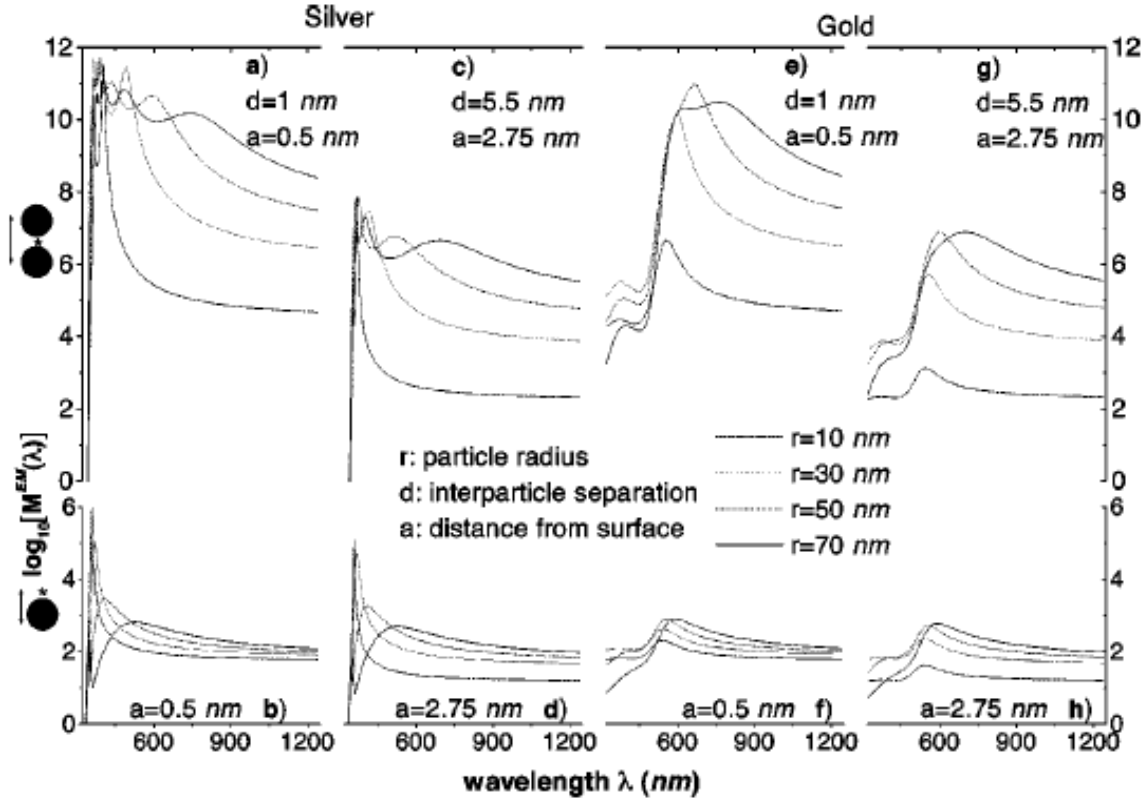

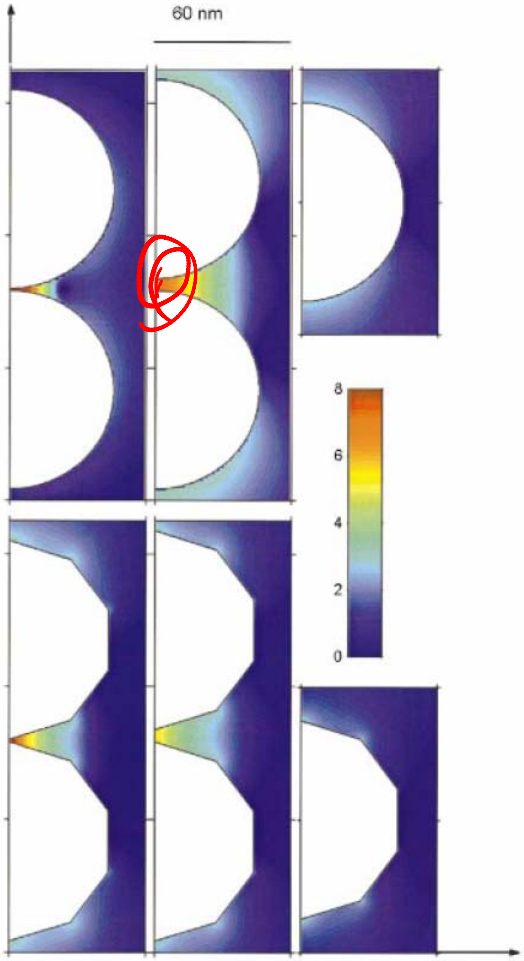

FIG. 3. (Color) EM-enhancement factor M^{EM} at a cross section through six different silver particle configurations. The wavelength of the incident field is $\lambda = 514.5$ nm with vertical polarization. The left-hand column illustrates the EM enhancement for dimer configurations of two spheres (top) and two polygons (bottom) with a separation of 1 nm. The middle column shows the same situation, but with a separation distance of 5.5 nm. The right-hand column shows the case of an isolated single particle. All particles share a common largest dimension of 90 nm. Note that the color scale from dark blue to dark red is logarithmic, covering the interval $10^0 < M^{EM} < 10^8$. Regions with enhancement outside this interval are shown in dark blue and dark red, respectively.

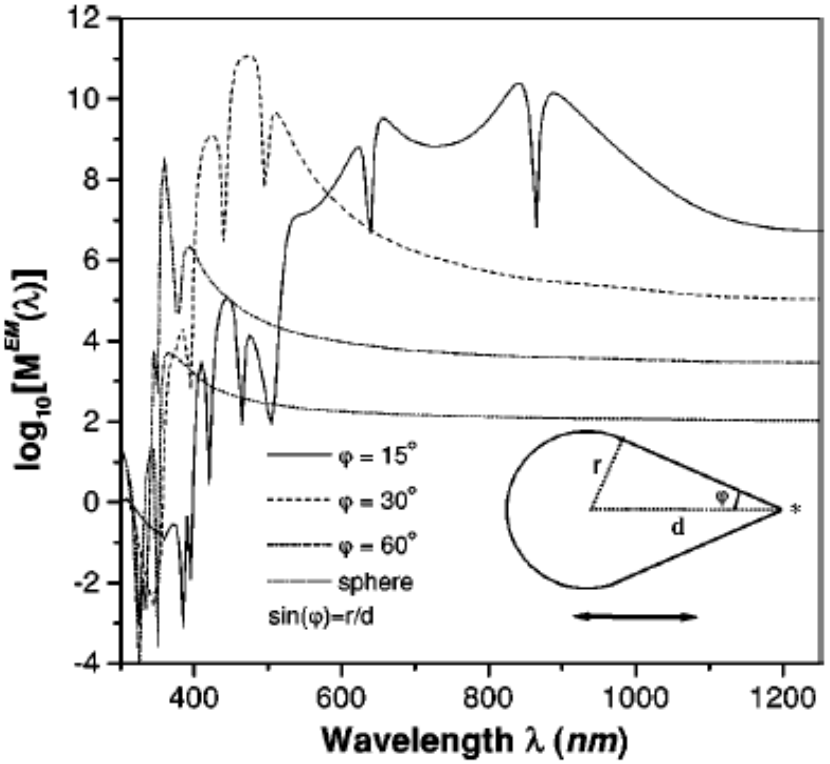

FIG. 5. EM-enhancement factor for a rotationally symmetric silver droplet as a function of the angle defining the opening edge ϕ. The field is polarized parallel to the axis of the droplet and the evaluation position (star) is located 0.5 nm outside the tip. As the droplet becomes sharper the enhancement increases several orders of magnitude.

Nanosphere Arrays with Controlled Sub-10-nm Gaps as Surface-Enhanced Raman Spectroscopy Substrates

J. AM. CHEM. SOC. 2005, *127*, 14992−14993

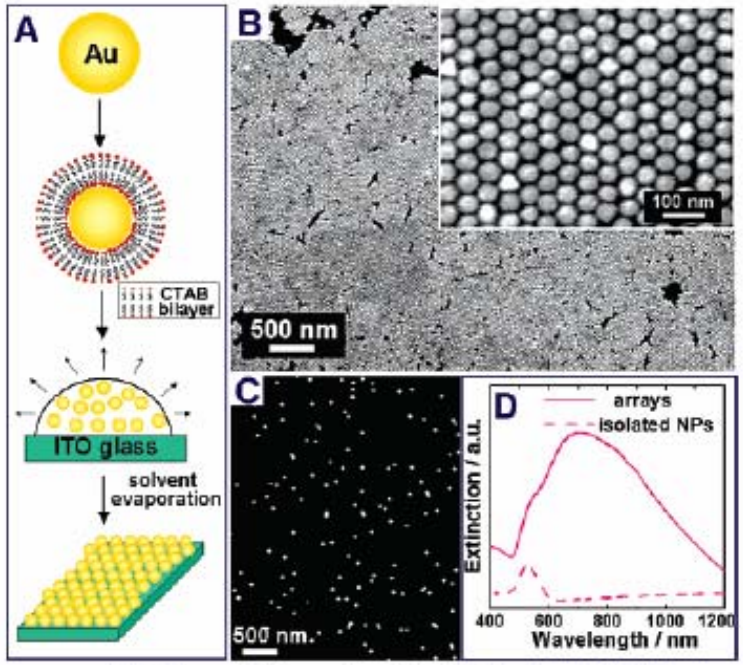

Figure 1. (A) Schematic illustration of the fabrication of sub-10-nm gap Au NP arrays. (B) SEM image of the arrays. (C) SEM image of monolayer of isolated Au NPs on ITO glass. (D) Vis−NIR extinction spectrum of the monolayer of isolated Au NPs and arrays.

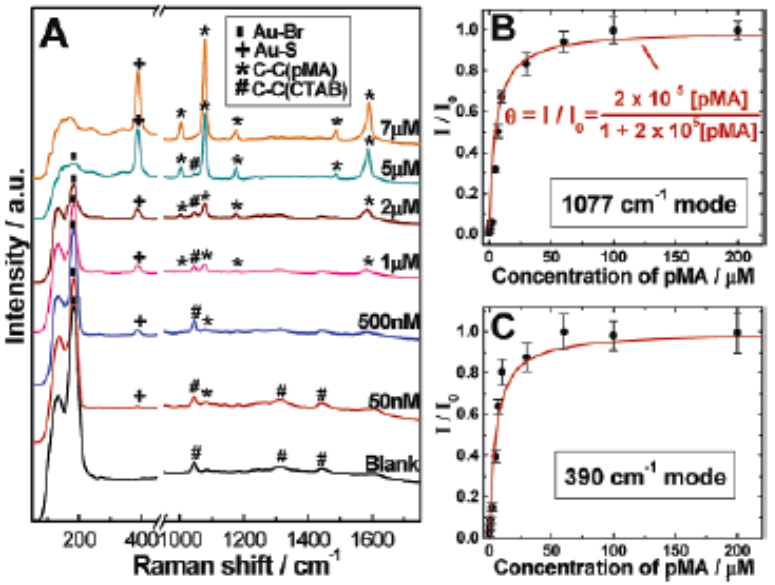

Figure 2. (A) SERS spectra of 5 μL of pMA with different concentrations deposited on the NP arrays. The excitation laser wavelength is 785 nm. Adsorption isotherm of pMA on the NP arrays obtained according to (B) 1077 and (C) 390 cm^{-1} modes in the SERS spectra. I_0 is the peak intensity of a saturated pMA monolayer.

Profiling the Near Field of a Plasmonic Nanoparticle with Raman-Based Molecular Rulers

NANO LETTERS

2006
Vol. 6, No. 10
2338−2343

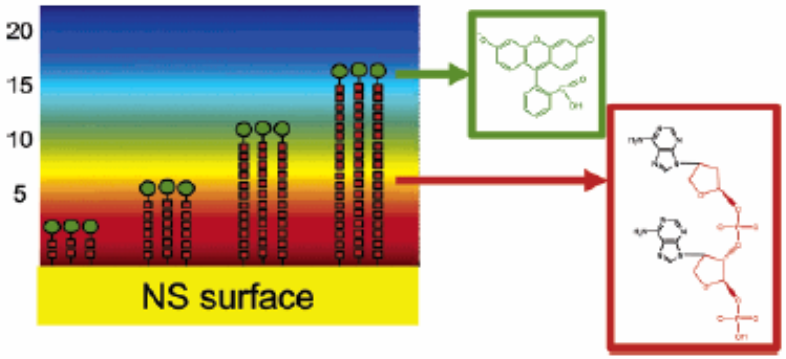

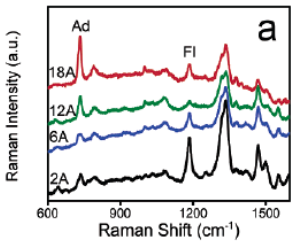

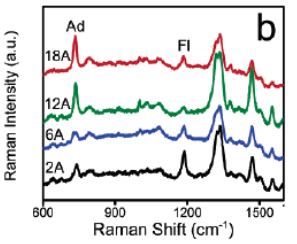

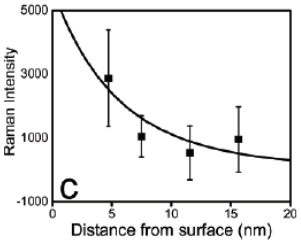

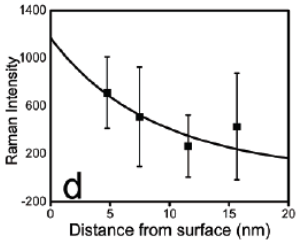

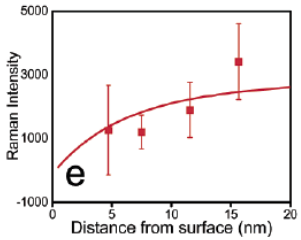

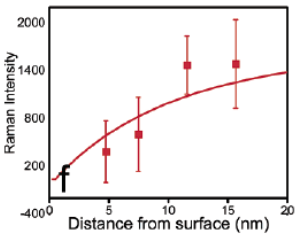

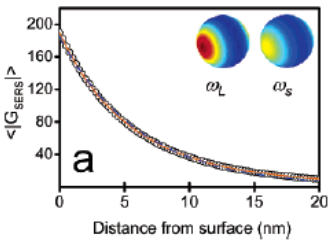

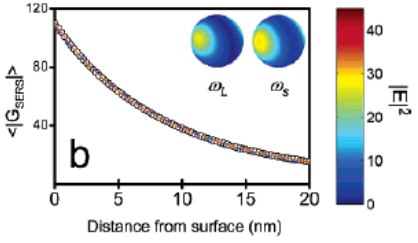

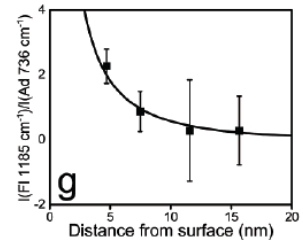

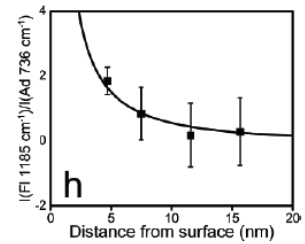

Anal. Chem. 2003, *75*, 6171−6176

Spectroscopic Tags Using Dye-Embedded Nanoparticles and Surface-Enhanced Raman Scattering

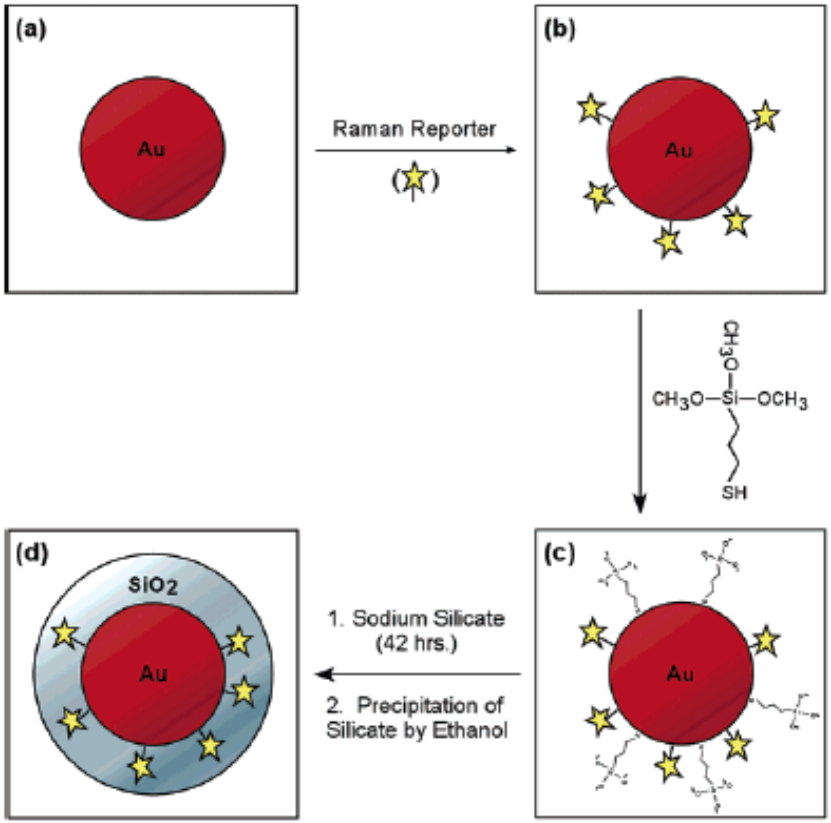

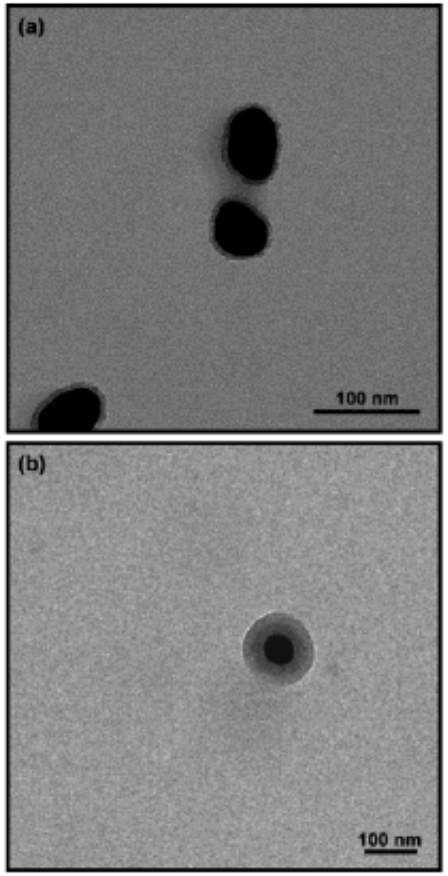

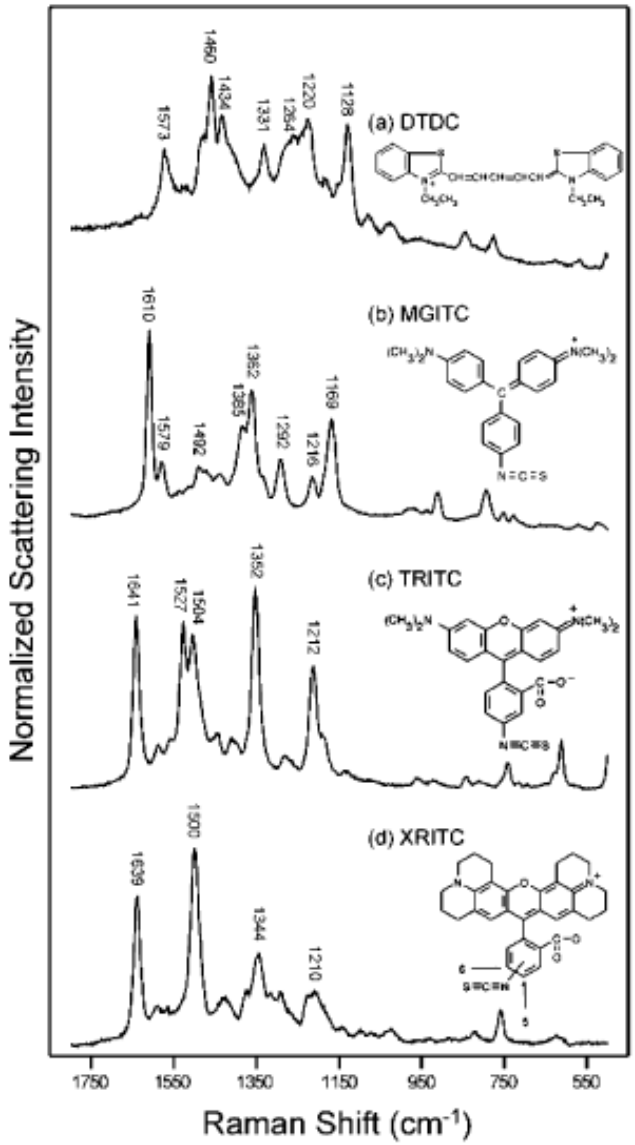

Figure 4. Chemical structures of four Raman reporters and their surface-enhanced resonance Raman spectra: (a) 3,3′-Diethylthiadicarbocyanine iodide (DTDC); (b) malachite green isothiocyanate (MGITC); (c) tetramethylrhodamine-5-isothiocyanate (TRITC); and (e) rhodamine-5-(and-6)-isothiocyanate (XRITC).

Anal. Chem. 2006, *78*, 6967−6973

Nanoparticle Probes with Surface Enhanced Raman Spectroscopic Tags for Cellular Cancer Targeting

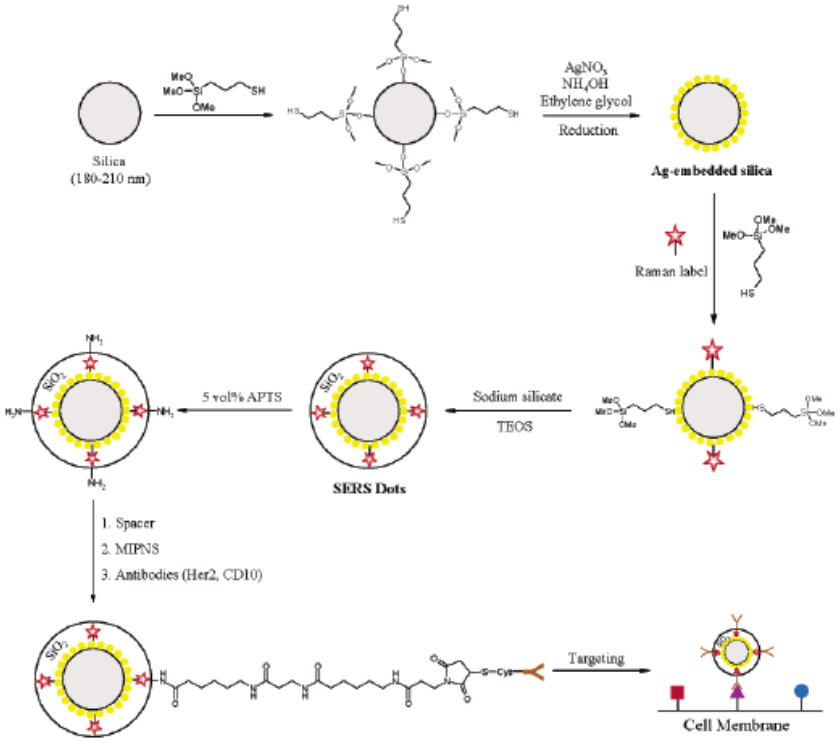

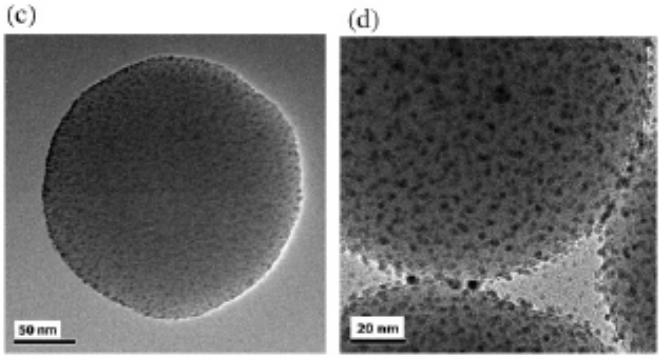

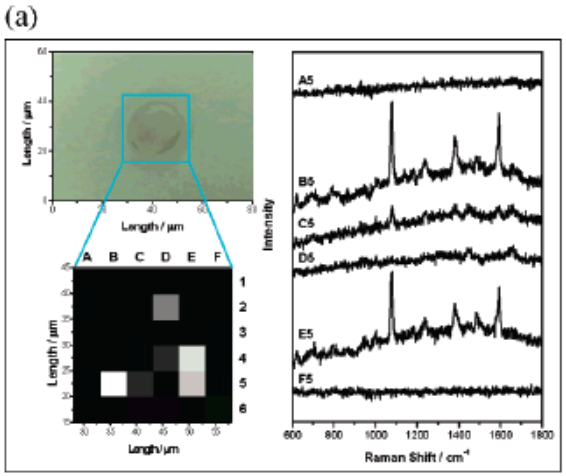

Anal. Chem. 2007, *79*, 916−922

Biological Imaging of HEK293 Cells Expressing PLCγ1 Using Surface-Enhanced Raman Microscopy

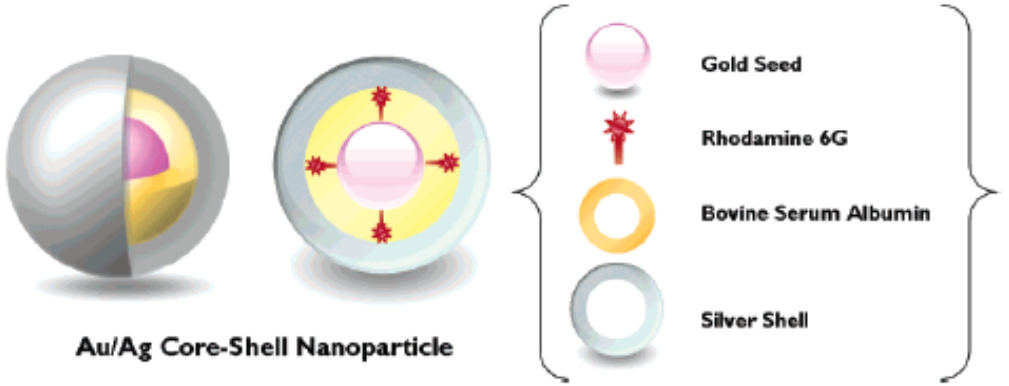

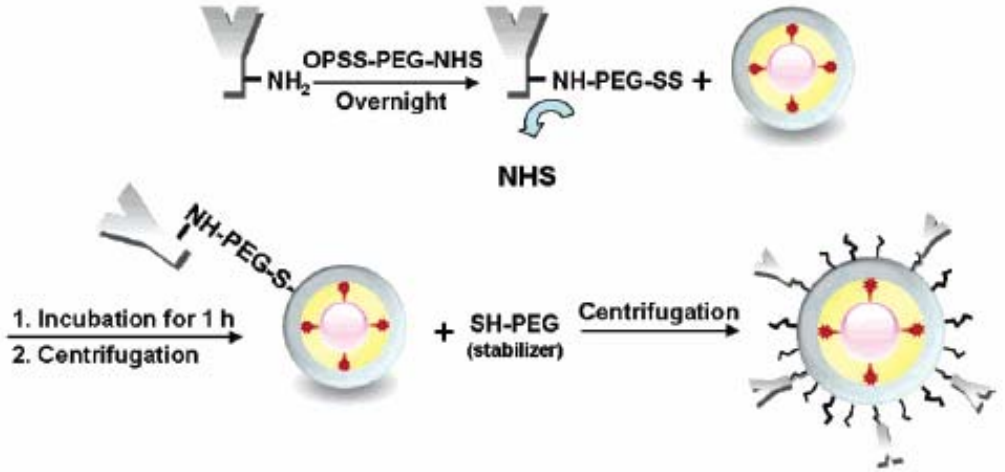

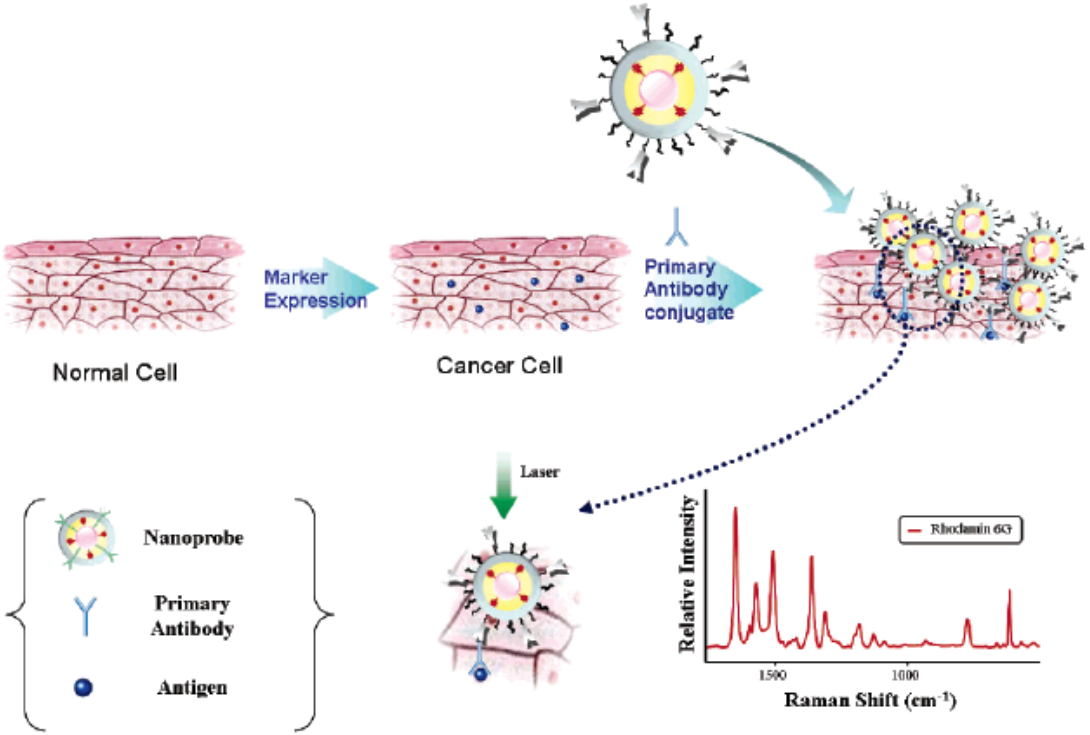

Figure 4. Schematic diagram depicting immobilization of Au/Ag core−shell nanoprobes on PLCγ1-expressing HEK293 cells and their SERS detection.

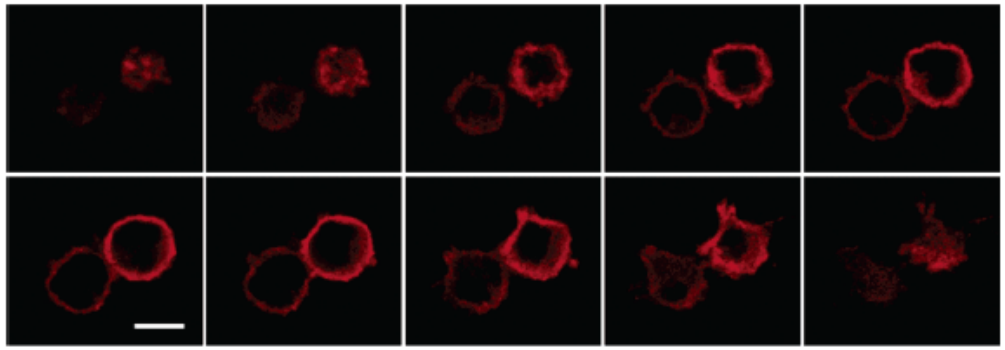

Figure 5. Serial fluorescence optical sections of PLCγ1-expressing HEK293 cells using red QDs. The *z*-axis interval of optical slices is 1.3 μm. Cells were incubated for 30 min in red QDs, after which the free QDs were washed away. These fluorescence images indicate that PLCγ1 markers are only expressed on the surface membranes. Scale bar, 10 μm.

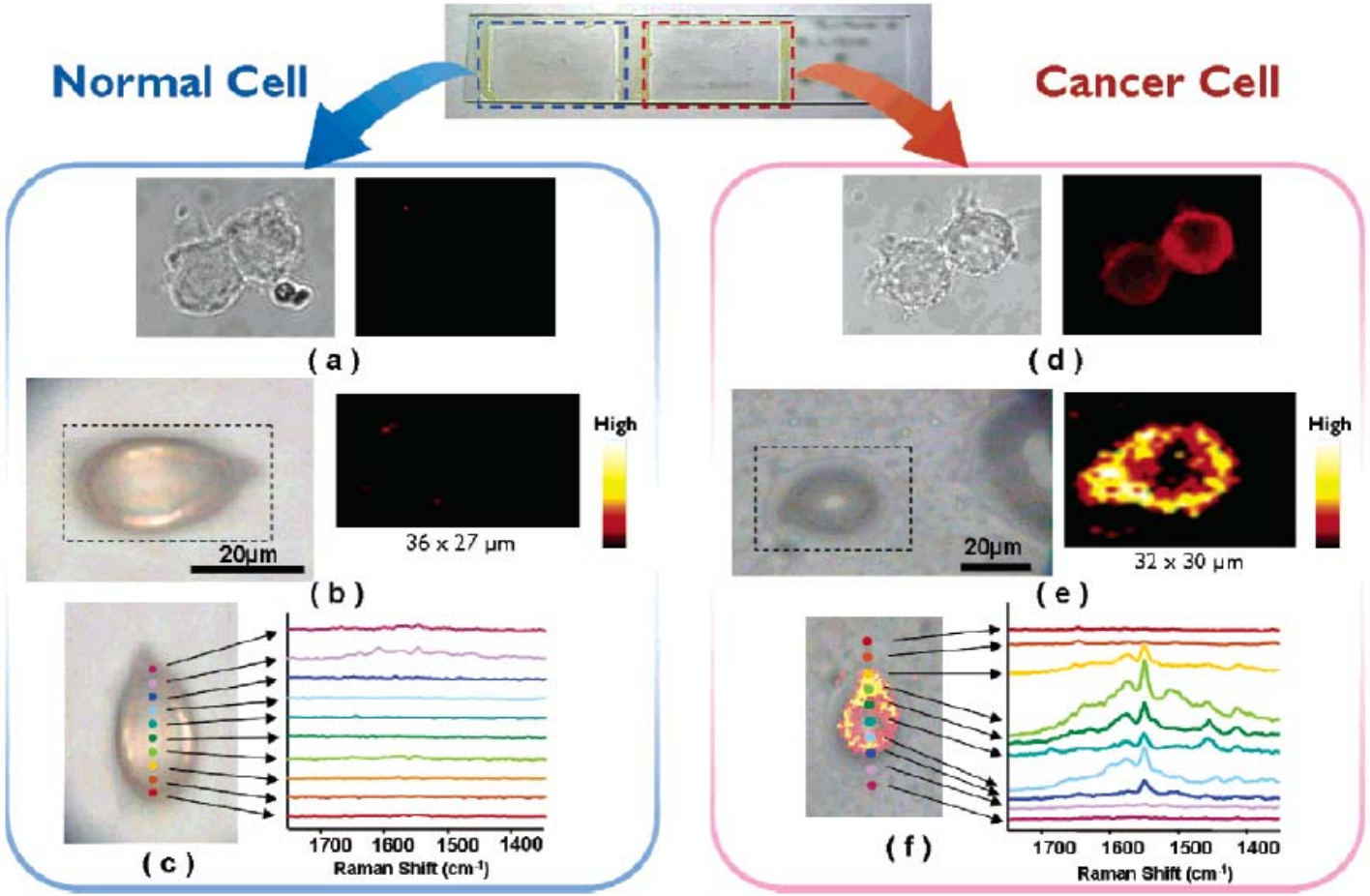

Figure 6. Fluorescence and SERS images of normal HEK293 cells and PLCγ1-expressing HEK293 cells. (a) QD-labeled fluorescence images of normal cells: (left) brightfield image, (right) fluorescence image. (b) SERS images of single normal cell: (left) brightfield image, (right) Raman mapping image of single normal cell based on the 1650-cm^{-1} R6G peak. The cell area was scanned with an interval of 1 μm. Intensities are scaled to the highest value in each area. (c) Overlay image of brightfield and Raman mapping for single normal cell. Colorful spots indicate the laser spots across the middle of the cell along the *y* axis. (d) QD-labeled fluorescence images of cancer cells: (left) brightfield image, (right) fluorescence image. (e) SERS images of single cancer cell: (left) brightfield image, (right) Raman mapping image of single cancer cell based on the 1650-cm^{-1} R6G peak. The cell area was scanned with an interval of 1 μm. Intensities are scaled to the highest value in each area. (f) Overlay image of brightfield and Raman mapping for single cancer cell. Colorful spots indicate the laser spots across the middle of the cell along the *y* axis.

J|A|C|S
COMMUNICATIONS

Published on Web 12/15/2006

Mammalian Cell Surface Imaging with Nitrile-Functionalized Nanoprobes: Biophysical Characterization of Aggregation and Polarization Anisotropy in SERS Imaging

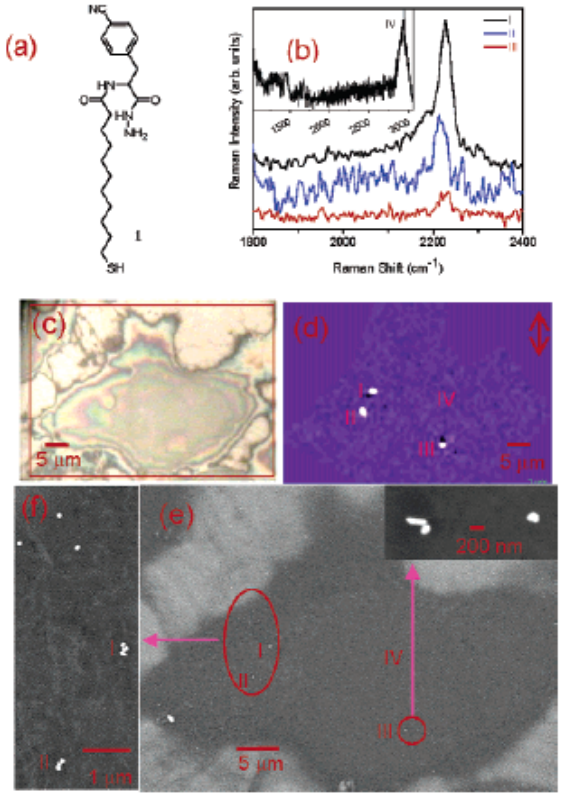

Figure 1. (a) The chemical structure of Raman reporter **1**; (b) Raman spectra of the CN vibration mode extracted from positions I, II, and III of the cell shown in the optical image (c). Inset of (b) is a cellular Raman spectrum taken from spot IV of the same cell. (d) Raman intensity map of the C═N band of the same cell, and (e) the corresponding SEM image. Inset in (e) showed the NPs in the lower right circle. (f) The group of NPs as shown in the large oval of (e).

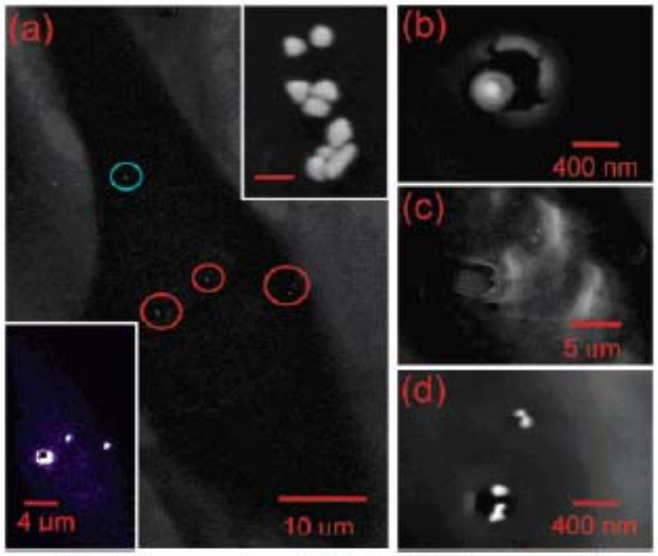

Figure 2. (a) SEM image of a cell. Upper right inset: magnification of a group of aggregated NPs. The scale bar is 200 nm. Lower left inset: the corresponding Raman intensity image of the same cell obtained with a power density of 10^5 W/cm^2. Laser-induced damage to the cell is shown in (b) the monomer (blue circle in a), (c) the aggregates, and (d) a pair of dimers.

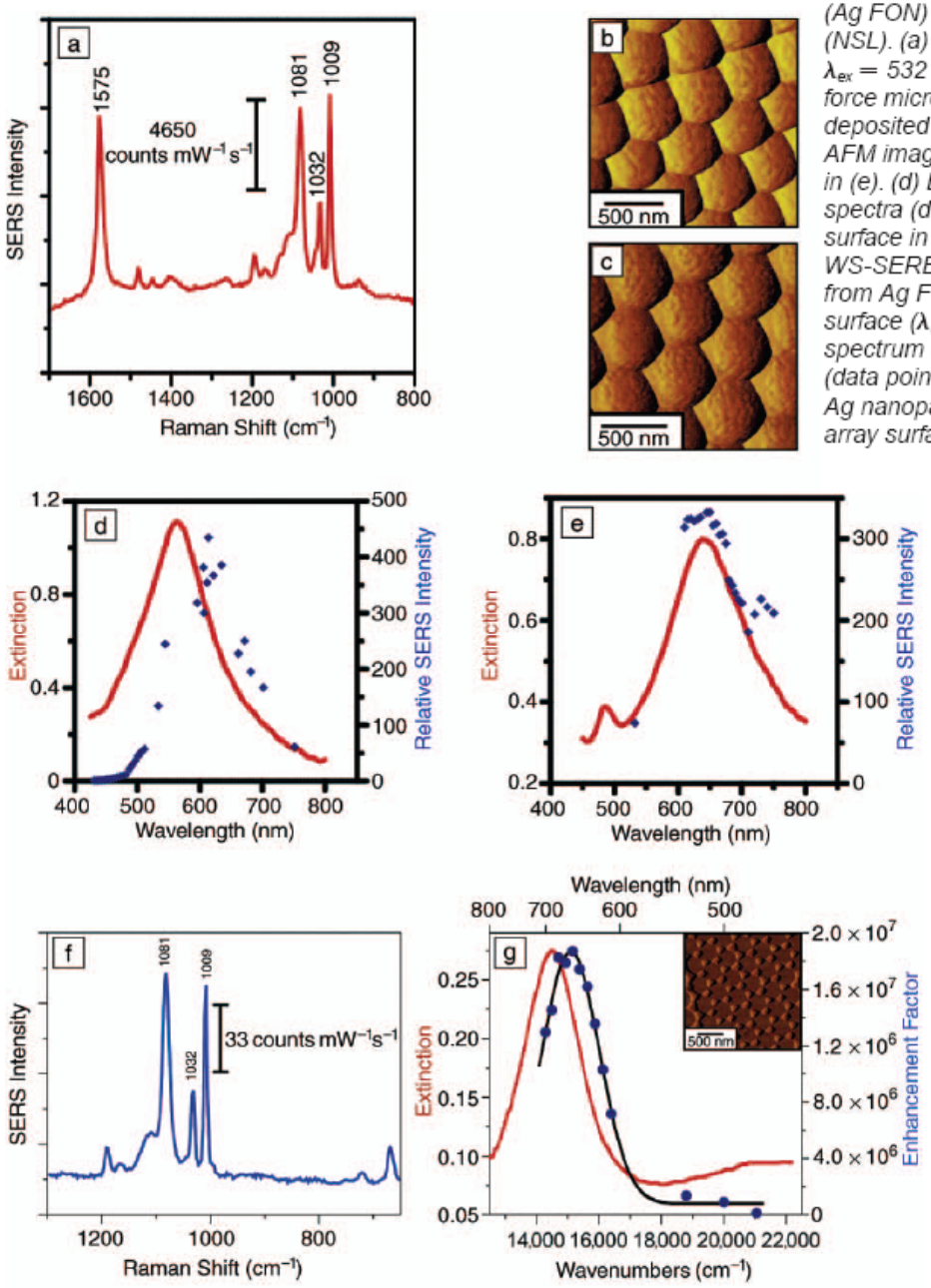

Figure 6. Localized surface plasmon resonance (LSPR), surface-enhanced Raman spectroscopy (SERS), and wavelength-scanned surface-enhanced Raman excitation spectroscopy (WS-SERES) results for benzenethiol adsorbed on Ag film-over-nanosphere (Ag FON) surfaces and nanoparticle arrays fabricated by nanosphere lithography (NSL). (a) SERS spectrum measured from Ag FON surface with excitation wavelength λ_{ex} = 532 nm, power = 3.0 mW, and 100 s data acquisition time. (b) Contact-mode atomic force microscopy (AFM) image of Ag FON surface (nanosphere diameter D = 410 nm, deposited mass thickness d_m = 200 nm) used for SERS in (a). (c) Contact-mode AFM image of Ag FON surface (D = 500 nm, d_m = 250 nm) used for WS-SERES in (e). (d) LSPR spectrum (solid line, λ_{max} = 562 nm, FWHM = 144 nm) and WS-SERES spectra (data points) for the 1081 cm^{-1} band of benzenethiol measured from the Ag FON surface in (b). (e) LSPR spectrum (solid line, λ_{max} = 638 nm, FWHM = 131 nm) and WS-SERES spectra (data points) for the 1081 cm^{-1} band of benzenethiol measured from Ag FON surface in (c). (f) SERS spectrum measured from Ag nanoparticle array surface (λ_{ex} = 532 nm, power = 3.0 mW, 100 s data acquisition time). (g) LSPR spectrum (solid line, λ_{max} = 688 nm, FWHM = 95 nm) and WS-SERES spectra (data points) for the 1081 cm^{-1} band of benzenethiol measured from a Ag nanoparticle array surface. (inset) Tapping-mode AFM image of a representative array surface.

Tip Enhanced Raman

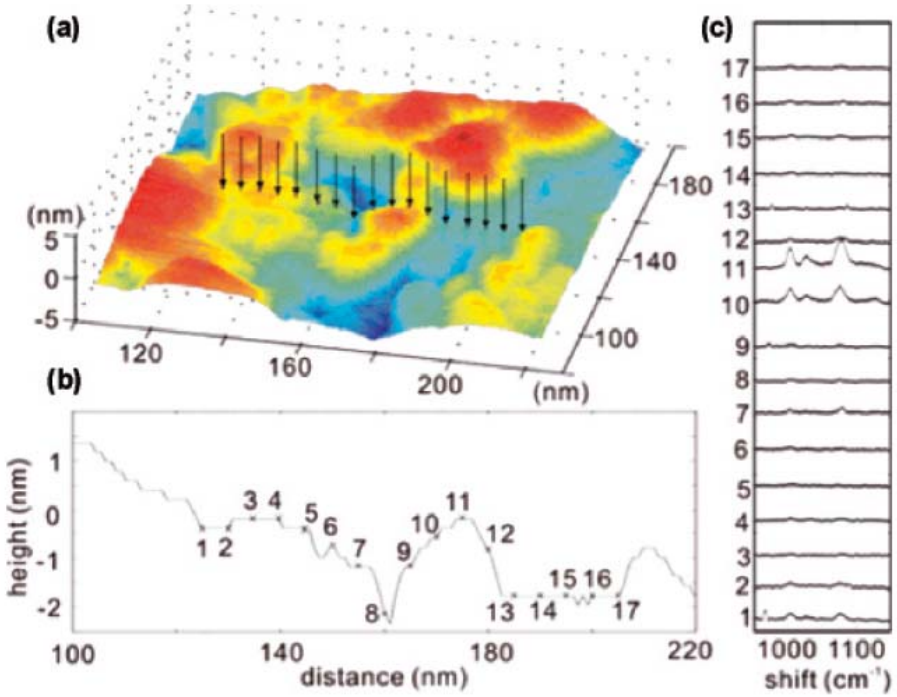

Figure 24. TERS mapping on a rough Au surface. An STM image of the sample is shown in a. TERS data was collected at the positions indicated by the arrows. The cross section of the topography image is shown in b, and the TERS collection sites are labeled with crosses. (c) Corresponding TERS sequence. The numbers denote the sites where the spectra were collected. Reprinted with permission from ref 463. Copyright 2007 American Chemical Society.

Near-Field Raman Microscopy

Droplet of AG nano particles labelled with Rodamine 6G on cover glass

Experiment Parameters:

Excitation Laser:	532 nm
Scan Range:	4 µm x 4 µm
Resolution:	100 x 100 pixel
Integration Time:	110 ms per spectrum
Feedback:	SNOM AC Mode

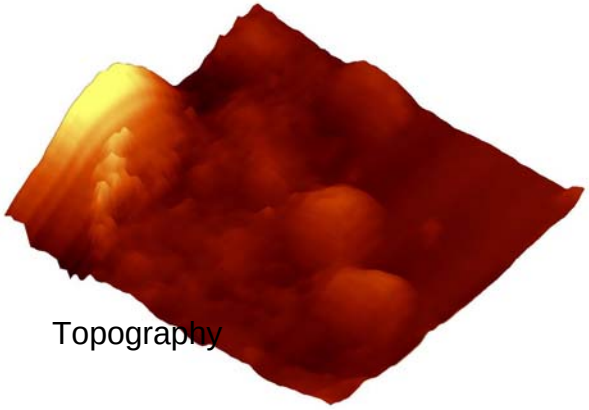

Topography

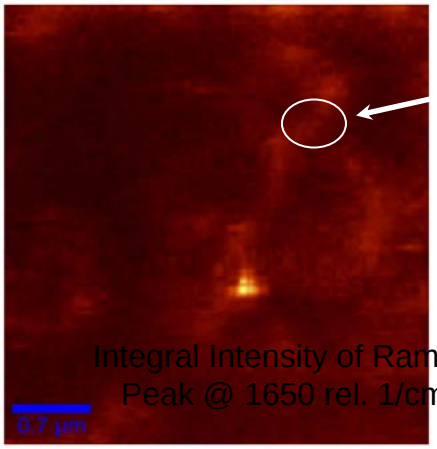

Integral Intensity of Raman Peak @ 1650 rel. 1/cm

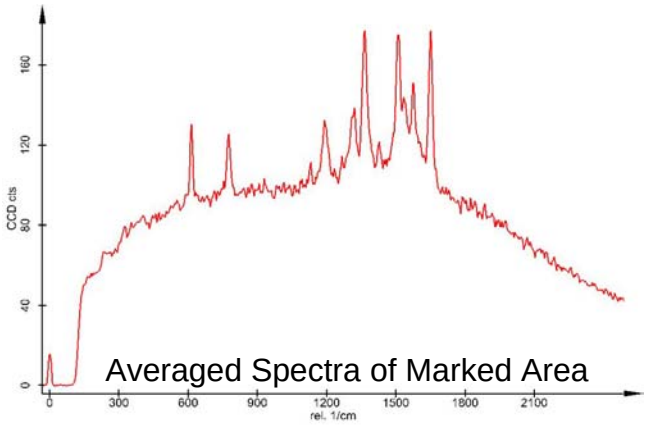

Averaged Spectra of Marked Area

Periodic Hole Array

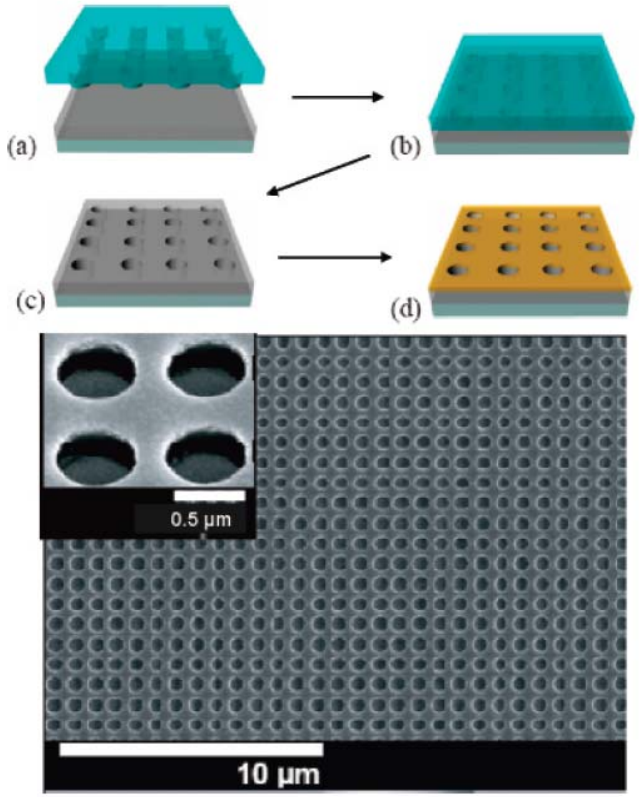

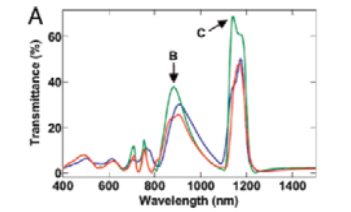

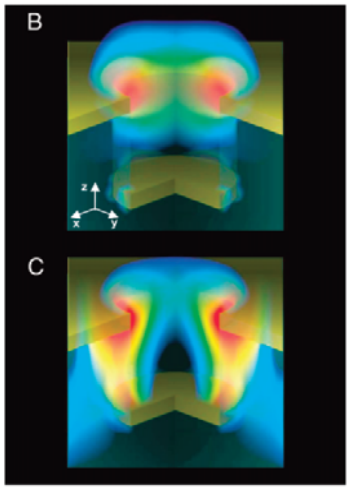

Figure 17. Correlation of transmission spectral features with hole/disk plasmonic excitations. (a) Normal incidence transmission spectrum of a quasi-3D plasmonic crystal (blue), and rigorous electrodynamics modeling of the spectrum for an ideal crystal (green) and one that includes subtle isolated nanoscale grains of Au near the edges of the Au disks (red). (b) Computed electromagnetic field distribution associated with the resonance at 883 nm (labeled B in a). The intensity is concentrated at the edges of the nanoholes in the upper level of the crystal. (c) Field distribution associated with the resonance at 1138 nm (labeled C in a), showing strong coupling between the upper and lower levels of the crystal. Reprinted with permission from ref 77. Copyright 2006 The National Academy of Sciences of the USA.

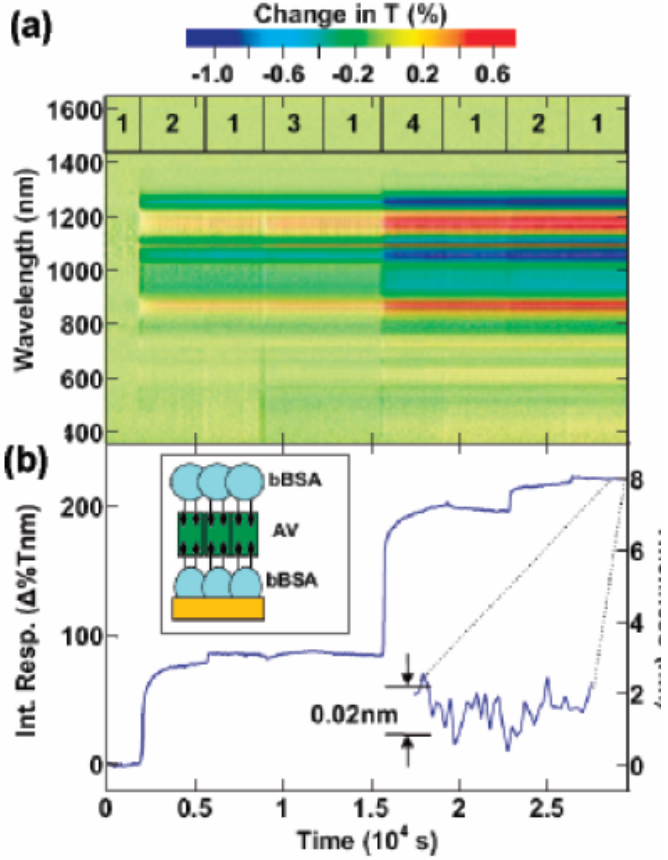
(a)
Change in T (%)
-1.0 -0.6 -0.2 0.2 0.6
1 2 1 3 1 4 1 2 1
Wavelength (nm)
(b)
bBSA
AV
bBSA
0.02nm
Int. Resp. (Δ%Tnm)
Time (10⁴ s)

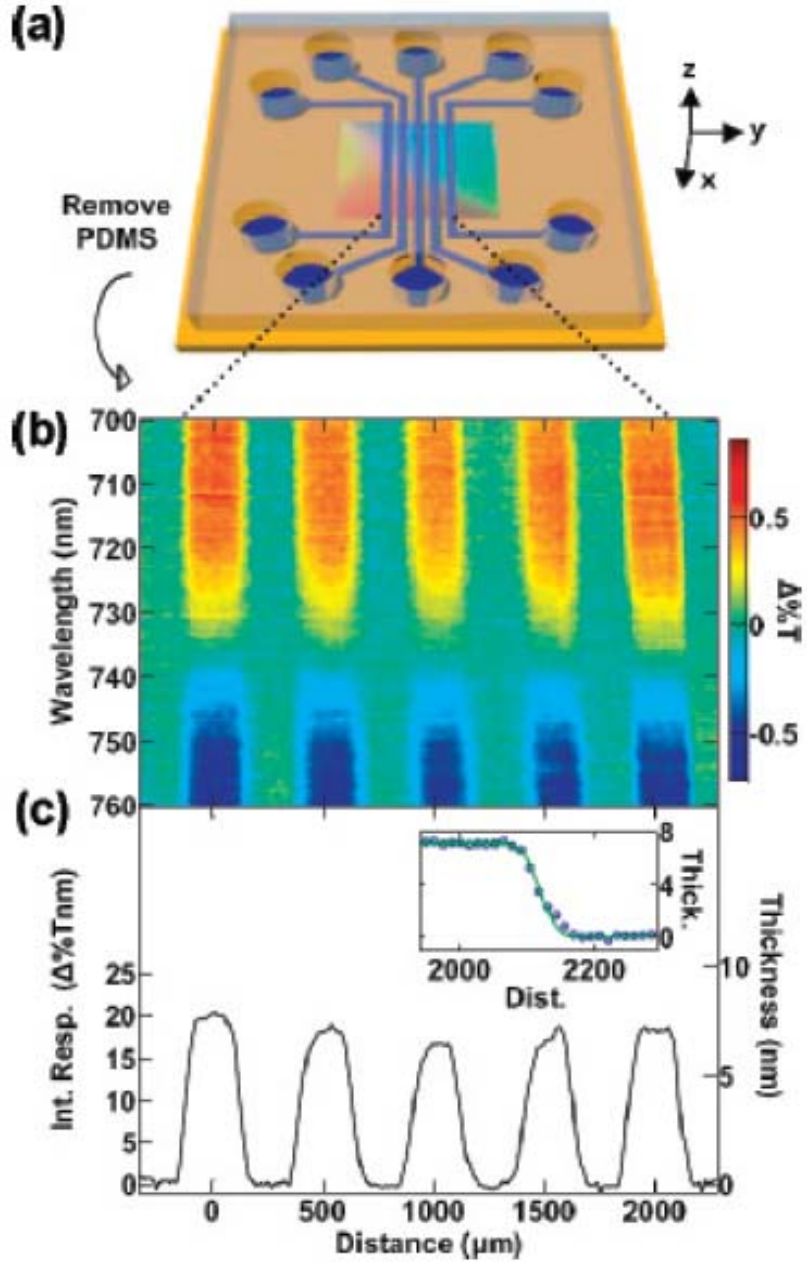
(a)
Remove PDMS
z
y
x
(b)
Wavelength (nm)
Δ%T
(c)
Int. Resp. (Δ%Tnm)
Thick.
Dist.
Thickness (nm)
Distance (μm)

Nanomaterials for Biodiagnostic

- Nucleic Acid
  - Genetic information for identification
  - Diseases, bacterium, virus, pathogen
  - PCR with molecular fluorophore, State of the Art
  - Expansive, Non-portable, Non-multiplexing
- Proteins
  - Cancers and diseases, unusual high concentration of marker
  - ELISA (~pM) with molecular fluorophore
  - No PCR version

ELISA (Enzyme-Linked Immunosorbent Assay)

is a biochemical technique used mainly in immunology to detect the presence of an antibody or an antigen in a sample. It utilizes two antibodies, one of which is specific to the antigen and the other of which is coupled to an enzyme. This second antibody gives the assay its "enzyme-linked" name, and will cause a chromogenic or fluorogenic substrate to produce a signal.

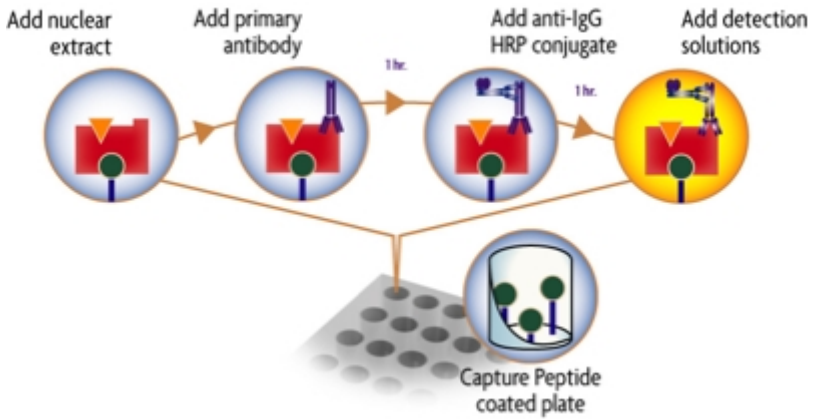

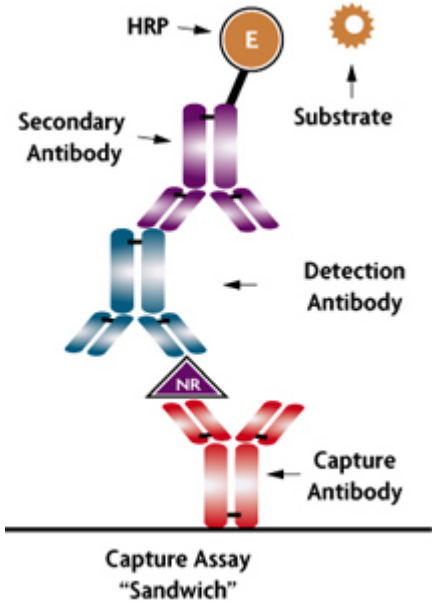

Why Nanomaterials?

- Molecular fluorophores
  - Limited spectral response
  - photostability
- Nanomaterials
  - Small size (1-100 nm)
  - Chemically tailorable physical properties
  - Unusual target binding properties
  - Structure robustness

Tailorable Physical Properties

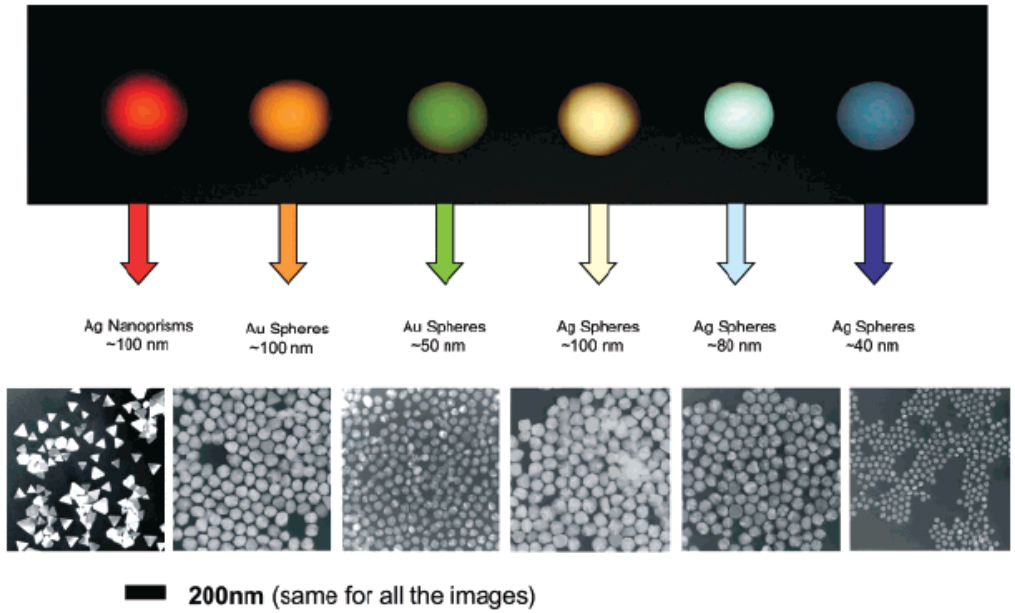

Figure 1. Sizes, shapes, and compositions of metal nanoparticles can be systematically varied to produce materials with distinct light-scattering properties.

Nanomaterial Detection

- Optical
- Electrical and electrochemical
- Magnetic
- Nanowire and Nanotubes
- Nanofabrication

Colorimetric Detection of DNA

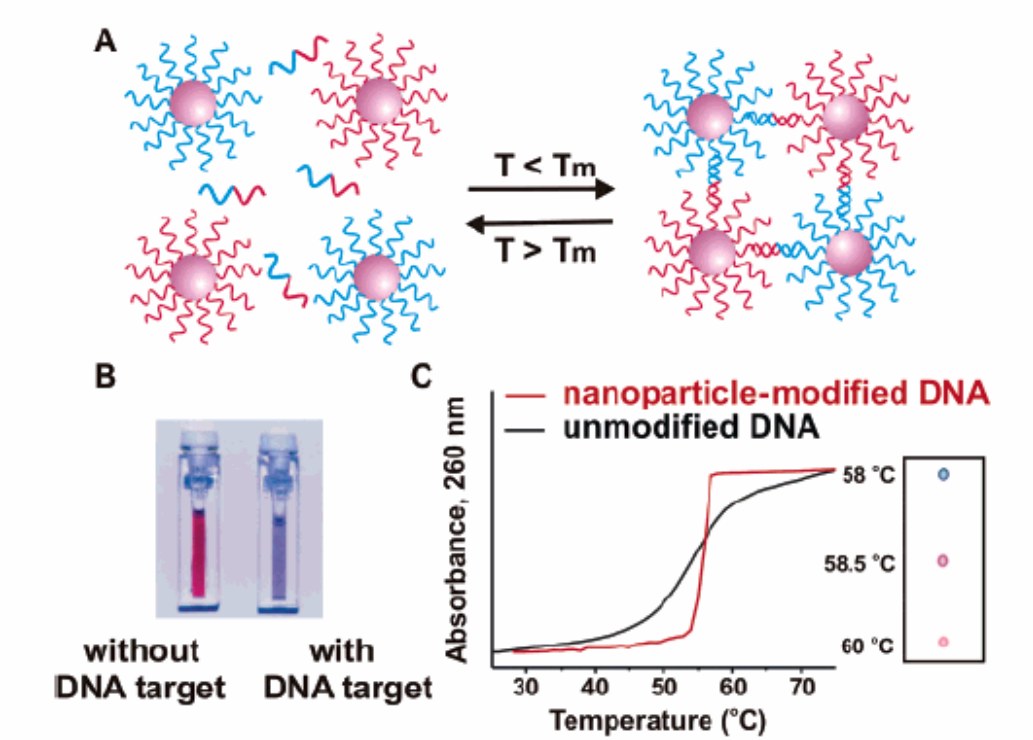

Figure 2. In the presence of complementary target DNA, oligonucleotide-functionalized gold nanoparticles will aggregate (A), resulting in a change of solution color from red to blue (B). The aggregation process can be monitored using UV−vis spectroscopy or simply by spotting the solution on a silica support (C). (Reprinted with permission from *Science* (http://www.aaas.org), ref 29. Copyright 1997 American Association for the Advancement of Science.)

A DNA-based method for rationally assembling nanoparticles into macroscopic materials

Chad A. Mirkin, Robert L. Letsinger, Robert C. Mucic & James J. Storhoff

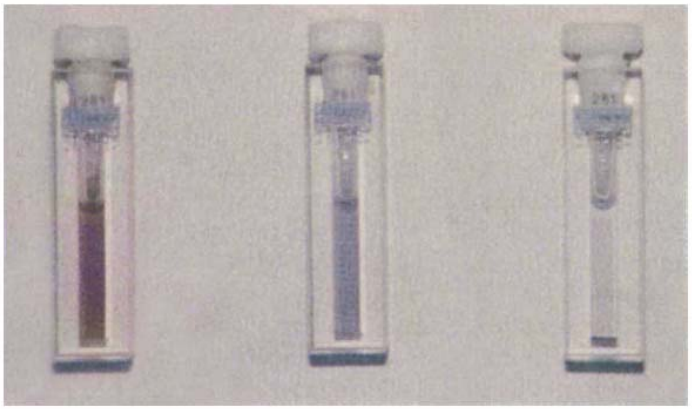

FIG. 2 Cuvettes with the Au colloids and the four DNA strands responsible for the assembly process. Left cuvette, at 80 °C with DNA-modified colloids in the unhybridized state; centre, after cooling to room temperature but before the precipitate settles; and right, after the polymeric precipitate settles to the bottom of the cuvette. Heating either of these cool solutions results in the reformation of the DNA-modified colloids in the unhybridized state (shown in the left cuvette).

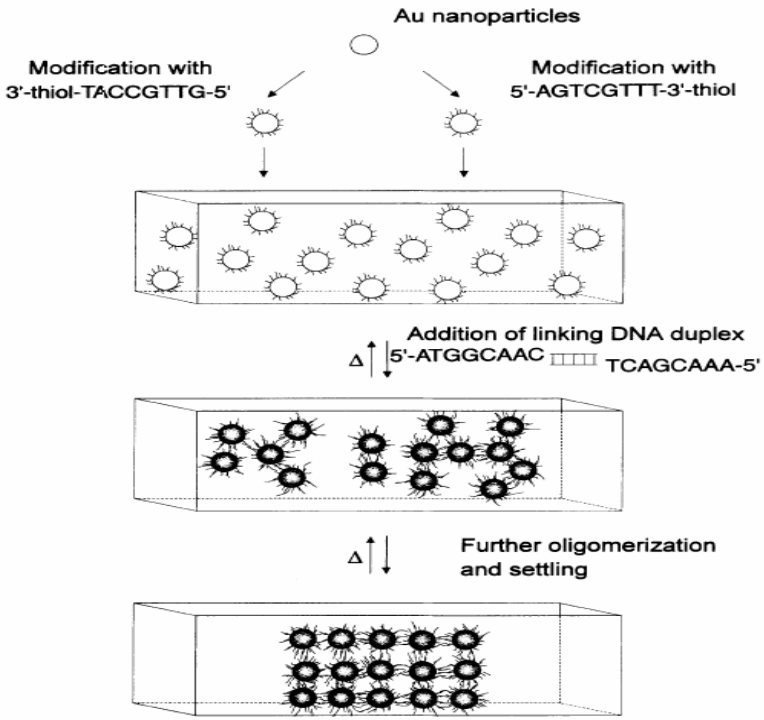

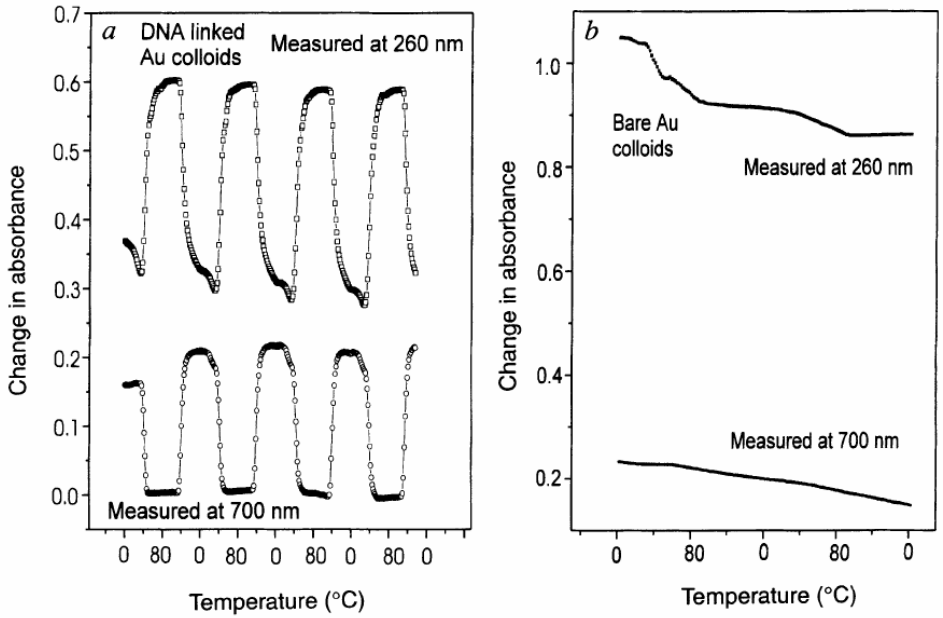

Nature, 1996, 382, 607

Selective Colorimetric Detection of Polynucleotides Based on the Distance-Dependent Optical Properties of Gold Nanoparticles

Robert Elghanian, James J. Storhoff, Robert C. Mucic,
Robert L. Letsinger,* Chad A. Mirkin*

SCIENCE • VOL. 277 • 22 AUGUST 1997

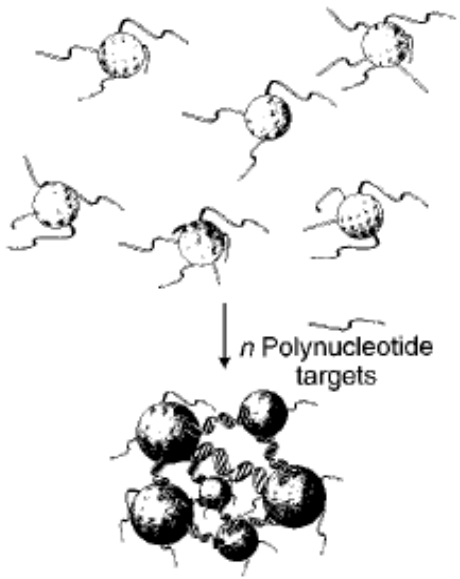

Fig. 1. Schematic representation of the concept for generating aggregates signaling hybridization of nanoparticle-oligonucleotide conjugates with oligonucleotide target molecules. The nanoparticles and the oligonucleotide interconnects are not drawn to scale, and the number of oligomers per particle is believed to be much larger than depicted.

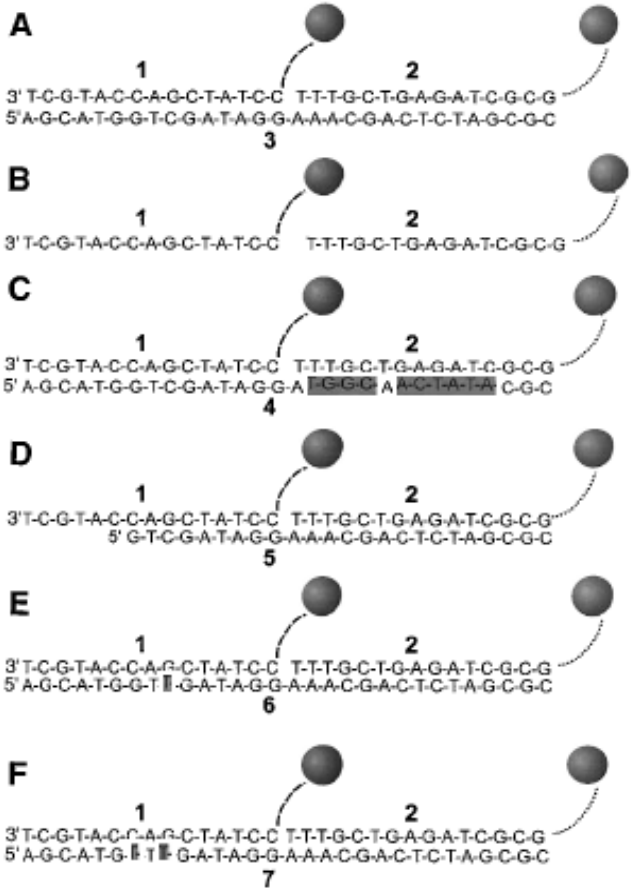

Fig. 2. Mercaptoalkyloligonucleotide-modified 13-nm Au particles and polynucleotide targets used for examining the selectivity of the nanoparticle-based colorimetric polynucleotide detection system. (**A**) Complementary target; (**B**) probes without the target; (**C**) a half-complementary target; (**D**) a 6-bp deletion; (**E**) a 1-bp mismatch; and (**F**) a 2-bp mismatch. For the sake of clarity, only two particles are shown; in reality a polymeric aggregate with many particles is formed. Dashed lines represent flexible spacer portions of the mercaptoalkyloligonucleotide strands bound to the nanoparticles; note that these spacers, because of their noncomplementary nature, do not participate in hybridization. The full sequences for the two probes, **1** and **2**, which bind to targets **3** through **7**, are

1-5′SH-$(CH_2)_6$- [CTA-ATC-CGC-ACA-G]
spacer

[CC-TAT-CGA-CCA-TGC-T]
probe

2-5′SH-$(CH_2)_6$-[ATG-GCA-ACT-ATA-C]
spacer

[GC-GCT-AGA-GTC-GTT-T]
probe

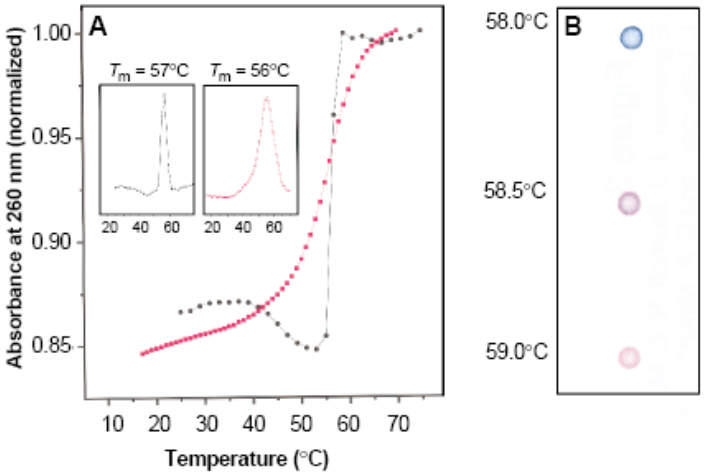

Fig. 3. (**A**) Comparison of the thermal dissociation curves for complexes of mercaptoalkyloligonucleotide-modified Au nanoparticles (black circles) and mercaptoalkyloligonucleotides without Au nanoparticles (red squares) with the complementary target, **3**, in hybridization buffer (0.1 M NaCl, 10 mM phosphate buffer, pH 7.0). For the first set (black circles), a mixture of 150 μl of each colloid conjugate and 3 μl of the target oligonucleotide in hybridization buffer (0.1 M NaCl, 10 mM phosphate, pH 7.0) was frozen at the temperature of dry ice, kept for 5 min, thawed over a period of 15 min, and diluted to 1.0 ml with buffer (final target concentration, 0.02 μM). The absorbance was measured at 1-min intervals with a temperature increase of 1°C per minute. The increase in absorption at 260 nm (A_{260}) was ~0.3 absorption units (AU). In the absence of the oligonucleotide targets, the absorbance of the nanoparticles did not increase with increasing temperature. For the second set, the mercaptoalkyloligonucleotides and complementary target (each 0.33 μM) were equilibrated at room temperature in 1 ml of buffer, and the changes in absorbance with temperature were monitored as before. The increase in A_{260} was 0.08 AU. (**Insets**) Derivative curves for each set (*15*). (**B**) Spot test showing T_c (thermal transition associated with the color change) for the Au nanoparticle probes hybridized with complementary target. A solution prepared from 150 μl of each probe and 3 μl of the target (0.06 μM final target concentration) was frozen for 5 min, allowed to thaw for 10 min, transferred to a 1-ml cuvette, and warmed at 58°C for 5 min in the thermally regulated cuvette chamber of the spectrophotometer. Samples (3 μl) were transferred to a C_{18} reverse phase plate with an Eppendorf pipette as the temperature of the solution was increased incrementally 0.5°C at 5-min intervals.

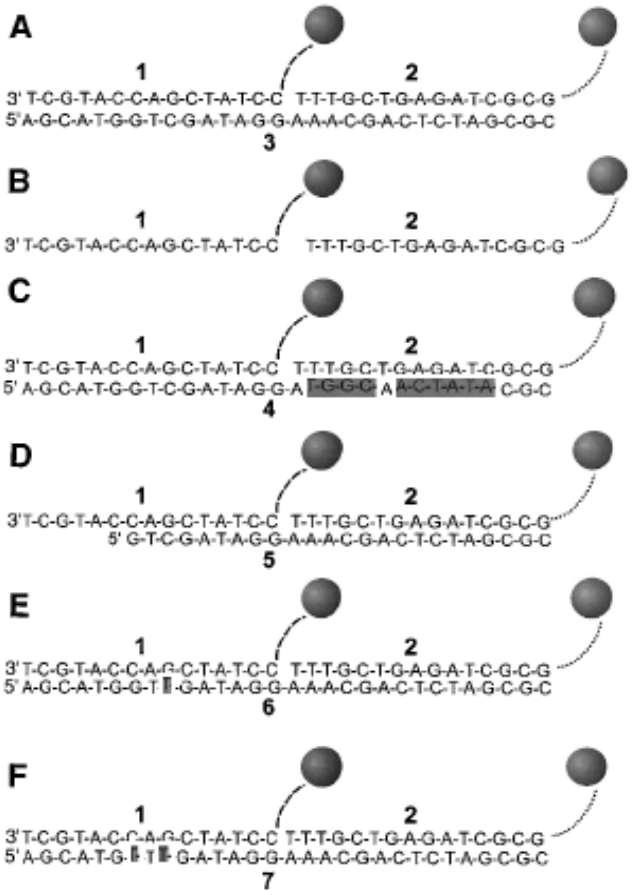

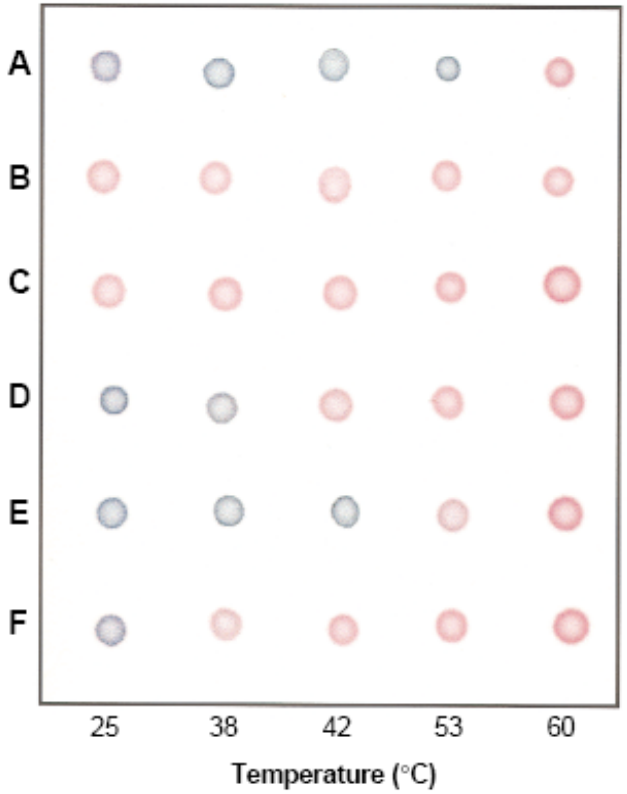

Fig. 4. Selective polynucleotide detection for the target probes shown in Fig. 2: (**A**) complementary target; (**B**) no target; (**C**) complementary to one probe; (**D**) a 6-bp deletion; (**E**) a 1-bp mismatch; and (**F**) a 2-bp mismatch. Nanoparticle aggregates were prepared in a 600-μl thin-walled Eppendorf tube by addition of 1 μl of a 6.6 μM oligonucleotide target to a mixture containing 50 μl of each probe (0.06 μM final target concentration). The mixture was frozen (5 min) in a bath of dry ice and isopropyl alcohol and allowed to warm to room temperature. Samples were then transferred to a temperature-controlled water bath, and 3-μl aliquots were removed at the indicated temperatures and spotted on a C_{18} reverse phase plate.

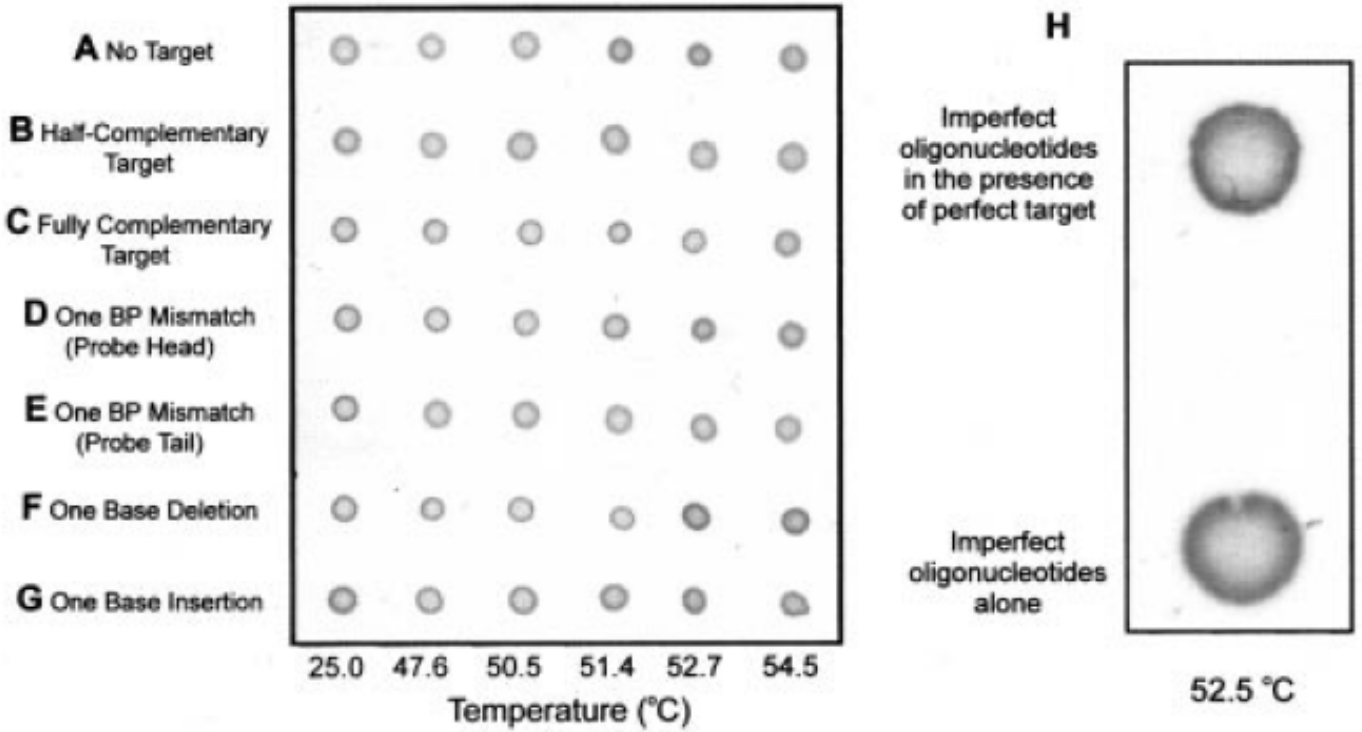

Figure 5. (A−G) The spot method for polynucleotide detection which demonstrates the selectivity of the Au nanoparticle based detection system toward single base imperfections. The probes and corresponding polynucleotide targets are listed in Figure 2. (H) Spot test demonstrating the detection and differentiation by color of a polynucleotide target in the presence of polynucleotides with single base imperfections.

1nM => 50pM

Rapid Aggregation of Gold Nanoparticles Induced by Non-Cross-Linking DNA Hybridization

Kae Sato, Kazuo Hosokawa, and Mizuo Maeda*

8102 ■ J. AM. CHEM. SOC. 2003, *125*, 8102−8103

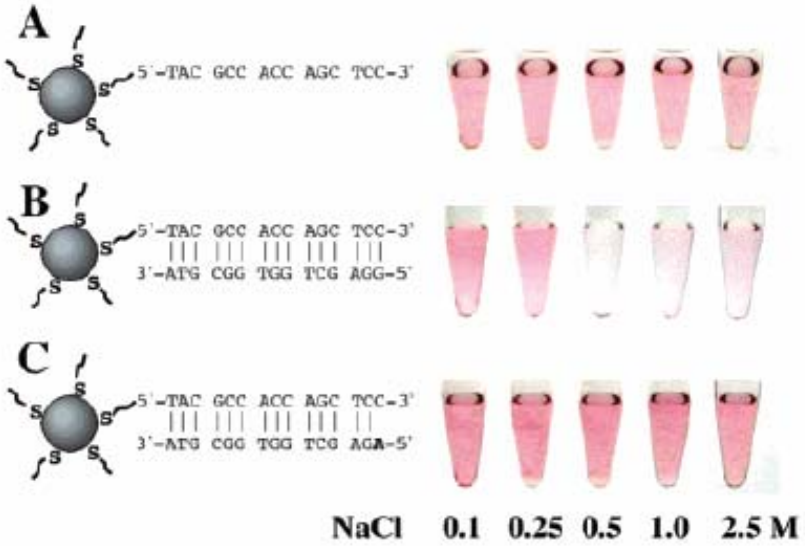

Figure 1. Aggregation behaviors of the DNA-gold nanoparticles at various NaCl concentrations at room temperature: (A) without a target DNA, (B) with the complementary target, and (C) with a target containing a single-base mismatch at its 5′ terminus. The final concentrations of the particle, the probe DNA, and the targets were 2.3, 500, and 500 nM, respectively.

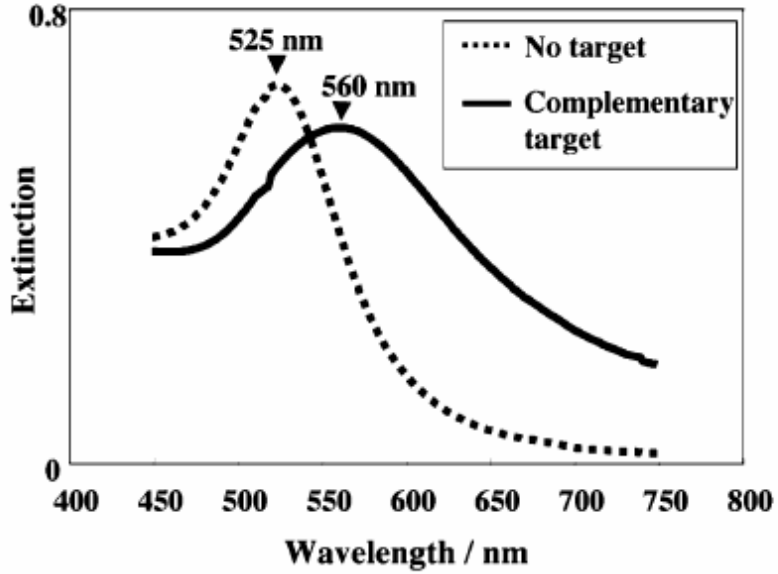

Figure 2. Visible spectra corresponding to Figure 1A (dotted line, no target) and 1B (solid line, complementary target) at 0.5 M NaCl.

60-500 nM

J. Am. Chem. Soc. **2000,** *122,* 9071−9077

Colloidal Au-Enhanced Surface Plasmon Resonance for Ultrasensitive Detection of DNA Hybridization

Lin He, Michael D. Musick, Sheila R. Nicewarner, Frank G. Salinas, Stephen J. Benkovic, Michael J. Natan, and Christine D. Keating*

Scheme 1. SPR Surface Assembly

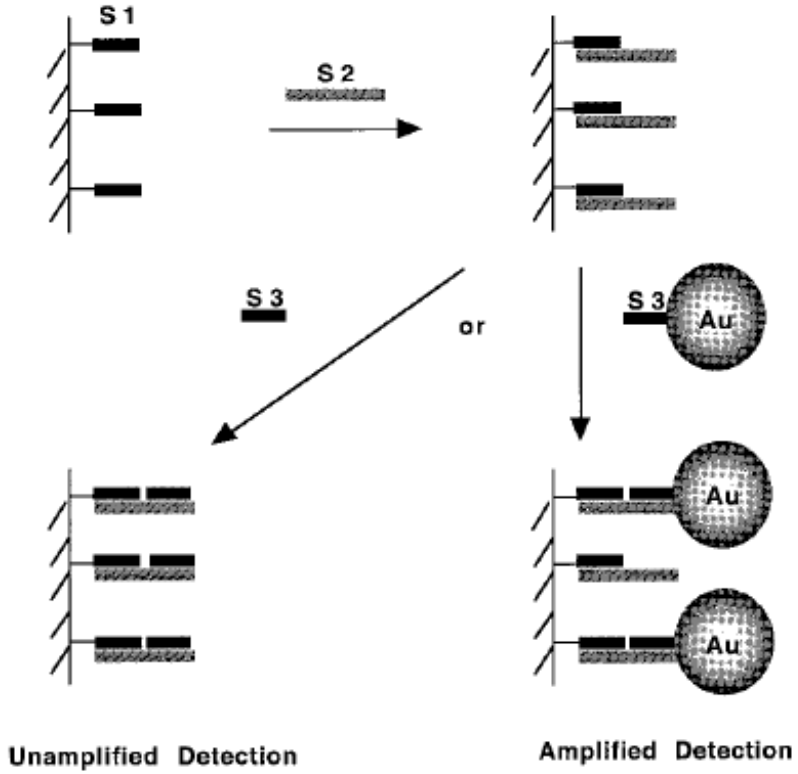

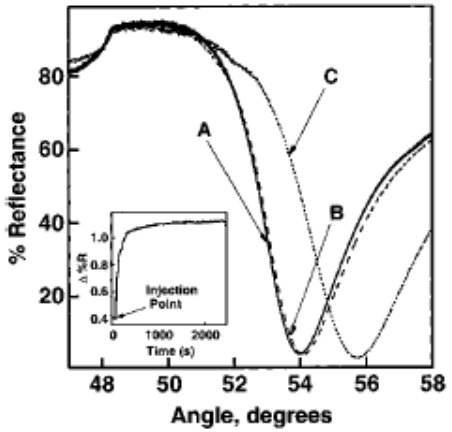

Figure 1. SPR curves of surfaces prepared in sequential steps as illustrated in Scheme 1: a MHA-coated Au film modified with a 12-mer oligonucleotide S1(A), after hybridization with its complementary 24-mer target S2 (B), and followed by introduction of S3:Au conjugate (C) to the surface. Inset: surface plasmon reflectance changes at 53.2° for the oligonucleotide-coated Au film measured during a 60-min exposure to S3:Au conjugates.

Scheme 2. SPR Surface Assembly in the Digestion Experiment

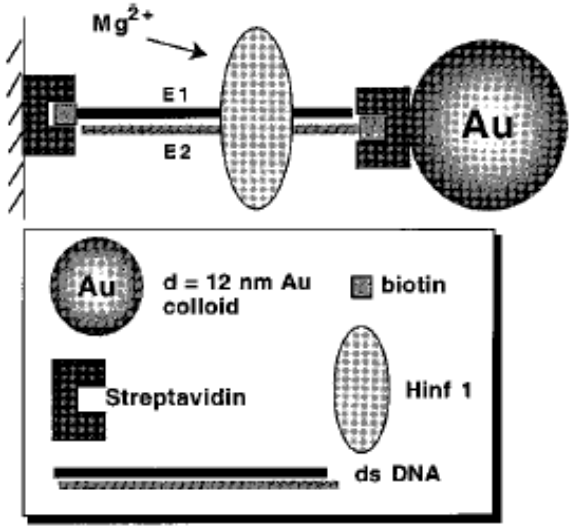

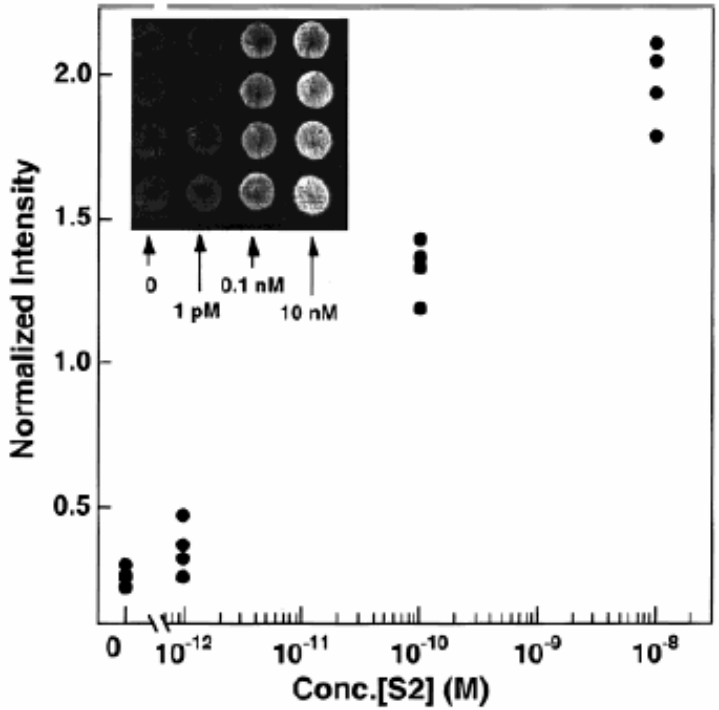

Figure 5. Plot of normalized intensity of SPR reflectance as a function of logarithmic concentration of the analyte 24-mer oligo (S2). Each spot represents one data point at the corresponding concentration. CCD parameters: exposure time = 0.3 s, 16 bit resolution, spot size = 4.5 mm in diameter. Inset: a 2-D SPR image of a Au surface derivatized with 20 μL of buffer blank, 1 pM, 0.1 nM, and 10 nM S2 oligos (from left to right, respectively).

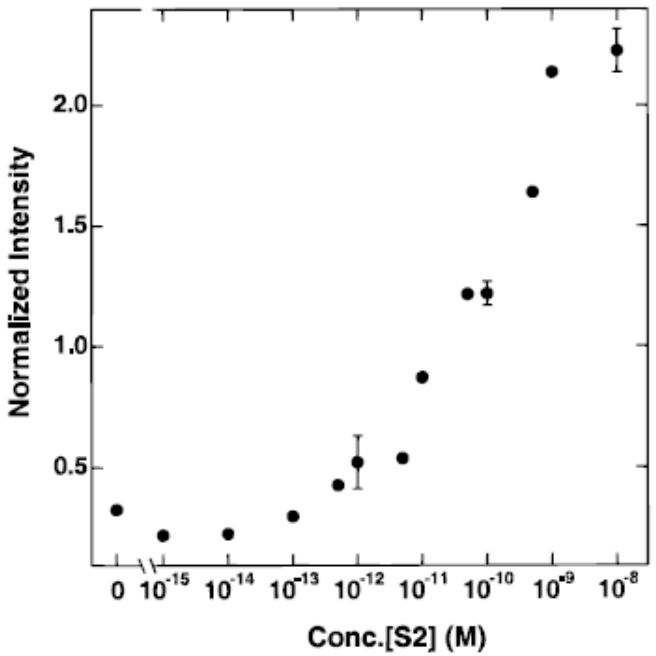

Figure 7. Plot of normalized intensity of SPR reflectance as a function of logarithmic concentration of the analyte 24-mer oligo (S2) from the image shown in Figure 6. The error bars are standard deviations from the data in Figure 5.

Table 1. Comparison of Sensitivity for Au−Amplified SPR in DNA Analysis with Other Techniques

detection method	detection limit of target DNA	refs
radiolabeling	100 fg	71
fluorescence	1.2×10^7 probes/cm^2	36
unamplified scanning SPR	100 fg/100 μm^2 for 10-mer oligos, 150 nM ~120 bp DNA	33, 35
unamplified imaging SPR	10 nM 16-mer oligos	63
Au-amplified scanning SPR	lower than 10 pM 24-mer oligos[a]	this work
Au-amplified imaging SPR	10 pM 24-mer oligos, ≤12 pg/cm^2 (≤8×10^8 oligonucleotides/cm^2)[b]	this work

[a] The spots on SPR imaging surface can be detected by scanning SPR with ease, which demonstrated a lower detection limit can be achieved with the scanning instrument. Considering an instrumental angle resolution limit of 0.005°, a theoretical detection limit of 2×10^7 particles/cm^2 can be realized.[21] [b] The oligonucleotide surface coverage reported for these experiments is an upper limit, determined by assuming 100% of the molecules in solution hybridized to the surface.

A Gold Nanoparticle Based Approach for Screening Triplex DNA Binders

Min Su Han, Abigail K. R. Lytton-Jean, and Chad A. Mirkin*

4954 ■ J. AM. CHEM. SOC. 2006, *128*, 4954−4955

Scheme 1. Representation of Structure and Color Change of Nanoassembly in the Presence of Triplex Binder at Room Temperature

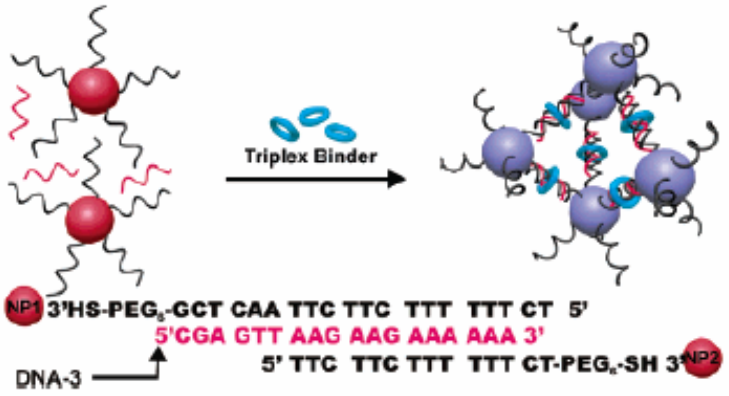

Figure 3. The color change of nanoassembly (NP-1, NP-2, and DNA-3) in the absence and presence of DNA binders at room temperature.

Sequence specific

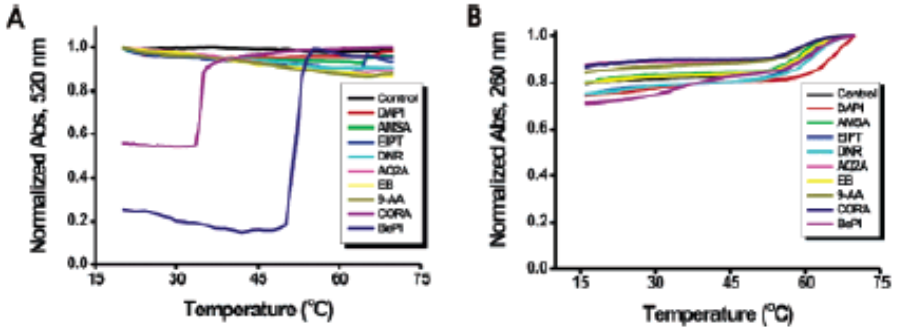

Figure 2. Melting curves of (A) NP-1, NP-2, and DNA-3 assemblies in the presence of DNA binders, (B) DNA-1, DNA-2, and DNA-3 (no nanoparticles) in the presence of DNA binders.

Self-Assembled Nanoparticle Probes for Recognition and Detection of Biomolecules

Dustin J. Maxwell, Jason R. Taylor, and Shuming Nie*,†

9606 ■ J. AM. CHEM. SOC. 2002, *124*, 9606−9612

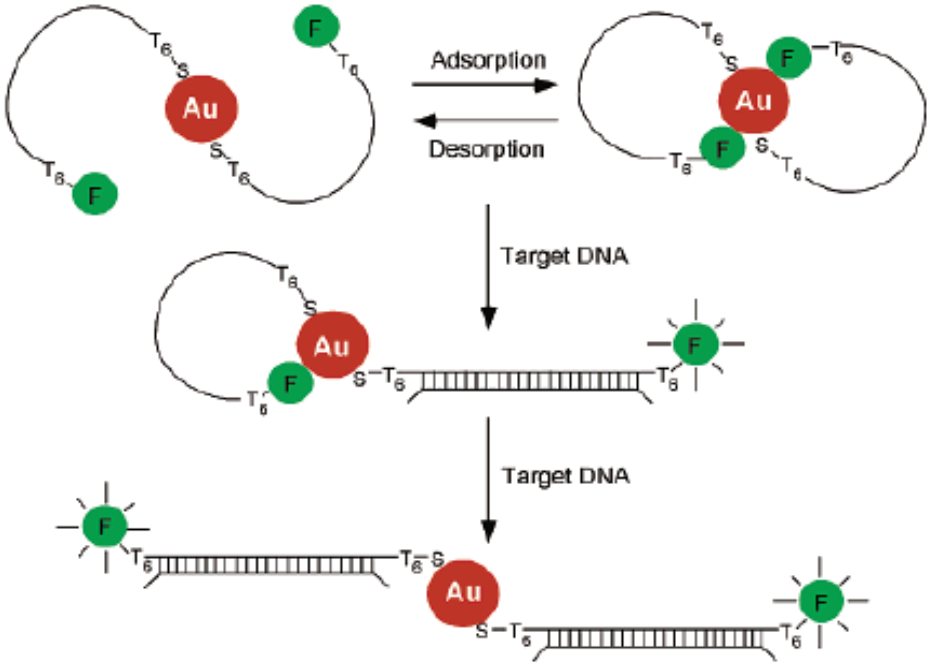

Figure 1. Nanoparticle-based probes and their operating principles. Two oligonucleotide molecules (oligos) are shown to self-assemble into a constrained conformation on each gold particle (2.5 nm diameter). A T_6 spacer (six thymines) is inserted at both the 3′- and 5′-ends to reduce steric hindrance. Single-stranded DNA is represented by a single line and double-stranded DNA by a cross-linked double line. In the assembled (closed) state, the fluorophore is quenched by the nanoparticle. Upon target binding, the constrained conformation opens, the fluorophore leaves the surface because of the structural rigidity of the hybridized DNA (double-stranded), and fluorescence is restored. In the open state, the fluorophore is separated from the particle surface by about 10 nm. See text for detailed explanation. Au, gold particle; F, fluorophore; S, sulfur atom.

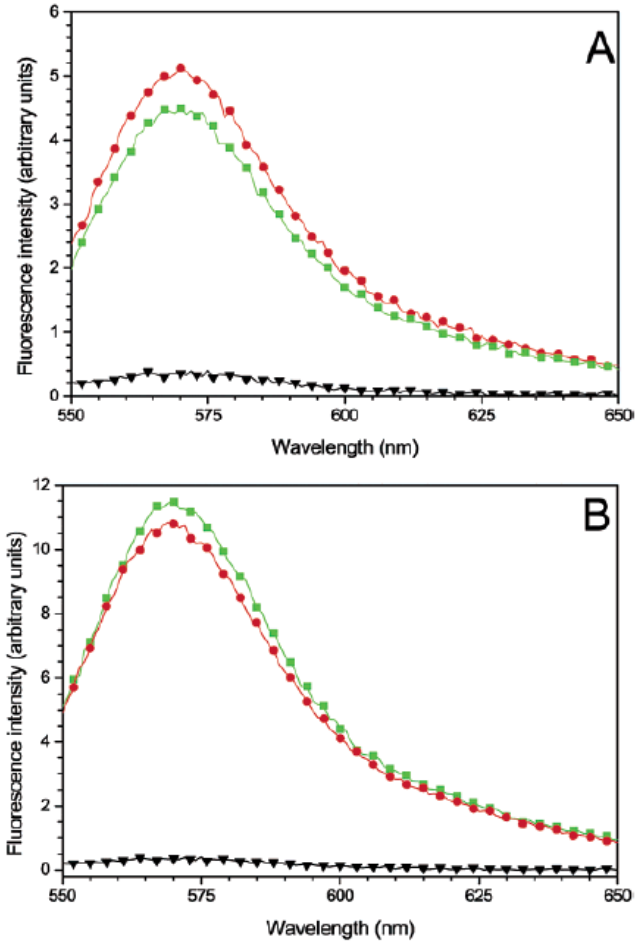

Figure 5. Fluorescence responses and the lack of sequence recognition abilities observed for nonthiolated nanoparticle probes. (A) Fluorescence spectra of nonthiolated probes generated by a complementary target (red curve), a noncomplementary target (green curve), and no target (black curve). These probes are considered nonfunctional because they do not recognize specific DNA sequences. (B) Fluorescence signals obtained from the supernatant solution when the probes were treated with a complementary target (red curve) or a noncomplementary target (green curve). The result revealed that the oligos were released into solution by nonspecific adsorption of the target on the particle surface. With a thiol group, this release was not observed (little or no signal in solution, black curve in B). The nonfunctional probes were prepared in the same way as the functional probes, except that the 3′-end thiol group was deleted. The intensity differences for the red and green curves were within experimental errors and had no particular significance.

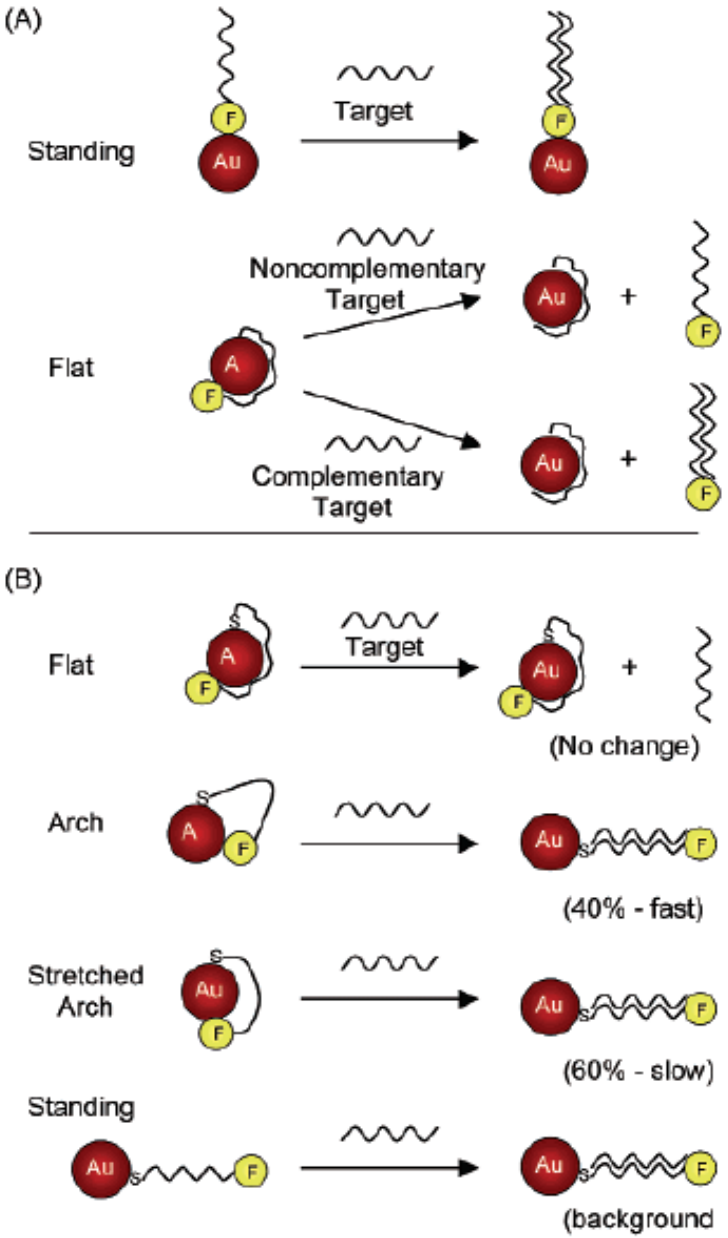

Figure 6. Schematic illustration of possible configurations for (a) nonthiolated and (b) thiolated oligonucleotides adsorbed on colloidal gold nanocrystals. Detailed discussion in text.

Silver Amplification

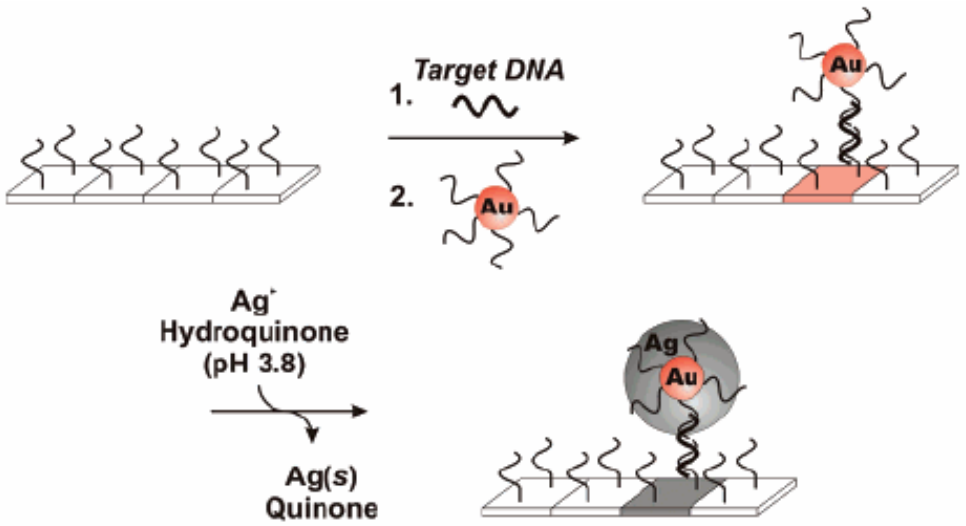

Figure 4. Scanometric DNA assay. In this assay a surface-bound capture oligonucleotide binds one-half of the target of interest, and an oligonucleotide-functionalized gold nanoparticle probe binds to the other half. Catalytic reduction of silver onto the capture/target/probe sandwich results in a signal that can be detected scanometrically. (Reprinted with permission from *Science* (http://www.aaas.org), ref 66. Copyright 2000 American Association for the Advancement of Science.)

Catalytic reduction of Ag on Au

Scanometric DNA Array Detection with Nanoparticle Probes

SCIENCE VOL 289 8 SEPTEMBER 2000

T. Andrew Taton,[1,2] Chad A. Mirkin,[1,2]* Robert L. Letsinger[1]*

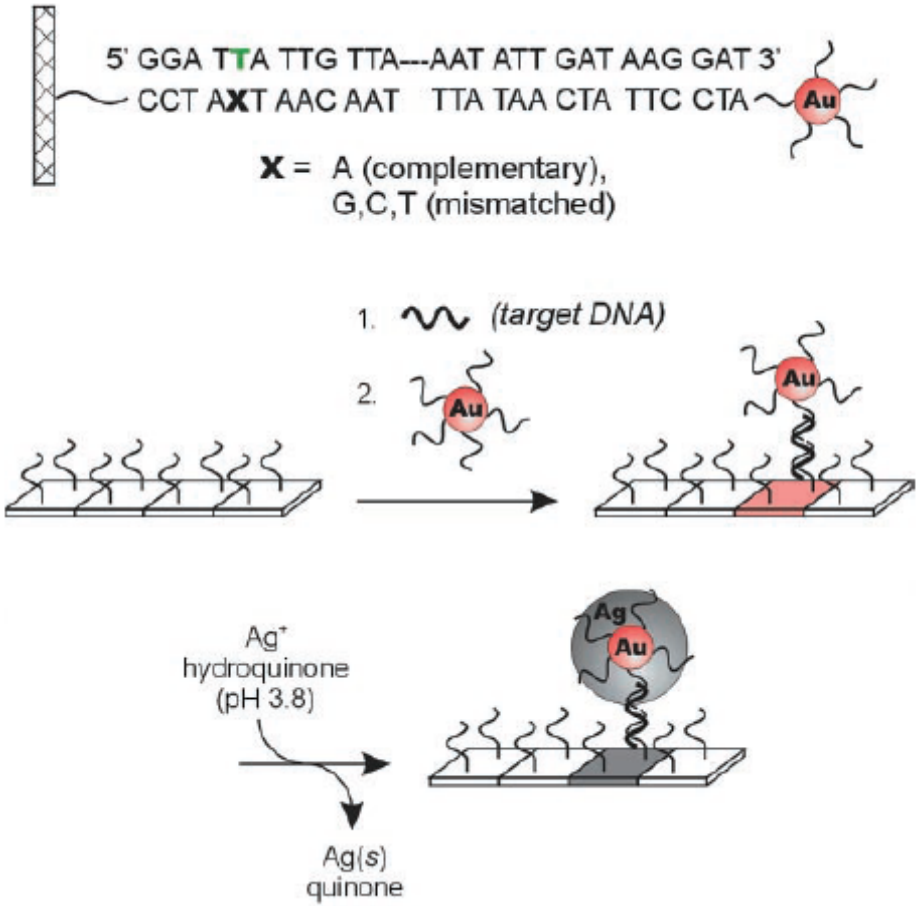

50 fM => 0.2 fM

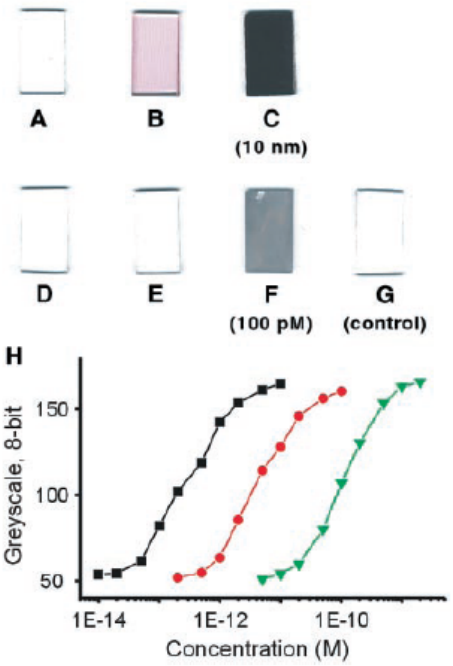

Fig. 1. Images of 7 mm by 13 mm, oligonucleotide-functionalized, float glass slides, obtained with a flatbed scanner. (**A**) Slide before hybridization of target and nanoparticle probe. (**B**) A slide identical to (A) after hybridization with oligonucleotide target (10 nM) and then nanoparticle probes (5 nM in particles). The pink color derives from the Au nanoparticle probes. (**C**) A slide identical to (B) after exposure to silver amplification solution for 5 min. (**D**) Slide before hybridization of target and nanoparticle probe. (**E**) A slide identical to (D) after hybridization with target (100 pM) and then nanoparticle probe (5 nM). The extinction of the submonolayer of nanoparticles is too low to be observed visually or with a flatbed scanner. (**F**) A slide identical to (E) after exposure to silver amplification solution for 5 min. Slide (F) is lighter than slide (C), indicating a lower concentration of target. (**G**) A control slide exposed to 5 nM nanoparticle probe and then exposed to silver amplification solution for 5 min. No darkening of the slide is observed. (**H**) Graph of 8-bit gray scale values as a function of target concentration. The gray scale values were taken from flatbed scanner images of oligonucleotide-functionalized glass surfaces that had been exposed to varying concentrations of oligonucleotide target, labeled with 5 nM oligonucleotide probe and immersed in silver amplification solution. For any given amplification time, the grayscale range is limited by surface saturation at high grayscale values and the sensitivity of the scanner at low values. Therefore, the dynamic range of this system can be adjusted by means of hybridization and amplification conditions (that is, lower target concentrations require longer amplification periods). Squares: 18-base capture-target overlap (*5*), 8× PBS hybridization buffer [1.2 M NaCl and 10 mM NaH_2PO_4/Na_2HPO_4 buffer (pH 7)], 15 min amplification time. Circles: 12-base capture-target overlap, 8× PBS hybridization buffer, 10 min amplification time. Triangles: 12-base capture-target overlap, 2× PBS hybridization buffer [0.3 M NaCl, 10 mM NaH_2PO_4/Na_2HPO_4 buffer (pH 7)], 5 min amplification time. The lowest target concentration that can be effectively distinguished from the background baseline is 50 fM.

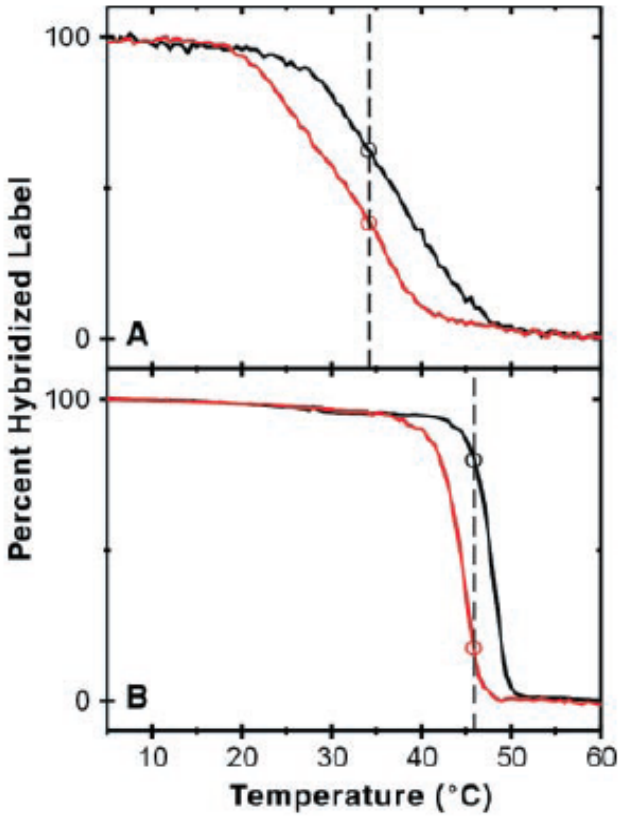

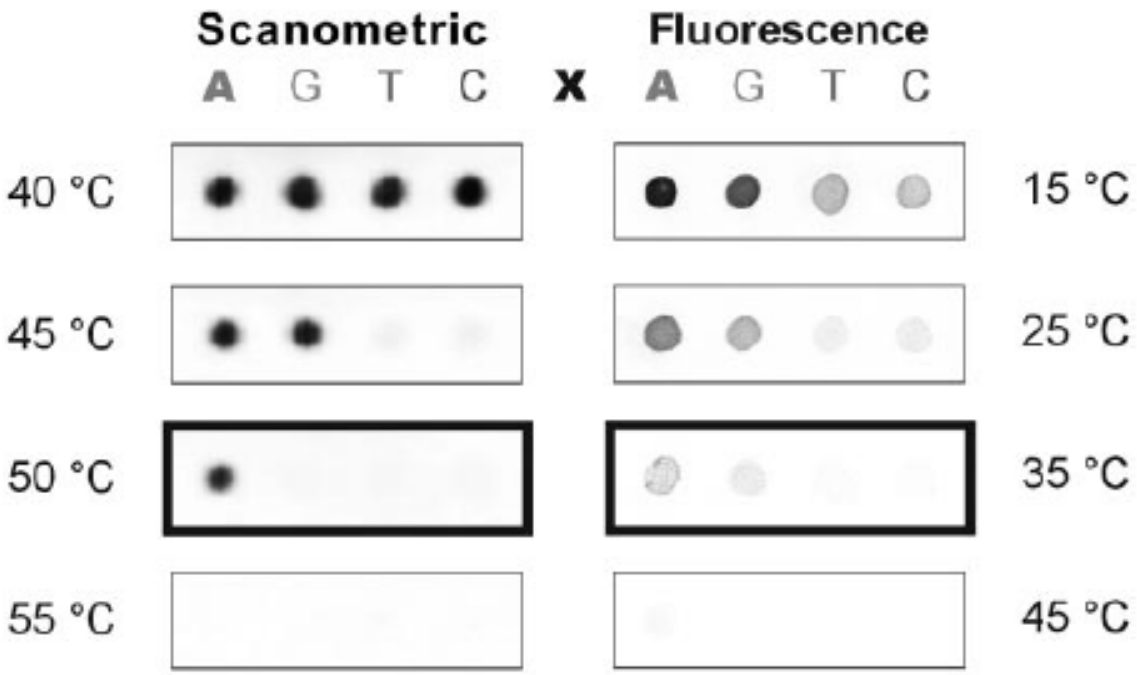

Fig. 3. (**Left**) Nanoparticle-labeled arrays developed at different stringency temperatures. Model oligonucleotide arrays (with the capture sequences shown in Scheme 1) were treated with oligonucleotide target and nanoparticle probes, followed by a 2-min buffer wash at the temperatures shown and subsequent silver amplification (*13*). Images were obtained with an Epson Expression 636 (600 dots per inch) flatbed scanner (Epson America, Long Beach, California). The darkened border indicates the array that showed optimum selectivity for the perfectly complementary target; at this temperature, the ratio of background-subtracted, 8-bit gray scale values for elements A:G:T:C, obtained from histogram averages in Adobe Photoshop (Adobe Systems, San Jose, California), is 96:9:7:6. (**Right**) Fluorophore-labeled arrays washed at different stringency temperatures. Model oligonucleotide arrays identical to those shown at left were treated with oligonucleotide target and Cy3-labeled oligonucleotide probes, followed by a 2-min buffer wash at the temperatures shown. Images were obtained with a ScanArray Confocal Microarray Scanner (GSI Lumonics, Billerica, Massachusetts). The darkened border indicates the array that showed the highest selectivity for the perfectly complementary target, as calculated by the QuantArray Analysis software package (GSI Lumonics); at this temperature, the intensity ratio (in percent, with the intensity of the X = A element at 15°C set to 100%) for elements A:G:T:C is 18:7:1:1.

Nanoparticles with Raman Spectroscopic Fingerprints for DNA and RNA Detection

YunWei Charles Cao, Rongchao Jin, Chad A. Mirkin*

30 AUGUST 2002 VOL 297 SCIENCE

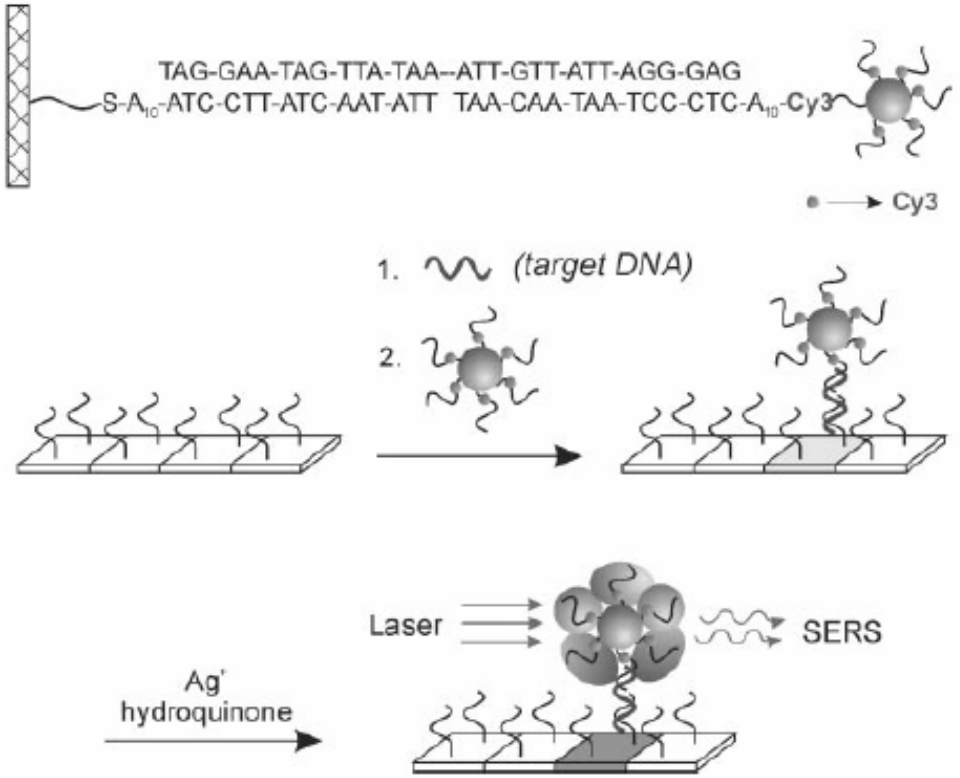

1 fM

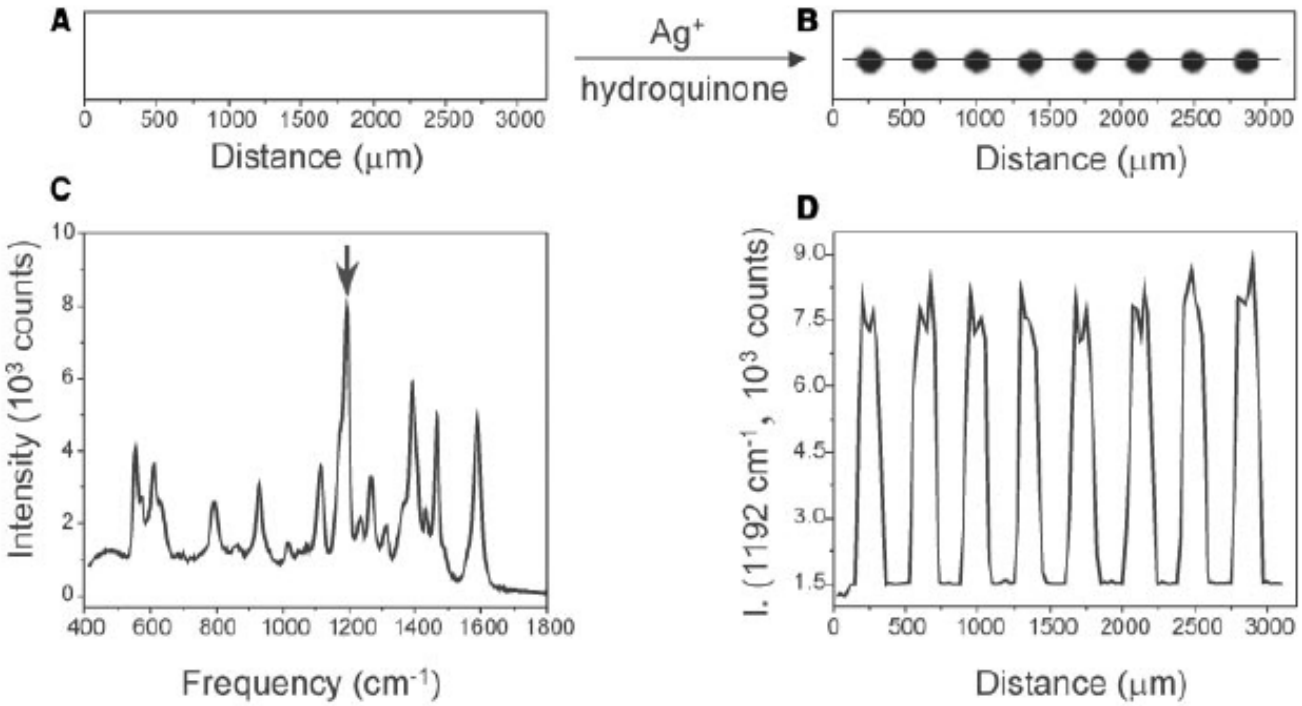

Fig. 1. Flatbed scanner images of microarrays hybridized with nanoparticles (**A**) before and (**B**) after Ag enhancing. (**C**) A typical Raman spectrum acquired from one of the Ag spots. (**D**) A profile of Raman intensity at 1192 cm^{-1} as a function of position on the chip; the laser beam from the Raman instrument is moved over the chip from left to right as defined by the line in (B).

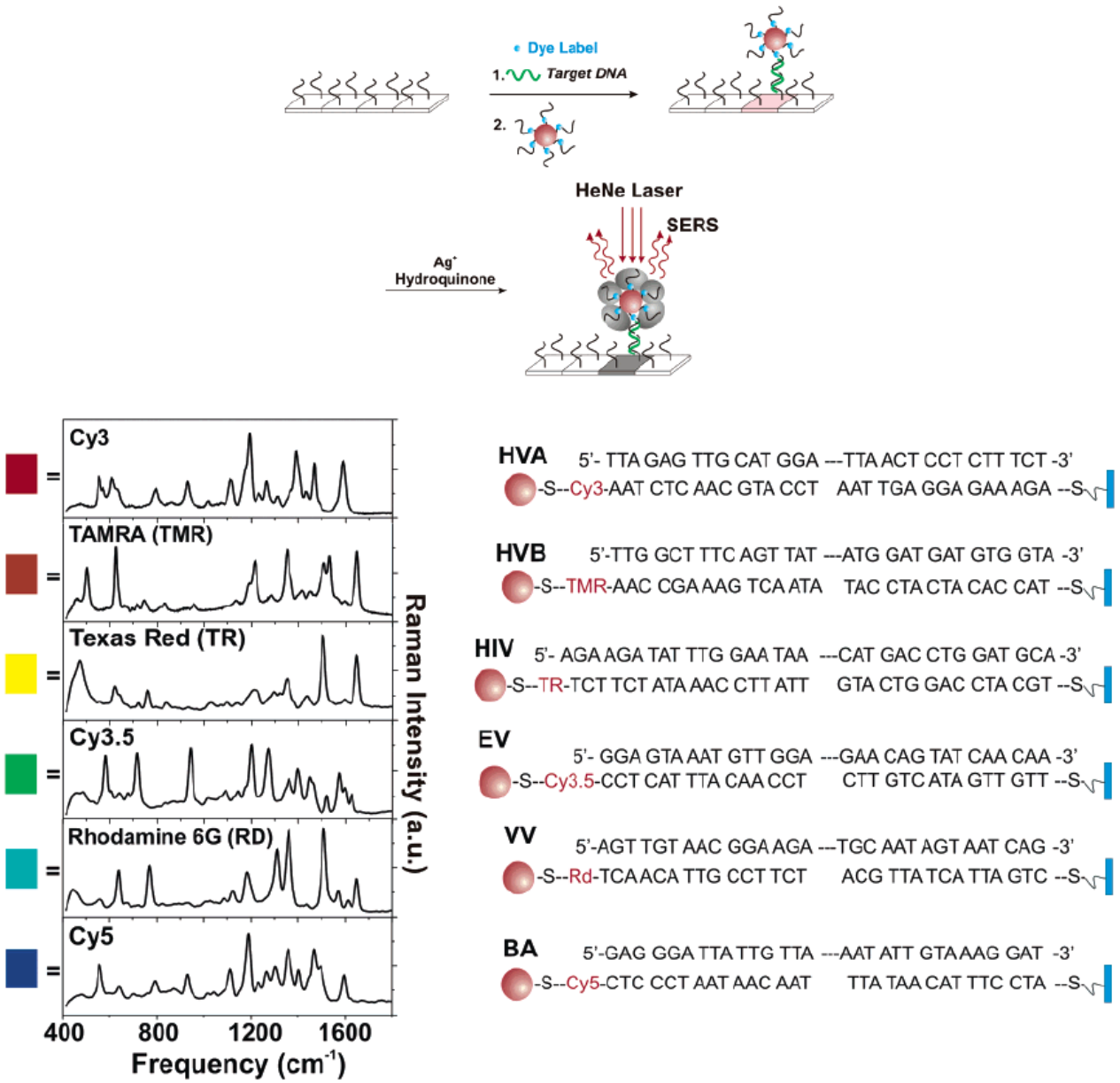

Figure 5. If Raman dyes (blue spheres) are attached to the labeling probe in the scanometric assay, the targets can be encoded and detected via the Raman signal of their labels. (Reprinted with permission from *Science* (http://www.aaas.org), ref 68. Copyright 2002 American Association for the Advancement of Science.)

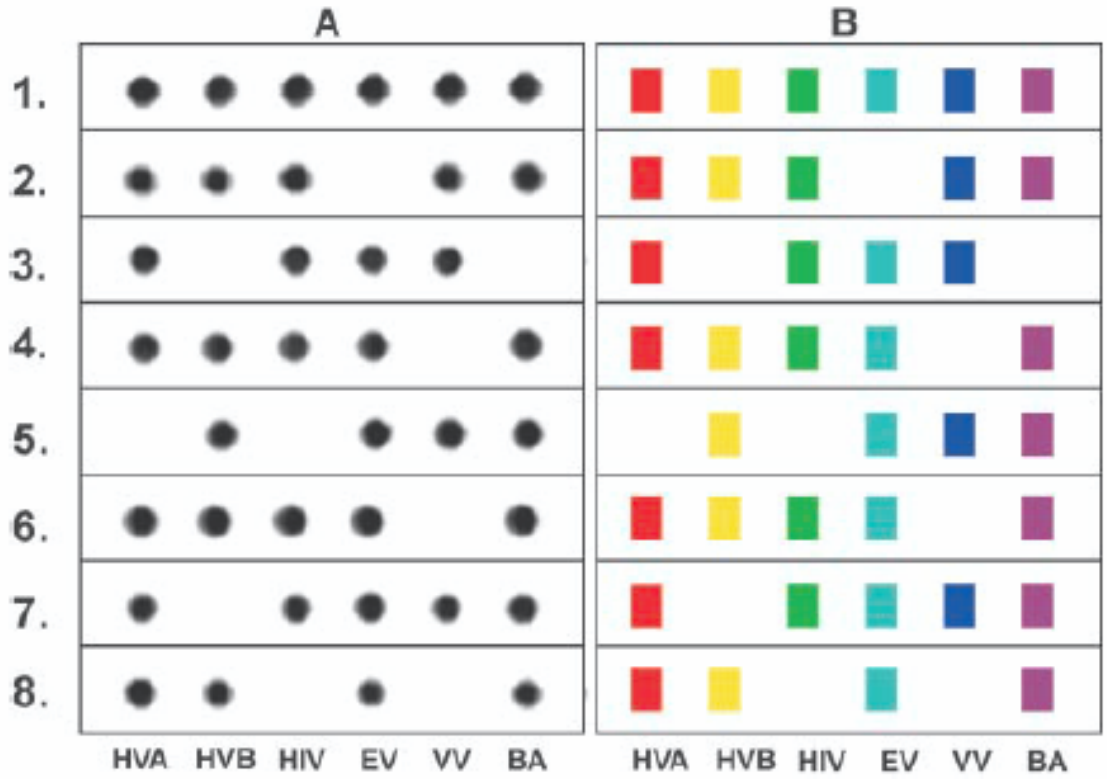

Fig. 3. (**A**) Flatbed scanner images of Ag-enhanced microarrays and (**B**) corresponding Raman spectra. The colored boxes correlate with the color-coded Raman spectra in Fig. 2. No false-positives or false-negatives were observed.

Bio-Bar-Code-Based DNA Detection with PCR-like Sensitivity

Jwa-Min Nam, Savka I. Stoeva, and Chad A. Mirkin*

J. AM. CHEM. SOC. 2004, *126*, 5932−5933

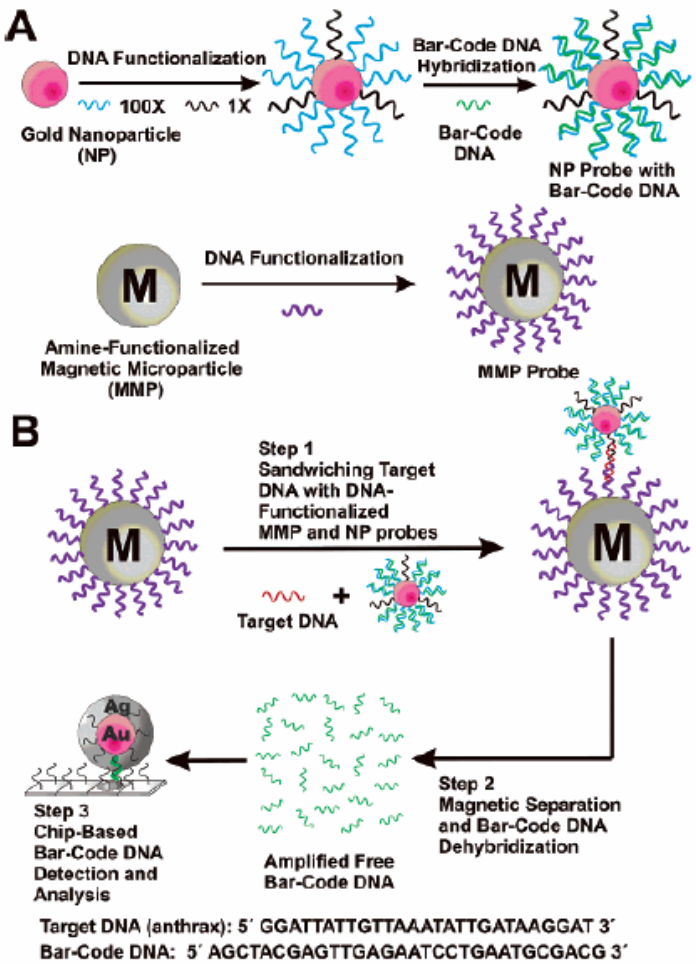

Figure 1. The DNA-BCA assay. (A) Nanoparticle and magnetic microparticle probe preparation. (B) Nanoparticle-based PCR-less DNA amplification scheme.

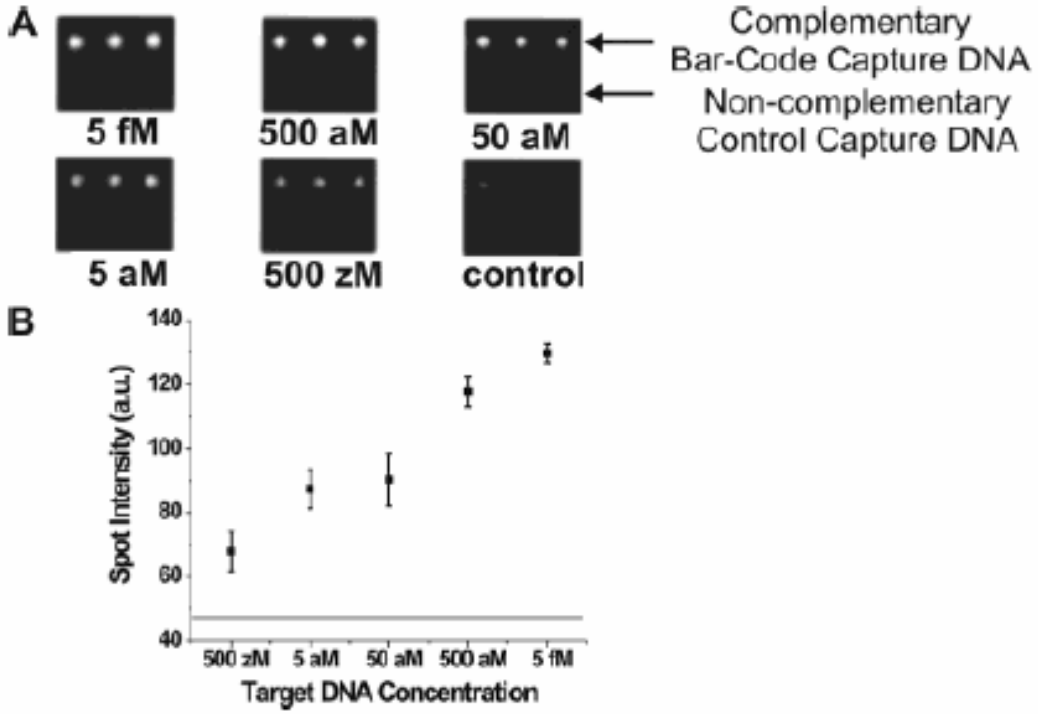

Figure 2. Amplified anthrax bar-code DNA detection with the Verigene ID system. (A) Anthrax bar-code DNA detection with 30 nm NP probes. (B) Quantitative data of spot intensities with 30 nm NP probes (Adobe Photoshop, Adobe Systems, Inc., San Jose, CA). The horizontal line represents control signal intensity (47 ± 2).

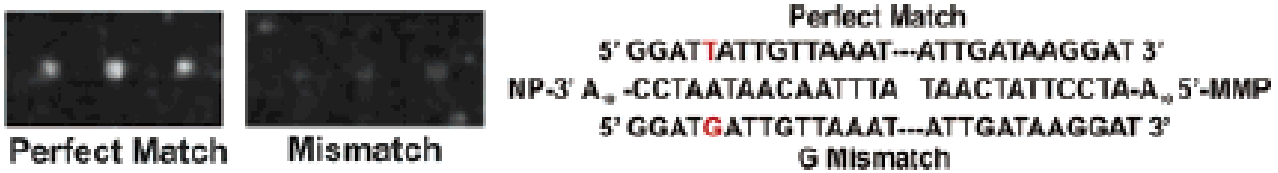

Figure 3. Single base mismatch experiment.

Nanoparticle-Based Bio–Bar Codes for the Ultrasensitive Detection of Proteins

26 SEPTEMBER 2003 VOL 301 SCIENCE

Jwa-Min Nam,* C. Shad Thaxton,* Chad A. Mirkin†

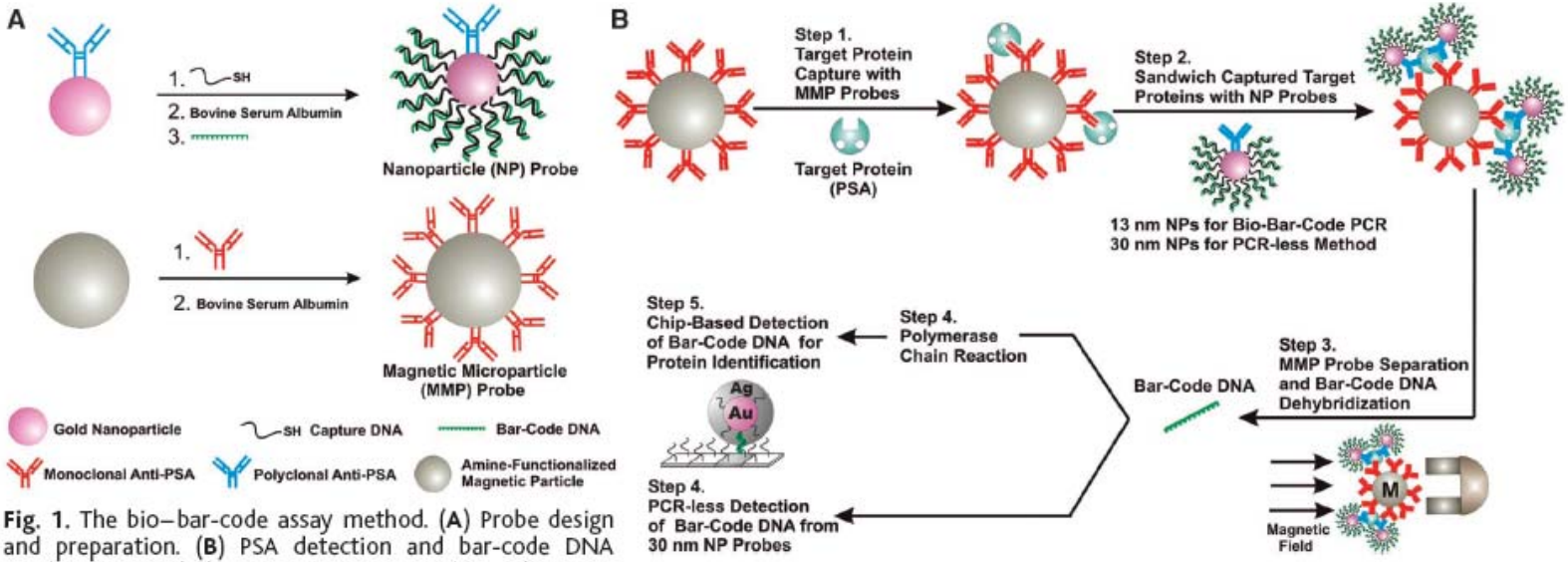

Fig. 1. The bio–bar-code assay method. (**A**) Probe design and preparation. (**B**) PSA detection and bar-code DNA amplification and identification. In a typical PSA-detection experiment, an aqueous dispersion of MMP probes functionalized with mAbs to PSA (50 μl of 3 mg/ml magnetic probe solution) was mixed with an aqueous solution of free PSA (10 μl of PSA) and stirred at 37°C for 30 min (Step 1). A 1.5-ml tube containing the assay solution was placed in a BioMag microcentrifuge tube separator (Polysciences, Incorporated, Warrington, PA) at room temperature. After 15 s, the MMP-PSA hybrids were concentrated on the wall of the tube. The supernatant (solution of unbound PSA molecules) was removed, and the MMPs were resuspended in 50 μl of 0.1 M phosphate-buffered saline (PBS) (repeated twice). The NP probes (for 13-nm NP probes, 50 μl at 1 nM; for 30-nm NP probes, 50 μl at 200 pM), functionalized with polyclonal Abs to PSA and hybridized bar-code DNA strands, were then added to the assay solution. The NPs reacted with the PSA immobilized on the MMPs and provided DNA strands for signal amplification and protein identification (Step 2). This solution was vigorously stirred at 37°C for 30 min. The MMPs were then washed with 0.1 M PBS with the magnetic separator to isolate the magnetic particles. This step was repeated four times, each time for 1 min, to remove everything but the MMPs (along with the PSA-bound NP probes). After the final wash step, the MMP probes were resuspended in NANOpure water (50 μl) for 2 min to dehybridize bar-code DNA strands from the nanoparticle probe surface. Dehybridized bar-code DNA was then easily separated and collected from the probes with the use of the magnetic separator (Step 3). For bar-code DNA amplification (Step 4), isolated bar-code DNA was added to a PCR reaction mixture (20-μl final volume) containing the appropriate primers, and the solution was then thermally cycled (*20*). The bar-code DNA amplicon was stained with ethidium bromide and mixed with gel-loading dye (*20*). Gel electrophoresis or scanometric DNA detection (*24*) was then performed to determine whether amplification had taken place. Primer amplification was ruled out with appropriate control experiments (*20*). Notice that the number of bound NP probes for each PSA is unknown and will depend upon target protein concentration.

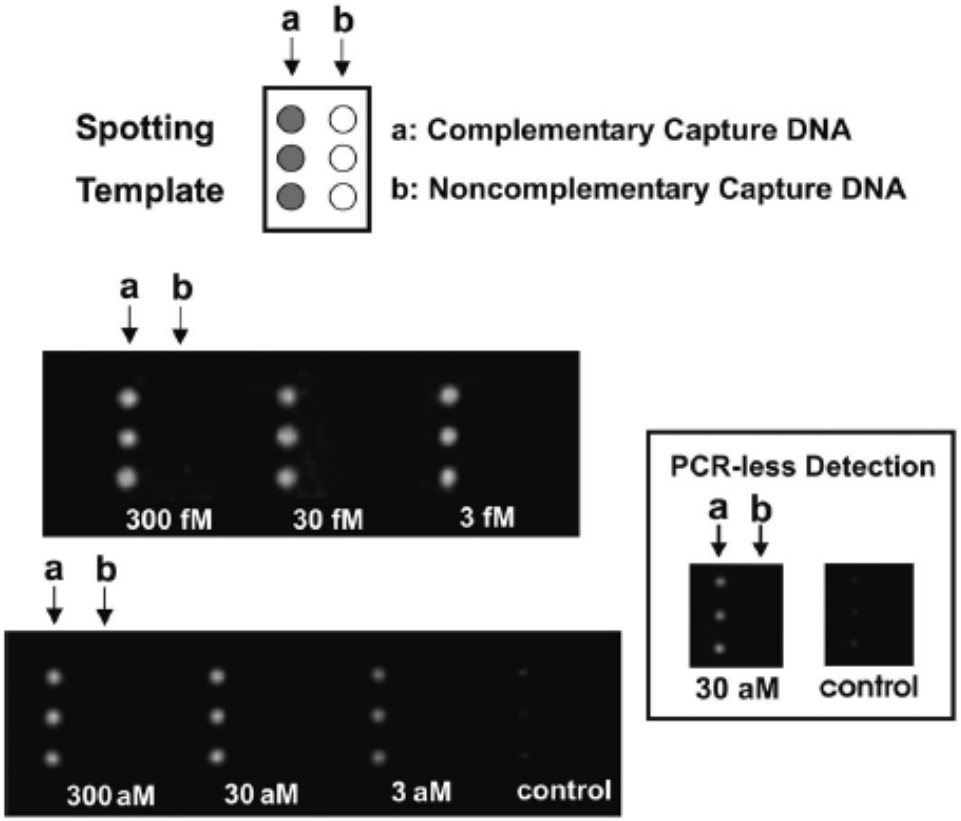

Fig. 2. Scanometric detection of PSA-specific bar-code DNA. PSA concentration (sample volume of 10 μl) was varied from 300 fM to 3 aM and a negative control sample where no PSA was added (control) is shown. For all seven samples, 2 μl of antidinitrophenyl (10 pM) and 2 μl of β-galactosidase (10 pM) were added as background proteins. Also shown is PCR-less detection of PSA (30 aM and control) with 30 nm NP probes (inset). Chips were imaged with the Verigene ID system (*20*).

Array-Based Electrical Detection of DNA with Nanoparticle Probes

So-Jung Park, T. Andrew Taton,* Chad A. Mirkin†

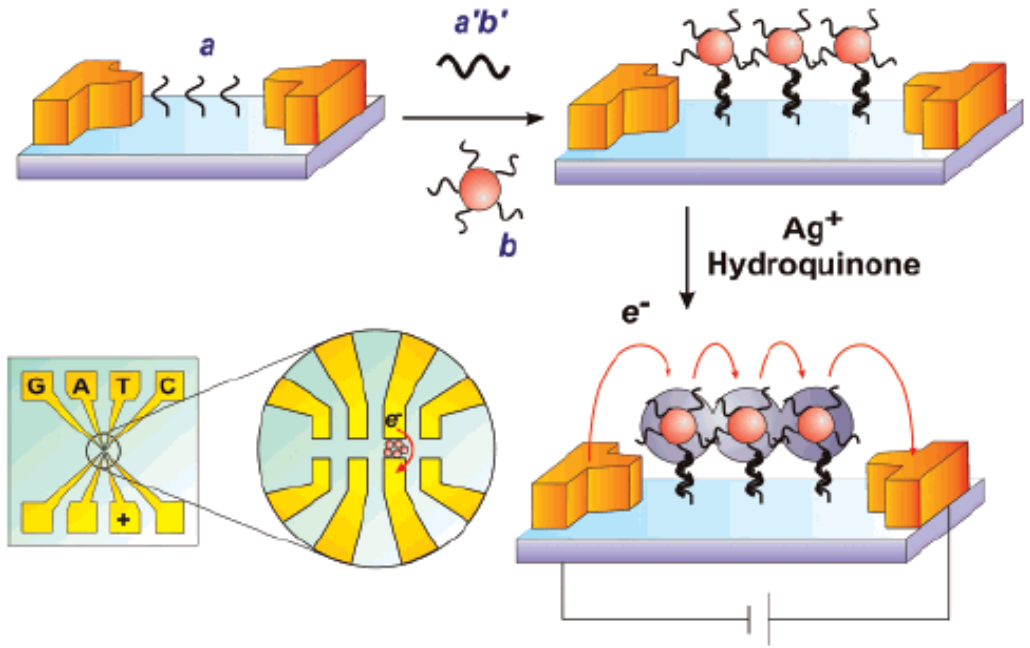

Figure 7. When the capture/target/probe sandwich is positioned in the gap between two electrodes, catalytic reduction of silver onto the sandwich system results in a signal that can be detected electrically. (Reprinted with permission from *Science* (http://www.aaas.org), ref 93. Copyright 2002 American Association for the Advancement of Science.)

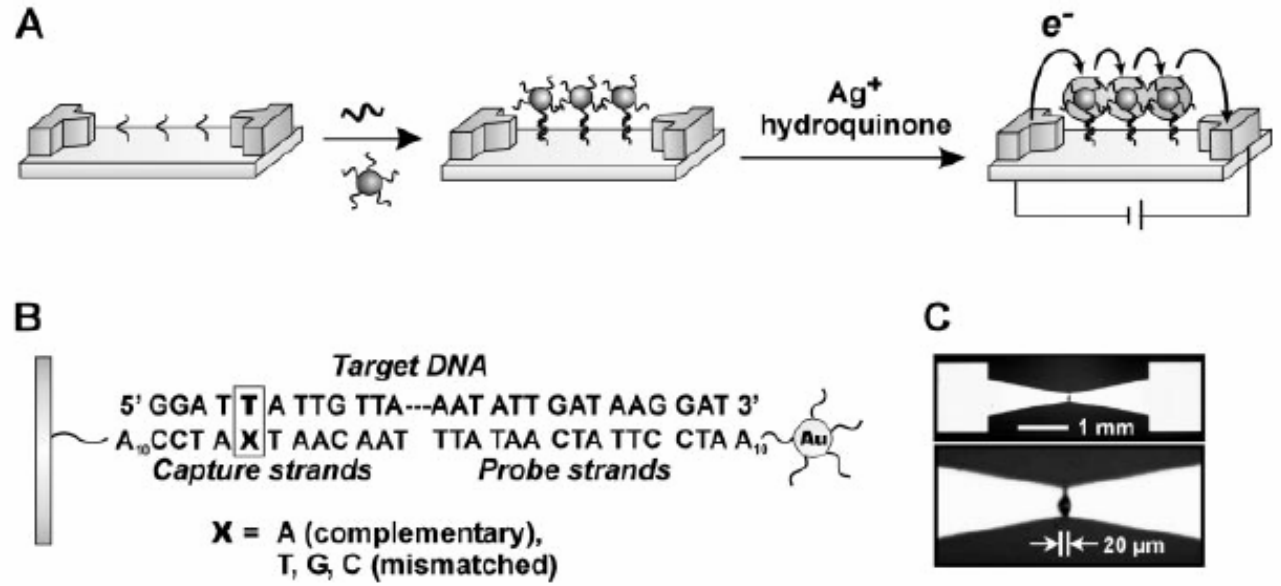

Fig. 1. (**A**) Scheme showing concept behind electrical detection of DNA. (**B**) Sequences of capture, target, and probe DNA strands. (**C**) Optical microscope images of the electrodes used in a typical detection experiment. The spot in the electrode gap in the high-magnification image is food dye spotted by a robotic arrayer (GMS 417 Microarrayer, Genetic Microsystems, Woburn, MA).

Table 1. Detection Limits of Nucleic Acid Assays[a]

	assay	ss DNA	PCR products	genomic DNA
nanostructure-based methods	colorimetric[29] (cross-linked Au nanoparticles)	~10 nM		
	colorimetric[36] (non-cross-linked Au nanoparticles)	60 nM		
	magnetic relaxation[97] (iron oxide nanoparticles)	20 pM		
	electrochemical[96] (nanoparticles)	270 pM		
	scanometric[35,66,67] (Au nanoparticles with Ag amplification)	50 fM	100 aM[b]	200 fM
	Raman spectroscopy[68] (Au nanoparticles with Ag amplification)	~1 fM		
	electrical[93] (Au nanoparticles with Ag amplification)	500 fM		
	electrical[99] (Si nanowire)	10 fM		
	electrical[103] (carbon nanotube)	54 aM		
	resonant light-scattering[61−66] (metal nanoparticles)	170 fM[b]		33 fM
	fluorescence[56] (ZnS and CdSe quantum dots)	2 nM		
	surface plasmon resonance[41] (Au nanoparticles)	10 pM		
	quartz crystal microbalance[94] (Au nanoparticles)	~1 fM		
	laser diffraction[42] (Au nanoparticles)	~50 fM		
	fluorescence[45] (fluorescent nanoparticles)	~1 fM		
	bio-bar-code amplification[71] (Au nanoparticles with Ag amplification)	500 zM		
other non-enzymatic based methods	fluorescence[35] (molecular fluorophores)		~600 fM[b]	
	fluorescence (dendrimer amplification)[134]		2.5 μg	
	electrochemical amplification[136] (electroactive reporter molecules)	100 aM		

[a] Detection limits can vary based on target length and sequence; therefore, it is difficult to compare assays without testing them using identical targets and conditions. [b] Values taken from ref 34.

Table 2. Detection Limits of Protein Assays

	assay	target	protein in saline	protein in serum
nanostructure-based methods	optical[72] (Au nanoshells)	rabbit IgG	0.88 ng/mL (~4.4 pM)[a]	0.88 ng/mL (~4.4 pM)[a]
	optical[74] (Au nanoparticles)	IgE and IgG1	~20 nM	
	magnetic relaxation[98] (iron oxide nanoparticles)	adenovirus (ADV) and herpes simplex virus (HSV)	100 ADV/ 100μL	50 HSV/ 100 μL
	scanometric[79] (Au nanoparticles with Ag amplification)	mouse IgG	200 pM	
	Raman[82] (Au nanoparticles with Raman labels)	prostate-specific antigen		30 fM
	surface plasmon resonance[83,84] (triangular Ag particles on surfaces)	streptavidin(S A) and anti-biotin (AB)	~1 pM SA and ~700 pM AB	
	electrical[110] (single-walled carbon nanotubes)	10E3 antibody to U1A RNA splicing factor	~1 nM	
	electrical[20] (Si nanowires)	streptavidin	10 pM	
	bio-bar-code amplification[75] (Au nanoparticles with Ag amplification)	prostate-specific antigen	30 aM (3 aM)[b]	(30 aM)[b]
molecular fluorophore methods	enzyme-linked immunosorbent assay	various	pM range	pM range
electrochemical methods	electrochemical amplification[137] (oligonucleotide reporter molecules)	IgG	13 fM	
enzyme-based amplification methods	immuno-PCR[76]	bovine serum albumin	2 fM	
	rolling circle amplification[77]	prostate-specific antigen	3 fM	

[a] Reported in ng/mL; authors converted to molar concentration for ease of comparison. [b] These values are the lower limits when PCR is used to amplify the bar-code DNA prior to scanometric detection of bar codes.

Applications of Quantum Dots in Biology

An Overview

Charles Z. Hotz

- Size dependent emission spectra
- Single excitation
- Higher photostability
- Narrow emission peak
- Low toxicity for coated quantum dots

Nucleation and Growth of CdSe on ZnS Quantum Crystallite Seeds, and Vice Versa, in Inverse Micelle Media

A. R. Kortan, R. Hull, R. L. Opila, M. G. Bawendi, M. L. Steigerwald, P. J. Carroll, and L. E. Brus*

Contribution from AT&T Bell Laboratories, Murray Hill, New Jersey 07974.
Received June 20, 1989

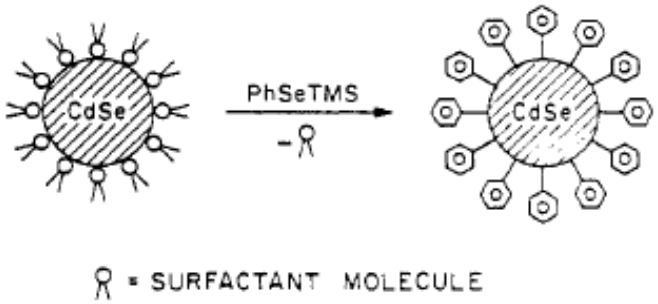

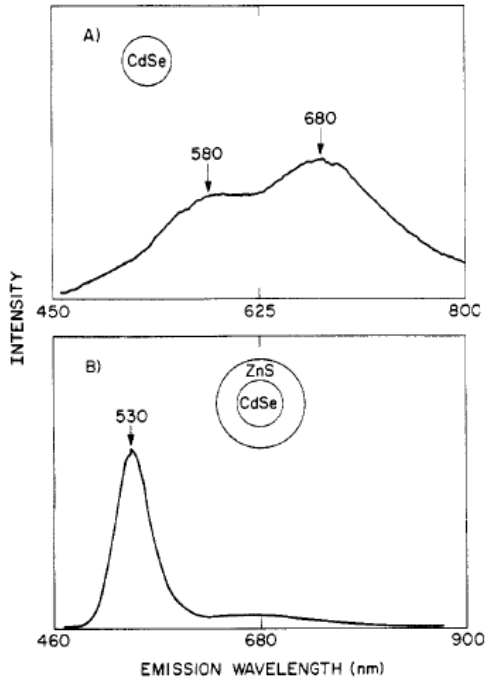

Figure 2. Room temperature luminescence spectra after annealing: (A) (CdSe)Ph, (B) $(CdSe)_1(ZnS)_4Ph$. The integrated quantum yield in B is more than an order of magnitude higher than in A.

Semiconductor Nanocrystals as Fluorescent Biological Labels

Marcel Bruchez Jr., Mario Moronne, Peter Gin, Shimon Weiss,*
A. Paul Alivisatos*

SCIENCE VOL 281 25 SEPTEMBER 1998

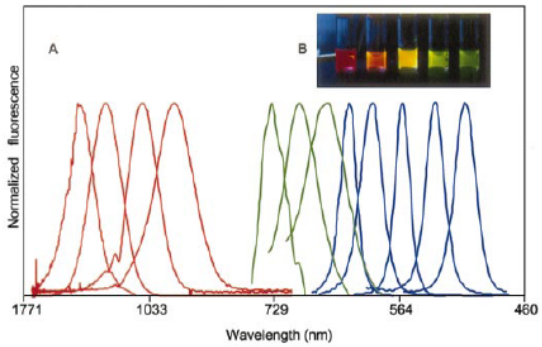

Fig. 2. (**A**) Size- and material-dependent emission spectra of several surfactant-coated semiconductor nanocrystals in a variety of sizes. The blue series represents different sizes of CdSe nanocrystals (*16*) with diameters of 2.1, 2.4, 3.1, 3.6, and 4.6 nm (from right to left). The green series is of InP nanocrystals (*26*) with diameters of 3.0, 3.5, and 4.6 nm. The red series is of InAs nanocrystals (*16*) with diameters of 2.8, 3.6, 4.6, and 6.0 nm. (**B**) A true-color image of a series of silica-coated core (CdSe)–shell (ZnS or CdS) nanocrystal probes in aqueous buffer, all illuminated simultaneously with a handheld ultraviolet lamp.

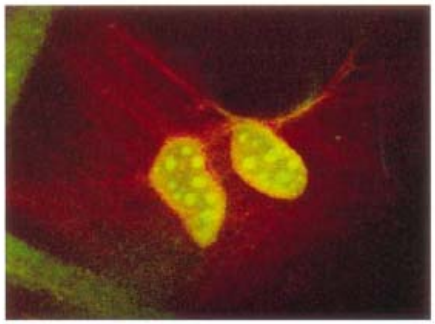

Fig. 3. Cross section of a dual-labeled sample examined with a Bio-Rad 1024 MRC laser-scanning confocal microscope with a 40× oil 1.3 numerical aperture objective. The mouse 3T3 fibroblasts were grown and prepared as described in (*27*). A false-colored image was obtained with 363-nm excitation, with simultaneous two-channel detection (522DF 35-nm FWHM narrow-pass filter for the green, and a 585-nm long-pass filter for the red). Image width: 84 μm.

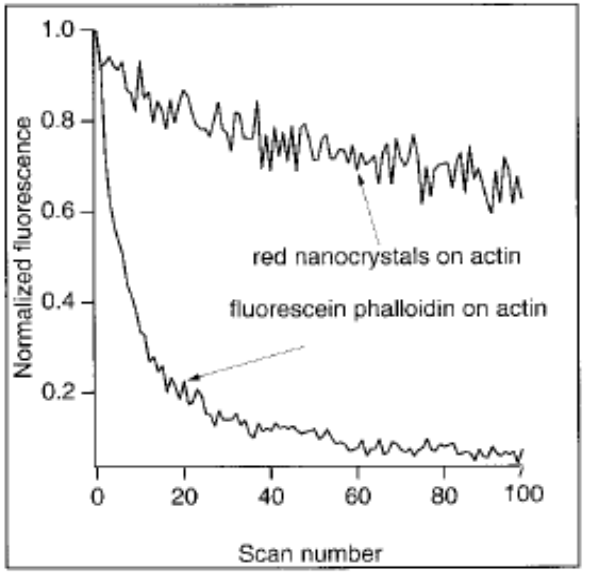

Fig. 4. Sequential scan photostability comparison of fluorescein-phalloidin–labeled actin fibers compared with nanocrystal-labeled actin fibers. Fluorescein was excited at 488 nm and the nanocrystals at 363 nm by a laser scanning confocal microscope with a 12-μs dwell time and ~20-mW power for each laser. The average intensity of four pixels was followed in each sample through 100 successive scans and normalized to its initial value. The intensity of the fluorescein drops quickly to autofluorescence levels, whereas the intensity of the nanocrystals drops only slightly.

Quantum Dot Bioconjugates for Ultrasensitive Nonisotopic Detection

Warren C. W. Chan and Shuming Nie*

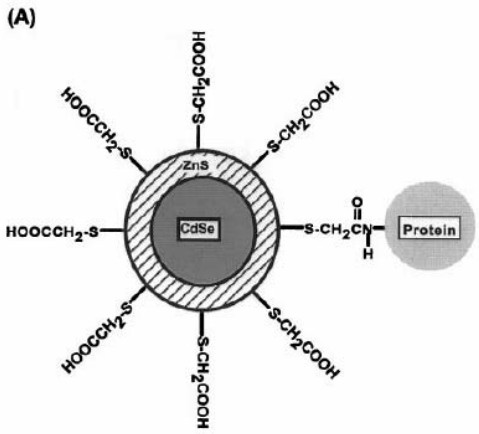

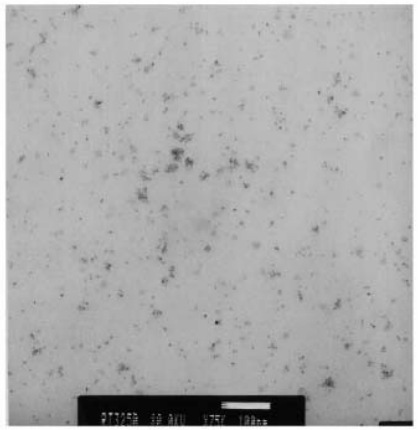

Fig. 1. (**A**) Schematic of a ZnS-capped CdSe QD that is covalently coupled to a protein by mercaptoacetic acid. (**B**) TEM of QD-transferrin (an iron-transport protein) conjugates. Scale bar, 100 nm. Clusters of closely spaced particles were mainly formed by sample spreading and drying on the carbon grid and not by chemical cross-linking. ZnS-capped QDs with a CdSe core size of 4.2 nm were prepared according to the procedure developed by Hines and Guyot-Sionnest (*7*). The colloidal QDs were dissolved in chloroform and were reacted with glacial mercaptoacetic acid (~1.0 M) for 2 hours. An aqueous phosphate-buffered saline (PBS) solution (pH 7.4) was added to this reaction mixture at a 1:1 volume ratio. After vigorous shaking and mixing, the chloroform and water layers separated spontaneously. The aqueous layer, which contained mercapto-coated QDs, was extracted. Excess mercaptoacetic acid was removed by four or more rounds of centrifugation. The purified QDs were conjugated to transferrin and IgG with the cross-linking reagent ethyl-3-(dimethyl-aminopropyl)carbodiimide. Standard protocols were followed (*16*), except the excess proteins were removed by repeated centrifugation. The purified conjugates were stored in PBS at room temperature.

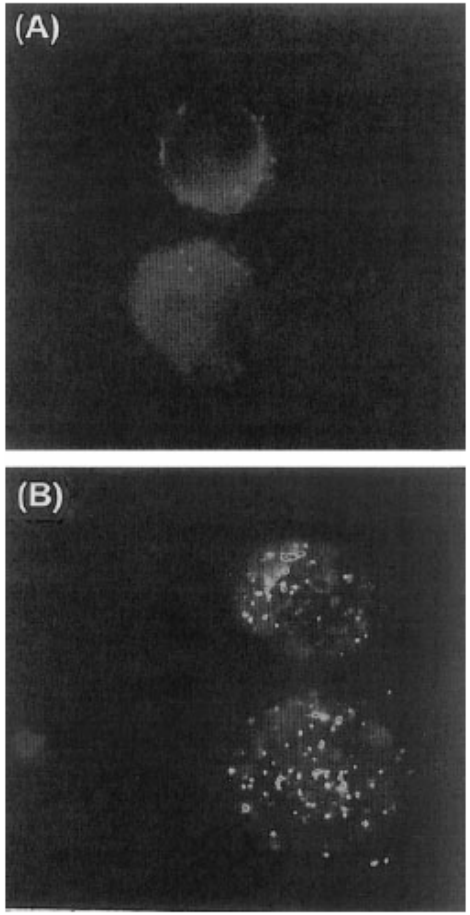

Fig. 4. Luminescence images of cultured HeLa cells that were incubated with (**A**) mercapto-QDs and (**B**) QD-transferrin conjugates. The QD bioconjugates were transported into the cell by receptor-mediated endocytosis and were detected as clusters or aggregates. Luminescence "blinking" was not observed for these clusters because of statistical averaging. The images were obtained with an epifluorescence microscope that was equipped with a high-resolution CCD camera (1.4 million pixels) (Photometrix, Tucson, Arizona) and a 100-W Hg excitation lamp. HeLa cells were grown in a minimum essential medium containing 10% fetal calf serum, 1% antibiotics (penicillin and streptomycin), and fungizone. The cultured cells were incubated overnight with either control QDs or the transferrin conjugates at 37°C. After repeated washings to eliminate excess QDs, the cells were removed from the petri dish and placed on a glass cover slip for imaging. The trypsin-treated cells had a spherical shape on the cover slip. Cell diameter, ~10 μm.

Optical Properties

- Broadband Absorption
  - Single laser excitation
- Sharp Emission
  - 20-30 nm symmetric emission
- High Quantum Yield
  - 20 x more than R6G
- Good Photostability
  - 100 x more stable for R6G (4 Hrs vs 10 mins)
- Loner fluorescent lifetime (20-40 ns vs 5 ns)

Structure

- Core quantum dot
  - CdSe, hydrophobic, not stable, lower QE (~5%)
  - Defects =>Trap state
- Core-shell quantum dot
  - ZnS/CdSe, hydrophobic, stable, higher QE (~50%)
  - Coated with higher bandgap materials or passivation reduces defects
- Water soluble quantum dot
  - Hydrophilic polymer coating
- Quantum dot bioconjugation
  - Bioconjugate to hydrophilic quantum dot

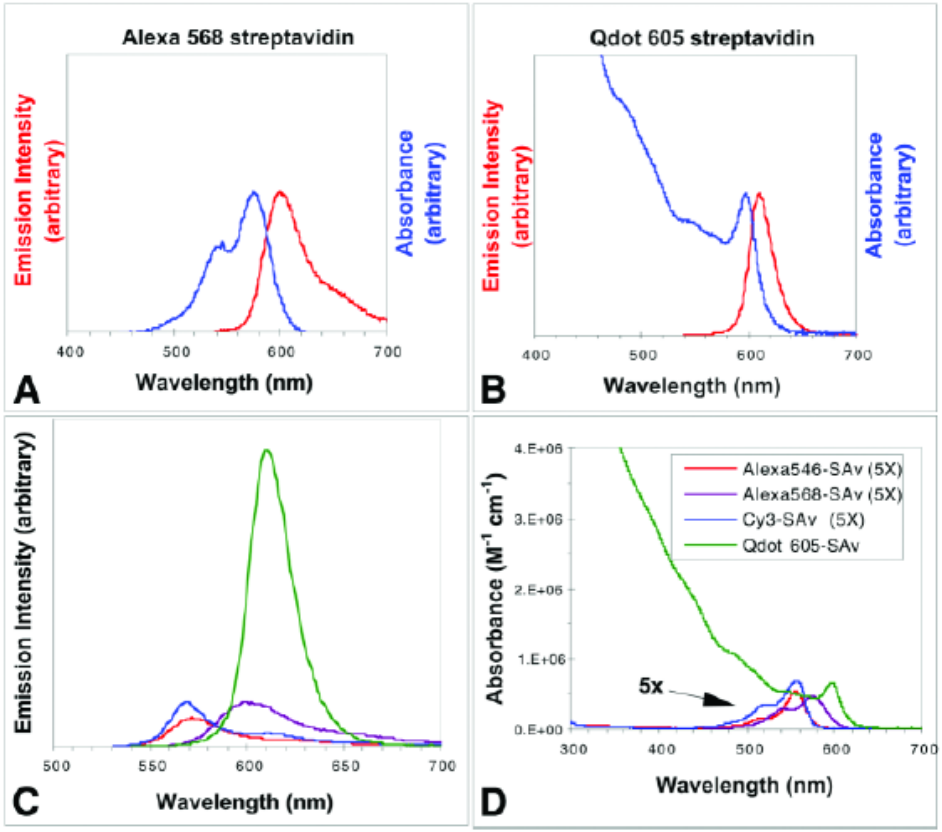

Fig. 1. Comparison of absorbance and emission spectra (normalized) of **(A)** Alexa® 568 streptavidin conjugate and **(B)** Qdot® 605 streptavidin conjugate. Note that the quantum dot conjugate can absorb light efficiently far to the blue of the emission. **(C)** Comparison of emission spectra (nonnormalized) of streptavidin conjugates of Qdot 605 (—), Alexa 546 (—), Alexa 568 (—), and Cy3® (—). The spectra were taken under conditions in which each fluorophore absorbed the same amount of excitation light. The measured quantum yields of the conjugates were 55, 8, 16, and 11%, respectively. **(D)** Comparison of absorbance spectra (nonnormalized, each 1 μ*M* flurophore) of Qdot 605 streptavidin conjugate (—), Cy3 streptavidin conjugate (—), Alexa 546 streptavidin conjugate (—), and Alexa 568 streptavidin conjugate (—). Note that all dye spectra are enhanced fivefold for clarity. Alexa, Cy3, and Qdot are registered trademarks of Molecular Probes, Amersham Biosciences, and Quantum Dot Corporation, respectively.

Table 1
Optical Properties of Quantum Dots Compared to Common Dyes[a]

Fluorescent dye	$\lambda_{excitation}$ (nm)	$\lambda_{emission}$ (nm)	$\varepsilon(mol^{-1}\text{-}cm^{-1})$
Qdot 525	400	525	280,000
Alexa 488	495	519	78,000
Fluorescein	494	518	79,000
Qdot 565	400	565	960,000
Cy3	550	570	130,000
Alexa 555	555	565	112,000
Qdot 585	400	585	1,840,000
R-Phycoerythrin	565	578	1,960,000
TMR	555	580	90,000
Qdot 605	400	605	2,320,000
Alexa 568	578	603	88,000
Texas Red	595	615	96,000
Qdot 655	400	655	4,720,000
APC	650	660	700,000
Alexa 647	650	668	250,000
Cy5	649	670	200,000
Alexa 647-PE	565	668	1,960,000

[a]The extinction coefficients (ε) are generally much larger for quantum dots than for fluorescent dyes. Furthermore, the excitation wavelength ($\lambda_{excitation}$) can be much farther from the emission ($\lambda_{emission}$).

Photo Stability

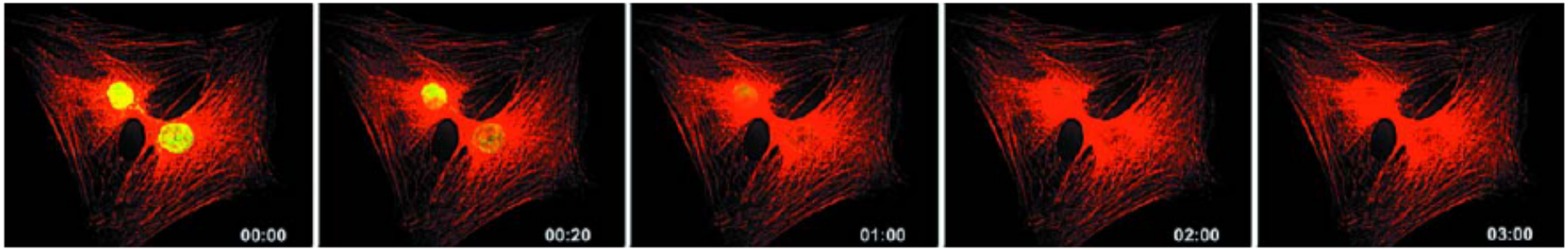

Fig. 2. Comparison of photostability between Qdot® 605 and Alexa Fluor® 488 streptavidin conjugates. Actin filaments in two 3T3 mouse fibroblast cells were labeled with Qdot 605 streptavidin conjugate (red), and the nuclei were stained with Alexa Fluor 488 streptavidin (green). The specimens were continuously illuminated for 3 min with light from a 100-W mercury lamp under a ×100 1.30 oil objective. An excitation filter (excitation: 485 ± 20 nm) was used to excite both Alexa 488 and Qdot 605. Emission filters (emission: 535 ± 10 and em 605 ± 10 nm) on a motorized filter wheel were used to collect Alexa 488 and Qdot 605 signals, respectively. Images were captured with a cooled charge-coupled device camera at 10-s intervals for each color automatically. Images at 0, 20, 60, 120, and 180 s are shown. Whereas Alexa 488 labeling signal faded quickly and became undetectable within 2 min, the Qdot 605 signal showed no obvious change for the entire 3-min illumination period.

Multiplexing by Q-dot

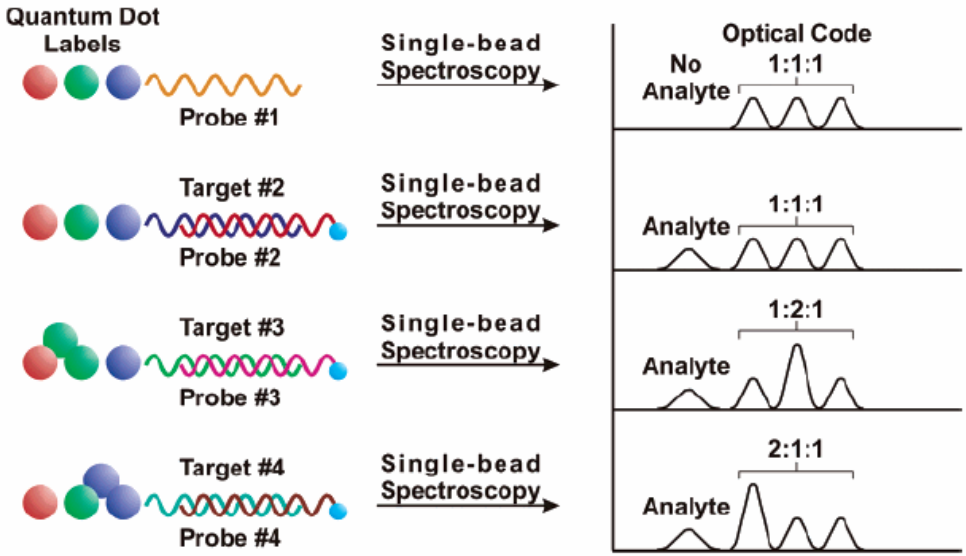

Figure 3. Quantum dots can be employed for detecting multiple targets in a single assay. Specifically, varying the numbers and ratios of different quantum dots per target results in a unique fluorescent signal for each individual target. (Reprinted with permission of Nature Publishing Group. *Nature Biotech.*, Vol. 19, 2001, by Nie, et al.)

Encoding

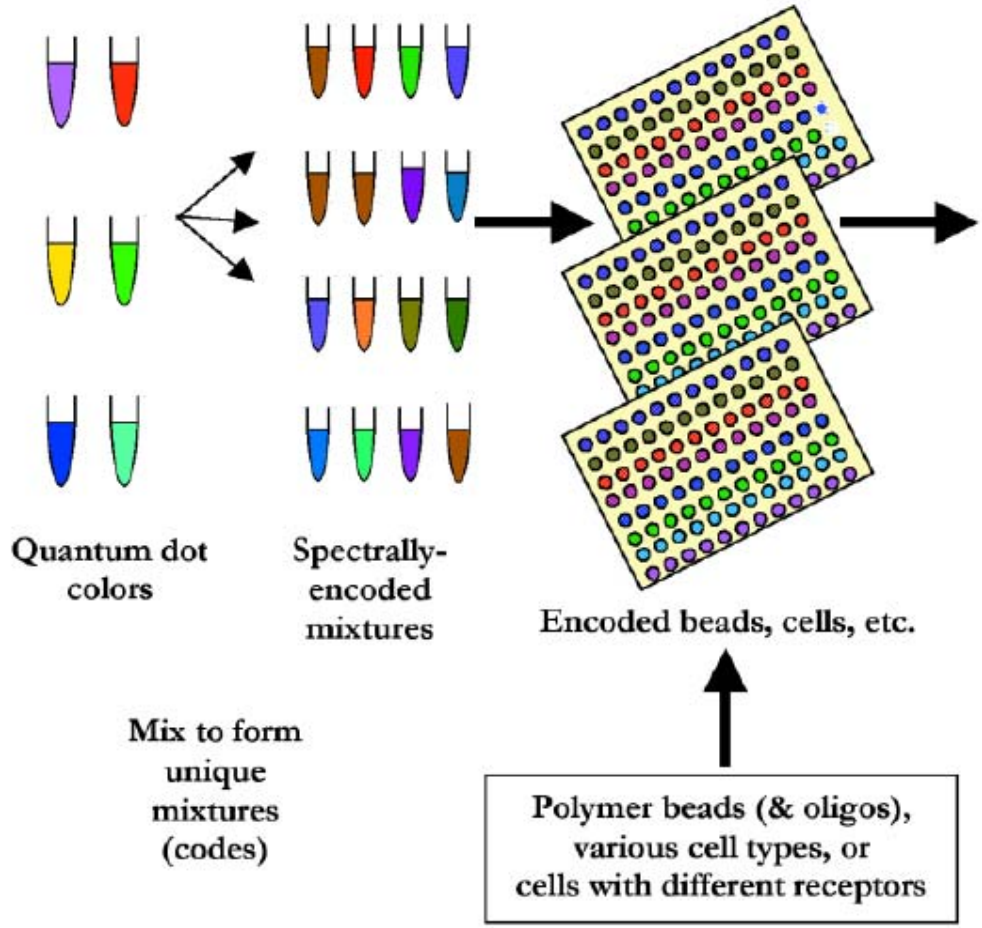

Application	Format
Multiplexed gene expression	Encoded beads each with gene-specific oligos
Multiplexed SNP genotyping	Encoded beads with allele-specific oligos
Multiplexed immunoassays	Encoded beads with antibodies
Multiplexed cell-based assays	Mixed cell types encoded with quantum dots
Multiplexed reporter assays	Encoded cell lines expressing various receptors

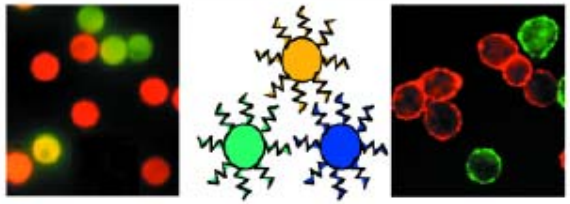

Fig. 6. Concept of encoding using quantum dots. Quantum dot colors can be mixed to produce spectral codes. These mixtures can be combined with polymer beads to produce encoded beads that can be subsequently coupled to distinct oligonucleotides or other affinity molecules. Alternatively, the quantum dot spectral codes can be used to label cells to differentiate cell lines, or cell lines bearing different receptors. SNP, single nucleotide polymorphism.

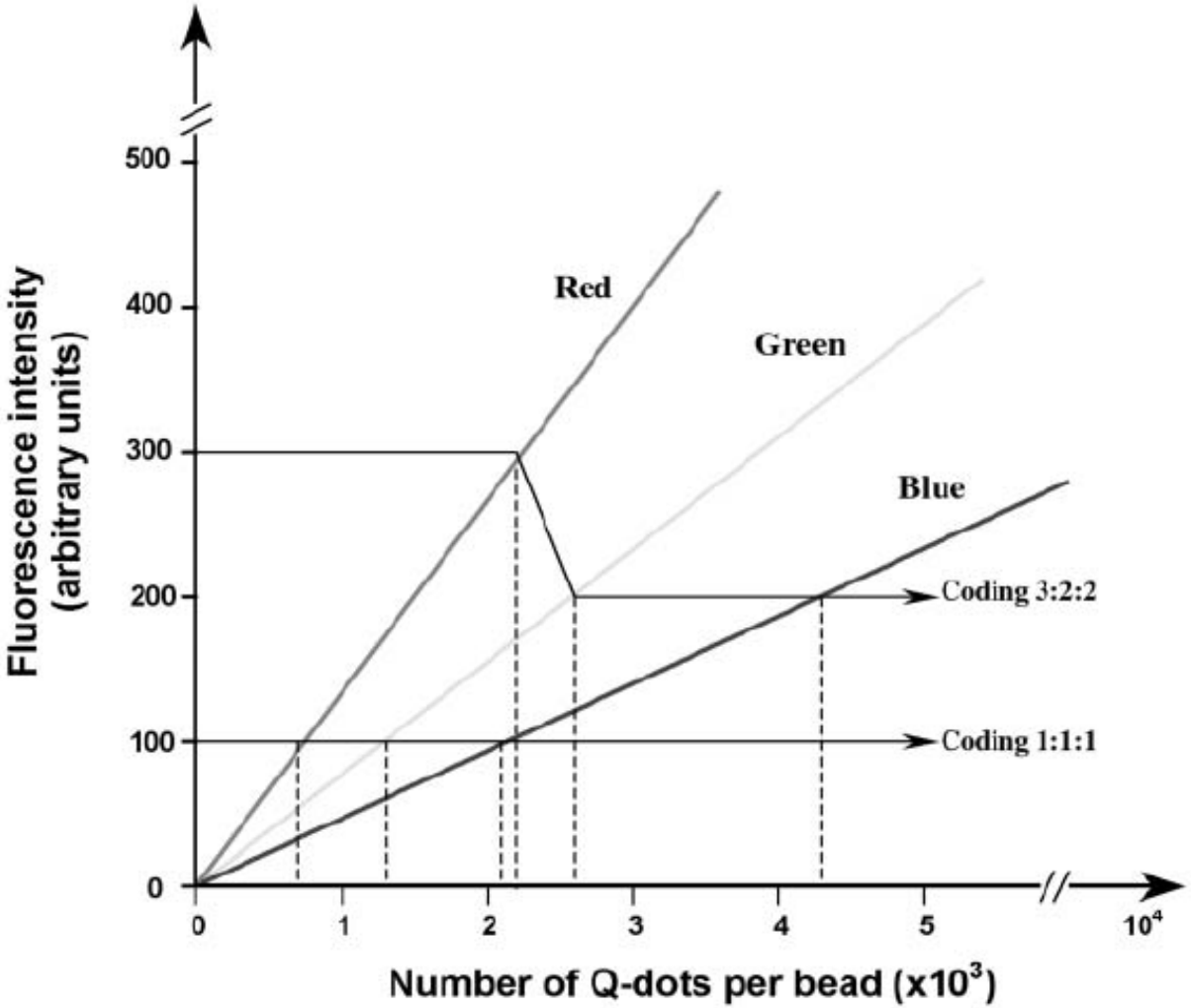

Fig. 1. Schematic drawing of working curves for preparation of multicolor quantum dot microbeads. Arrows depict two representative beads coded with intensity ratios of 1 : 1 : 1 and 3 : 2 : 2, and the number of quantum dots (or concentration) can be obtained from the x axis. Each single bead may contain quantum dots (Q-dots) ranging from several hundred to millions, depending on the bead size and surface area.

Cell Culture

In the remainder of this section, each step was performed using aseptic technique inside a laminar flow hood (*see* **Note 2**). Ten milliliters of medium was transferred by pipet into each labeled flask. Thawed vials were then sterilized by swabbing with alcohol. The vials were slowly opened, and the medium with the cells was transferred by pipet into the appropriately labeled flask. The flasks were next placed in a 37°C incubator at 5% CO_2, and the cells were allowed to grow until confluent.

Once confluent, the medium was aspirated off and the cells well rinsed with PBS, and then 3 mL of 0.1% trypsin was added. After approx 1 to 2 min, or when the cells began to round up and detach, 3 mL of medium was added to disperse the cells and to inhibit the trypsin (*see* **Note 3**). Cells from each flask were then transferred to an appropriately labeled 50-mL conical tube and centrifuged at 500*g* for 5 min. The supernatant was aspirated off, and the cells were resuspended in fresh medium.

Using a hemacytometer, the cells were counted and their concentration was determined (*see* **Note 4**). The cell solution was next diluted to 1×10^5 cells/mL and 150 µL was added to the glass cover slip of poly-D-lysine-coated sterile MatTek microwell dishes. The cells were incubated at 37°C with 5% CO_2 for 3 h to allow the cells to attach. Once the cells had attached, 2 mL of additional medium was added to the dish. The dishes were then returned to the incubator and allowed to grow for 3 d or until 50% confluent.

Hemacytometer

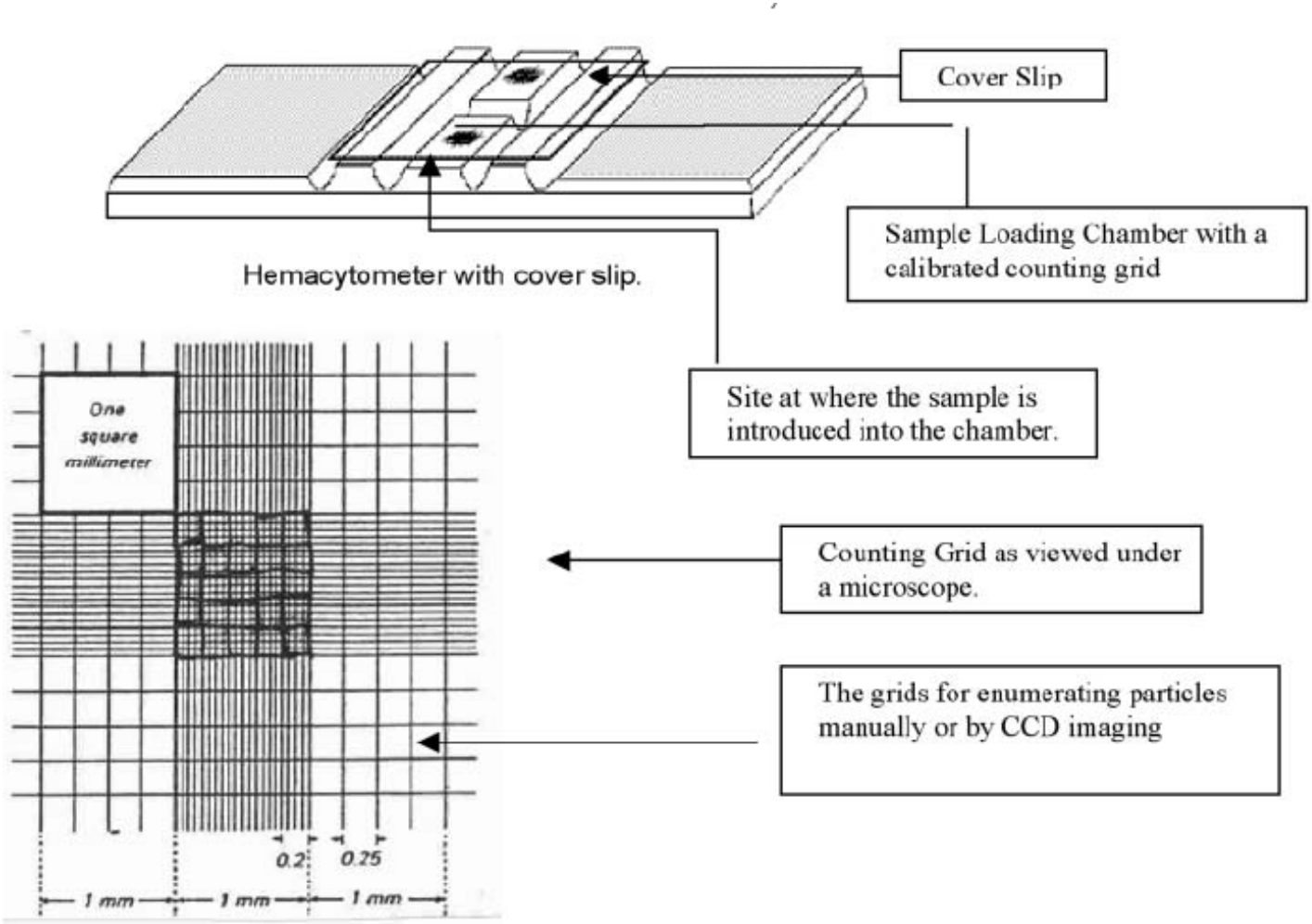

Fig. 3. Layout of hemacytometer.

Fluorescence Imaging Scheme

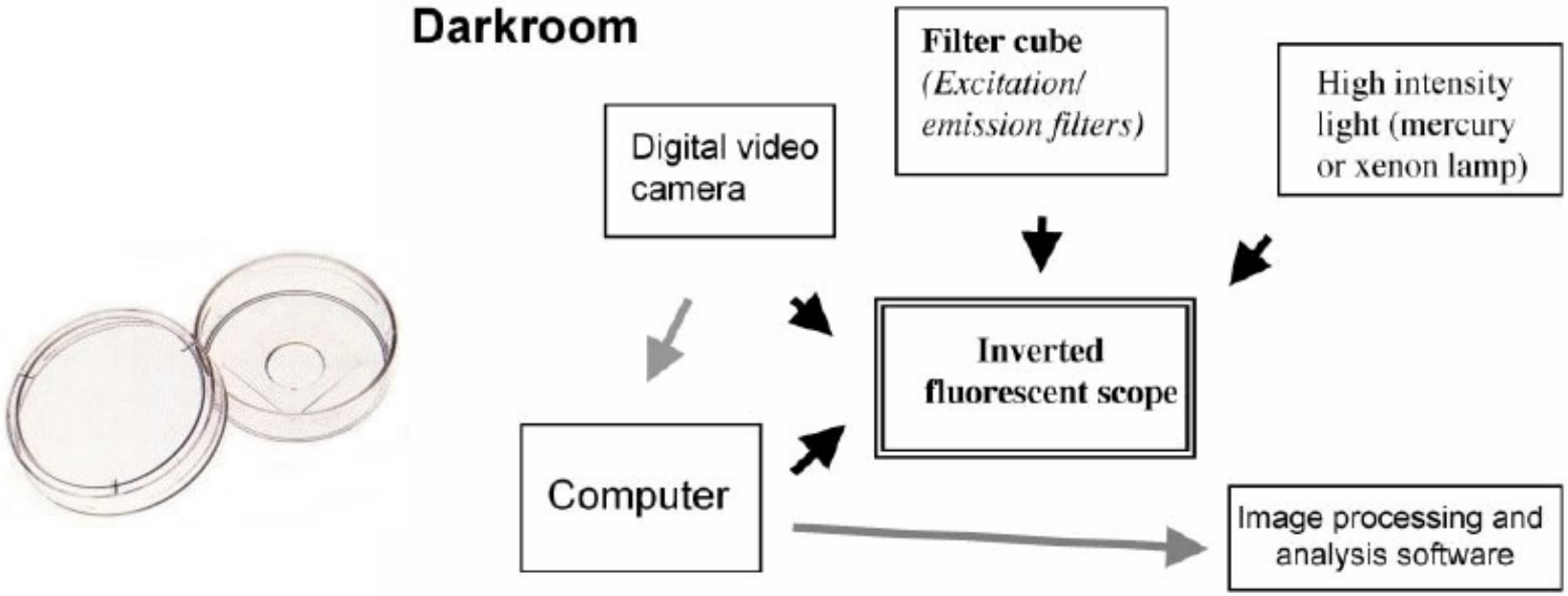

Fig. 2. Components required for fluorescent imaging. An inverted fluorescent microscope equipped with the appropriate excitation/emission filter(s) and camera insertion site also should include a mercury or xenon lamp for fluorophore excitation and a digital camera. The computer selected should have sufficient memory to process and to analyze digital images using analysis software. All equipment shown should be set up in a room in which lighting can be shut off without inconveniencing other laboratory operations.

Quantum Dot Bio-conjugation

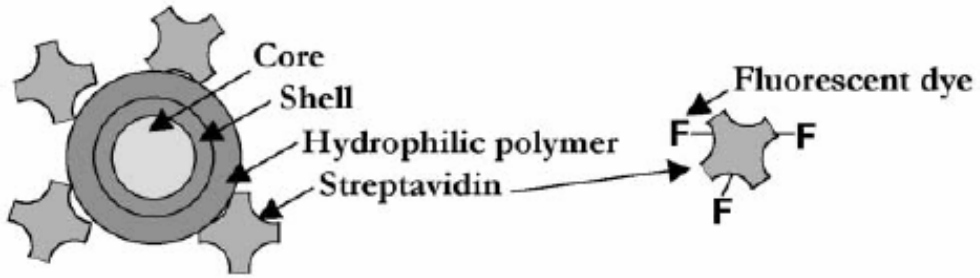

Fig. 3. Schematic of Qdot™ Nanocrystal Probe compared to a typically labeled fluorescent dye protein conjugate (see text for descriptions). Proteins generally carry several fluorescent dye labels (F). By contrast, each quantum dot is conjugated to multiple protein molecules.

Q-dot Aggregation

Clustering

Non-Clustering

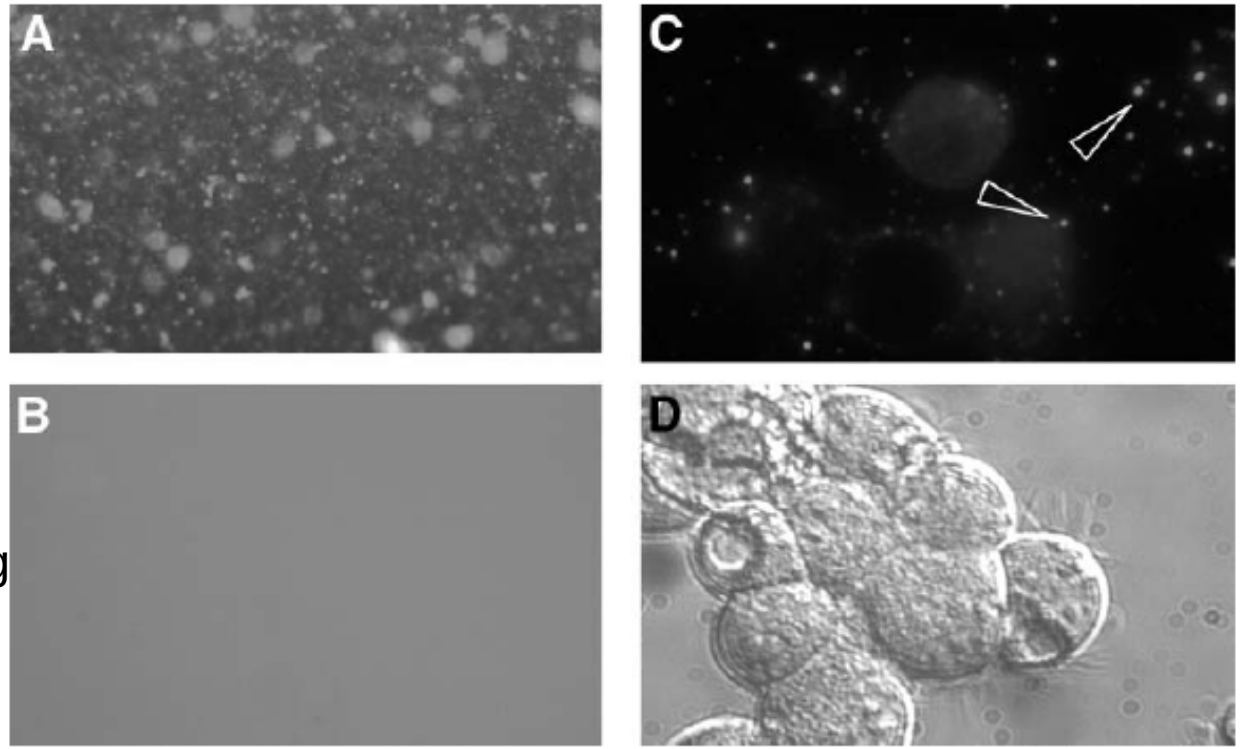

Clustering

Fig. 4. Evidence for quantum dot aggregation (magnification: ×40): **(A)** fluorescent image of aggregated SA-quantum dots in absence of cells; **(B)** image of nonaggregated SA-quantum dots in absence of cells; **(C)** image of cells surrounded by aggregated SA-quantum dots (arrowheads); **(D)** bright-field image.

Biotinylated Cell

Cell + Biotin

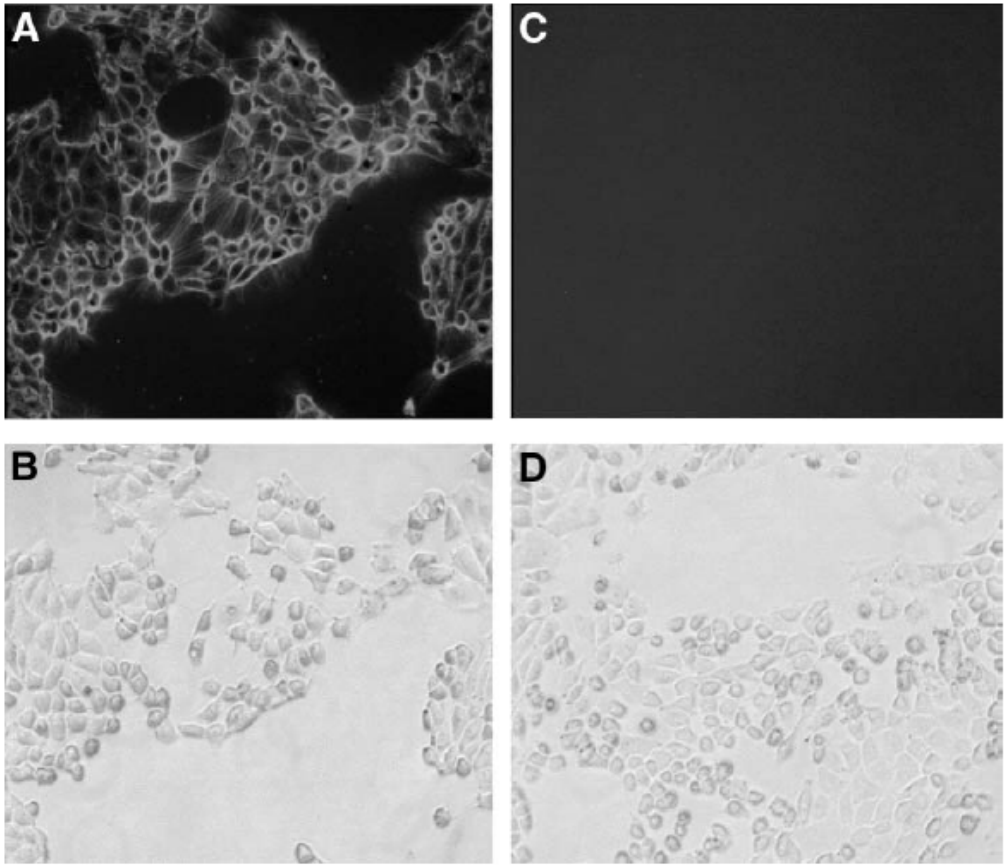

Fig. 1. Labeling of biotinylated HEK293 cells with SA-quantum dots (magnification: ×10). Three-day-old HEK293 cells cultured on poly-D-lysine glass-bottomed microwell dishes were biotinylated as described in **Subheading 3.2.1.** **(A,B)** Biotinylated HEK293 cells incubated with SA-quantum dots (50 n*M*); **(C,D)** biotinylated HEK293 cells labeled with SA-quantum dots after preincubating with 2 mg/mL of biotin.

Q-dot Antibody Labeling

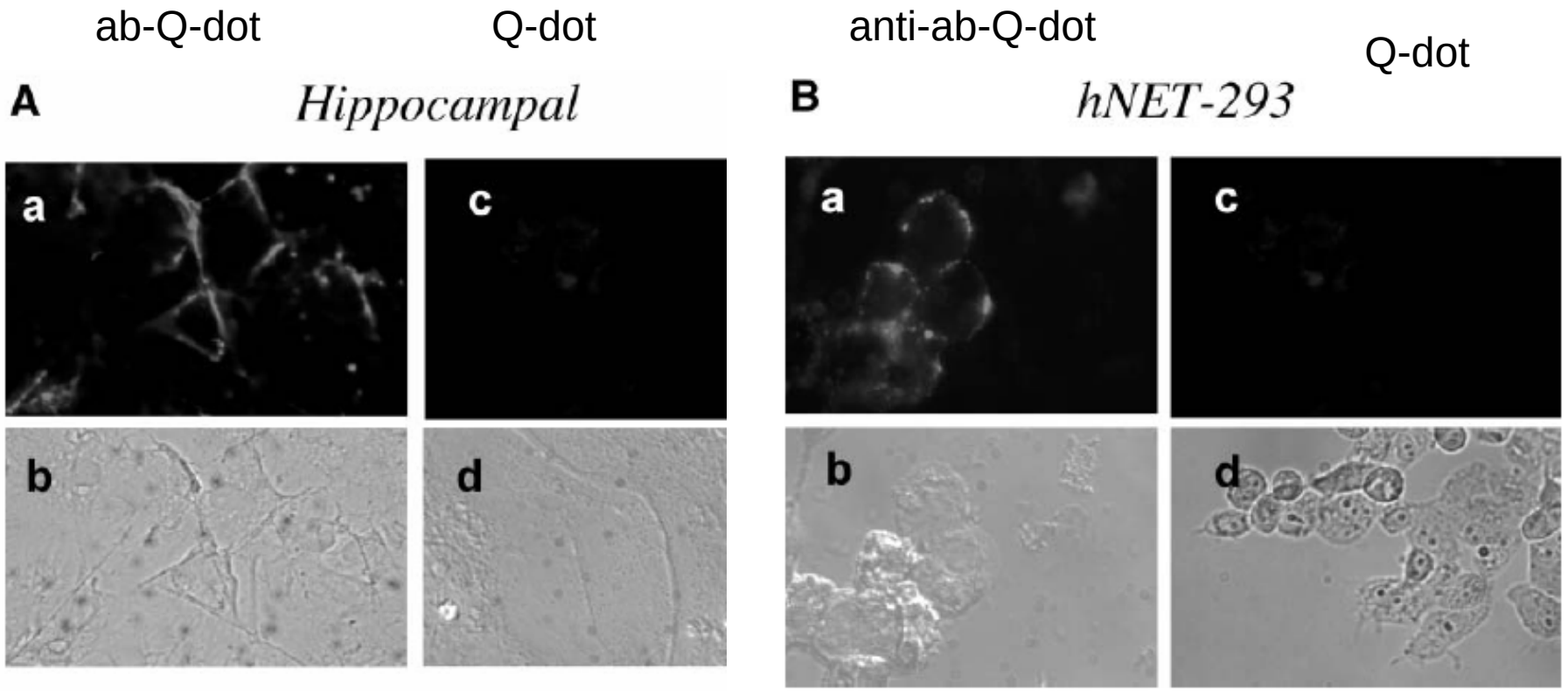

Fig. 5. SA-quantum dots and SA-Alexa Red recognize biotin-modified antibody-labeled cultures. **(A)** Eight-day-old *fixed* primary hippocampal cultures incubated with anti-LAMP followed by SA-quantum dots (a, b) or SA-quantum dots alone (c, d); **(B)** labeling of live hNET-293 cells with anti-hNET + biotinylated anti-rabbit IgG followed by SA-quantum dots (a, b) or SA-quantum dots alone (c, d).

Use of Nanobarcodes® Particles in Bioassays

R. Griffith Freeman, Paul A. Raju, Scott M. Norton,
Ian D. Walton, Patrick C. Smith, Lin He, Michael J. Natan,
Michael Y. Sha, and Sharron G. Penn

Submicrometer Metallic Barcodes

Sheila R. Nicewarner-Peña,[1] R. Griffith Freeman,[2]
Brian D. Reiss,[1] Lin He,[2] David J. Peña,[1] Ian D. Walton,[2]
Remy Cromer,[2] Christine D. Keating,[1]* Michael J. Natan[2]*

SCIENCE VOL 294 5 OCTOBER 2001

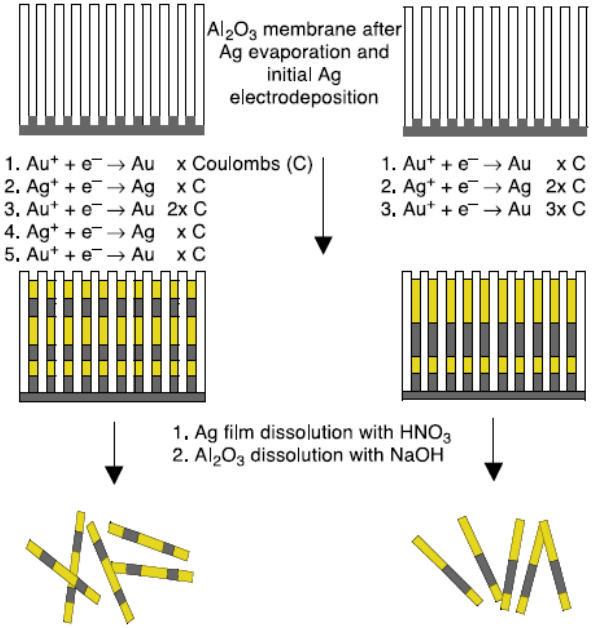

Fig. 1. Synthesis of barcoded particles.

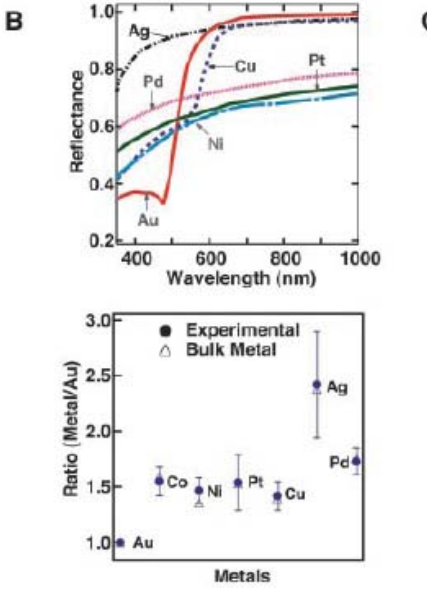

Surface Functionalization

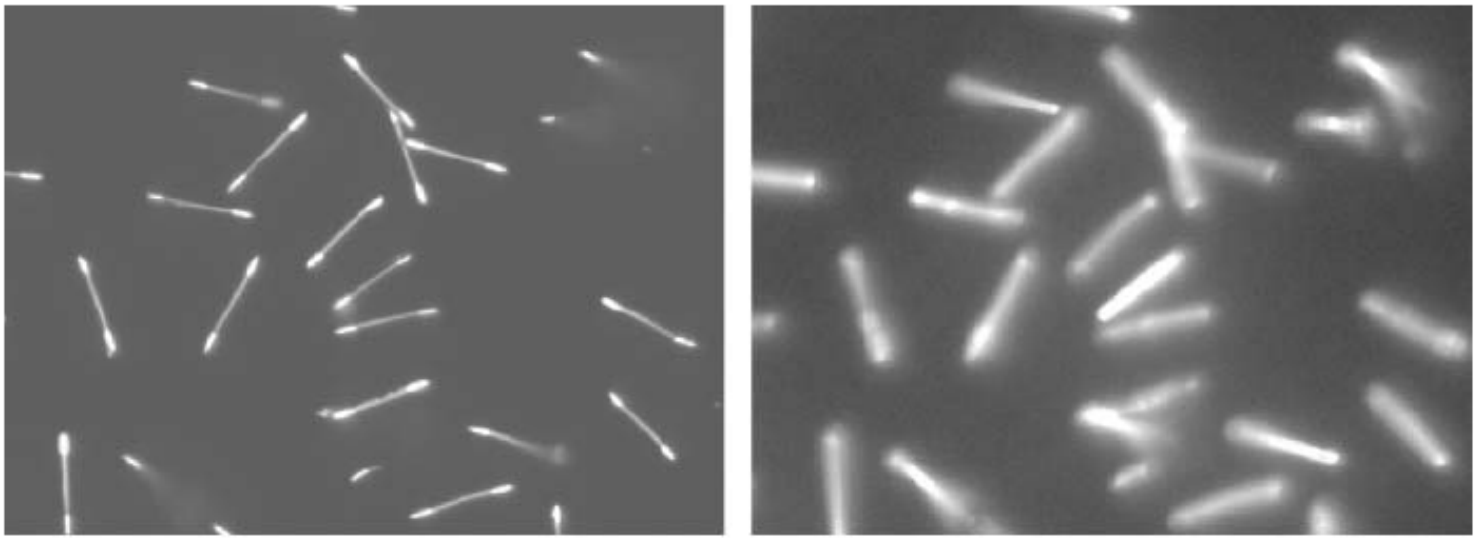

Reflectance **Fluorescence**

Fig. 2. Signal detection of oligonucleotide-derivatized NBCs hybridized with complementary Cy5 oligonucleotide.

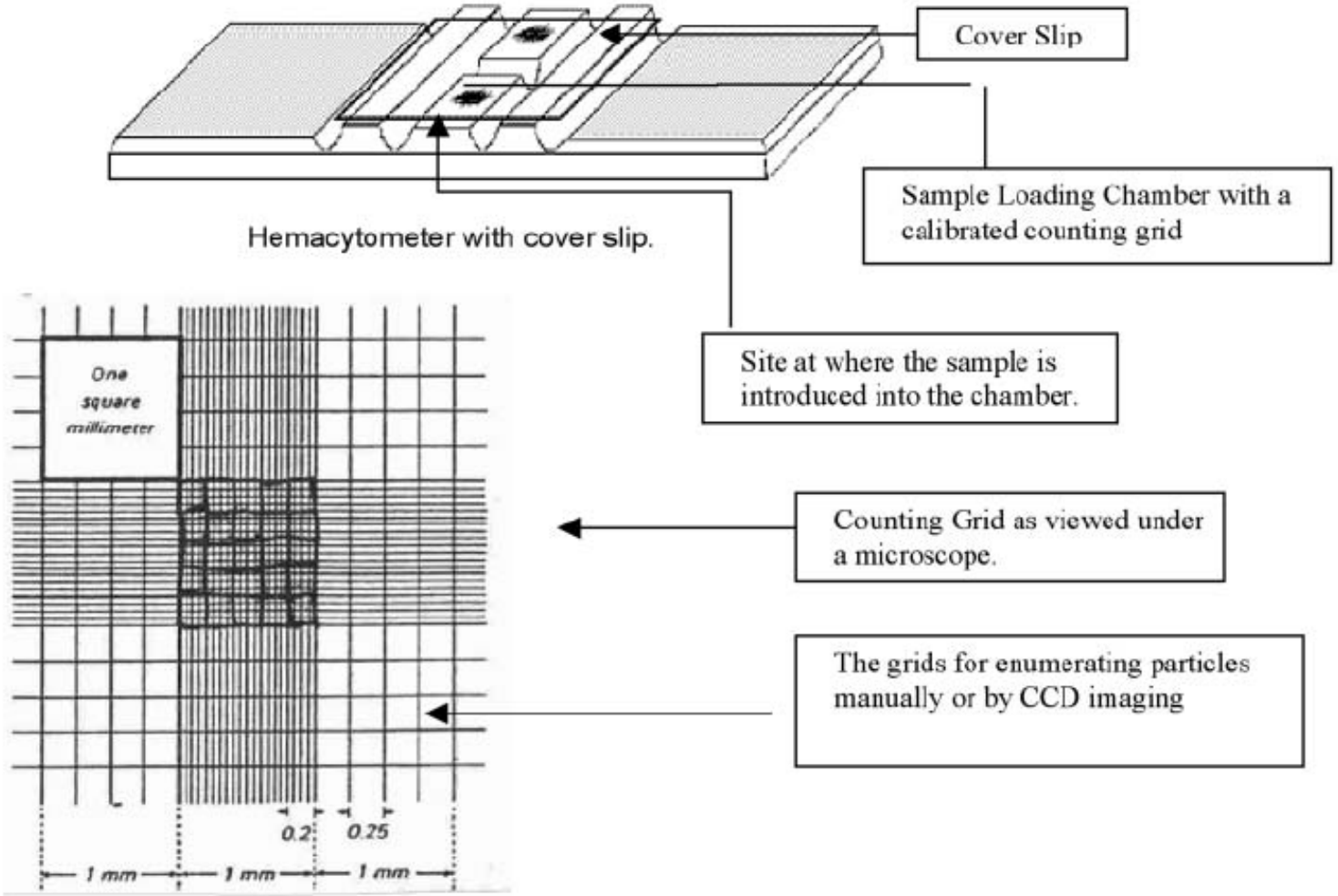

Fig. 3. Layout of hemacytometer.

Synthesis of Nanoparticles and Surface Modifications

Synthesis of Silver Nanoparticles

1. ***A solution of $AgNO_3$ (1.0×10^{-3} M) in deionized water was heated until it began to boil.***
2. ***Sodium citrate solution was added dropwise to the silver nitrate solution as soon as the boiling commenced. The color of the solution slowly turned into grayish yellow, indicating the reduction of the Ag+ ions.***
3. ***Heating was continued for an additional 15 min, and then the solution was cooled to room temperature before employing for further experimentation.***

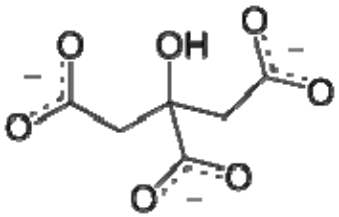

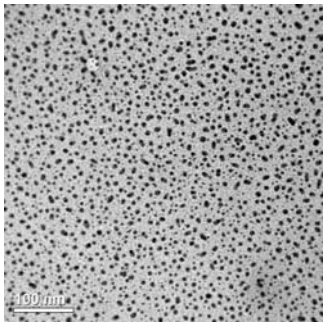

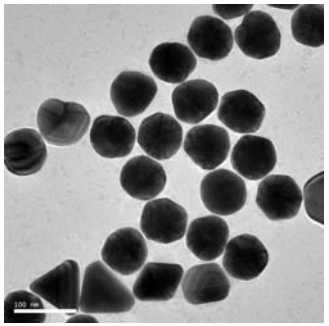

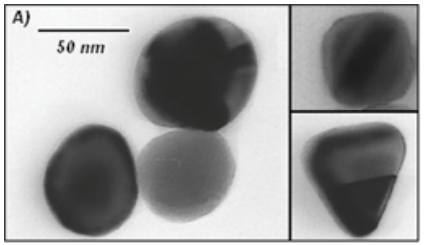

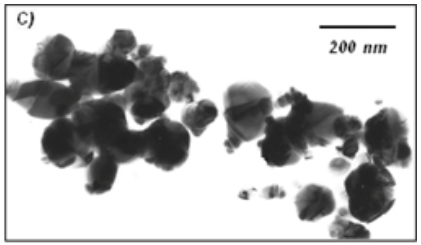

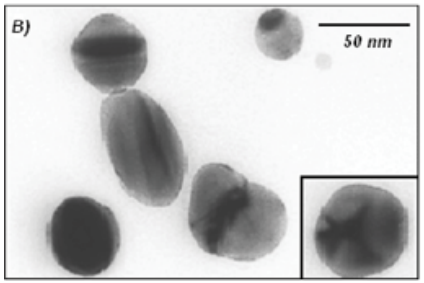

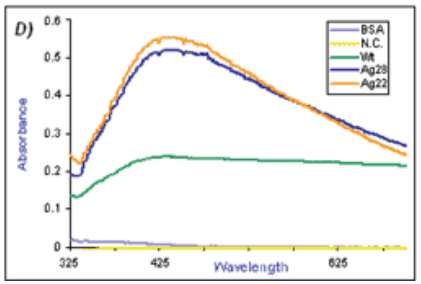

Synthesis of Gold Nanoparticles

1. ***Add 20 mL of 1.0 mM $HAuCl_4$ to a 50 mL round bottom flask on a stirring hot plate.***
2. ***Add a magnetic stir bar and bring the solution to a boil.***
3. ***To the boiling solution, add 2 mL of a 1% solution of trisodium citrate dihydrate***
4. ***The gold sol gradually forms as the citrate reduces the gold(III). Stop heating when a deep red color is obtained.***

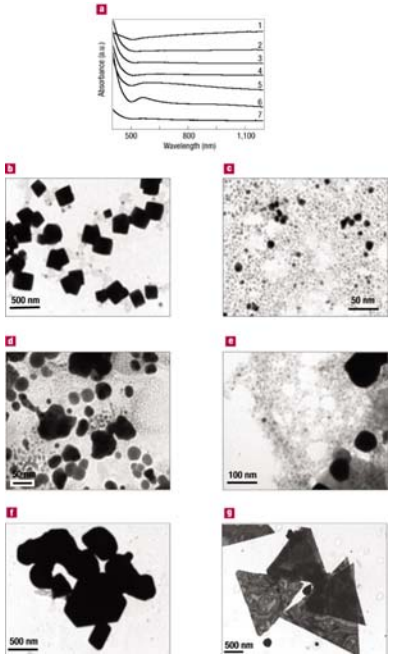

(1) $$M_xO_y \xrightarrow[(\text{medium})\ \Delta_T]{\text{Reducing Agent}} M_n + H_2O$$

(Reducing Agent = R - COH)

(2) $$M(L)_x \xrightarrow[(\text{medium})\ \Delta_T]{\text{Reducing Agent}} M_n + L^-$$

($L=NO_3^-, C_2H_5O^-$)

(Reducing Agent = R - COH)

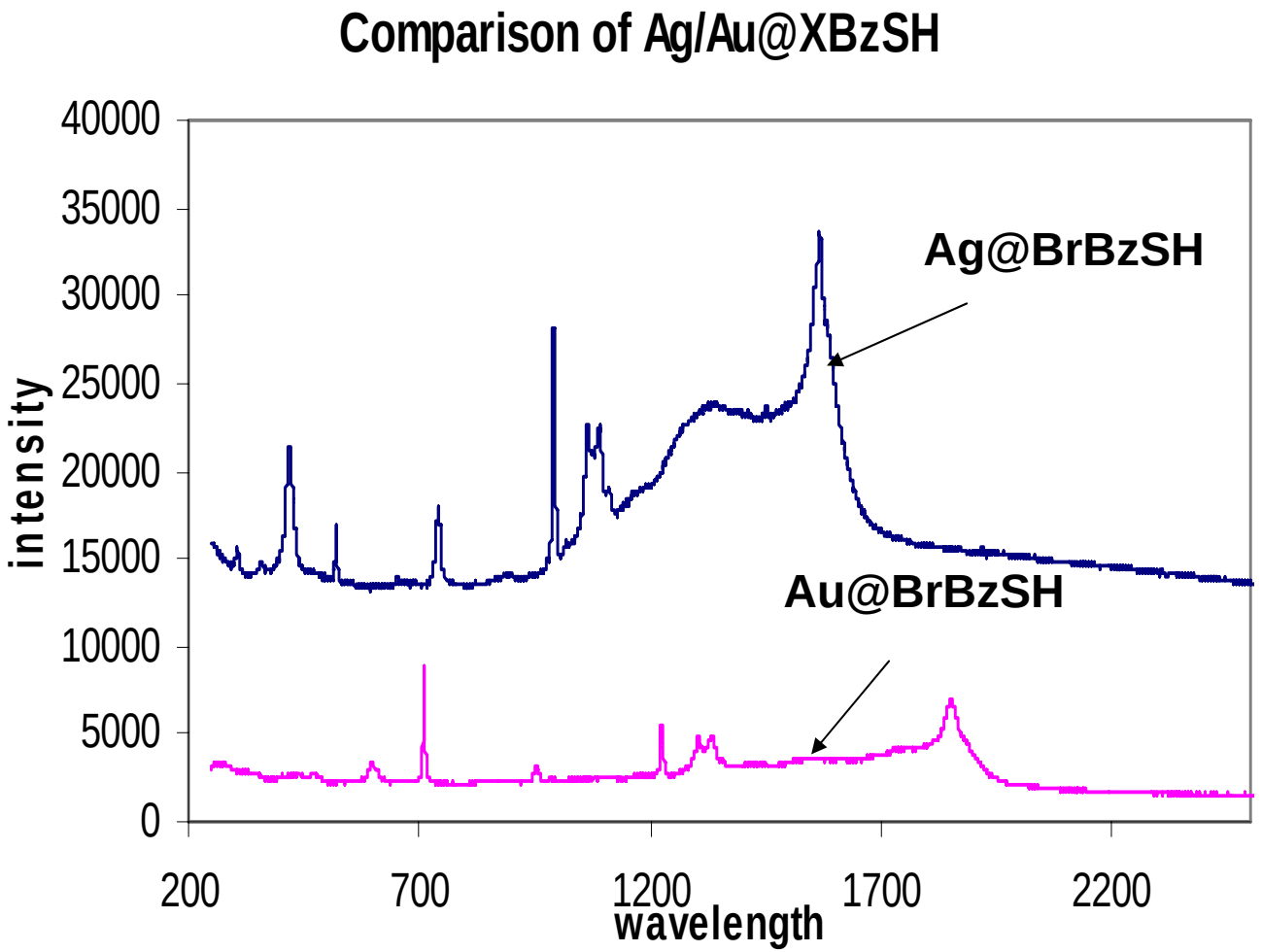
Comparison of Ag/Au@XBzSH
40000
35000
30000
25000
20000
15000
10000
5000
0
intensity
200
700
1200
1700
2200
wavelength
Ag@BrBzSH
Au@BrBzSH

Construction of Core Shell Ag/Au@SiO_2 Nanoparticles

1. *Under vigorous stirring, 1 ml of the silver/ gold colloids solution was mixed with 250 mL of isopropanol and 25 mL of deionized water.*
2. *Immediately after the addition of 4 mL of 30% ammonium hydroxide, different amounts of tetraethoxysilane (TEOS) were added to the reaction mixture.*
3. *To obtain different silica layer thicknesses, TEOS solutions with a concentration between 50% and 100% was added to the suspension. The reaction was stirred at room temperature for 30 minutes and then was allowed to age without agitation at 4 ℃ overnight.*
4. *Each suspension of silica-coated silver/gold nanoparticles was washed and centrifuged, followed by re-suspension in water. The thickness of the silica layers was determined from TEM images .*

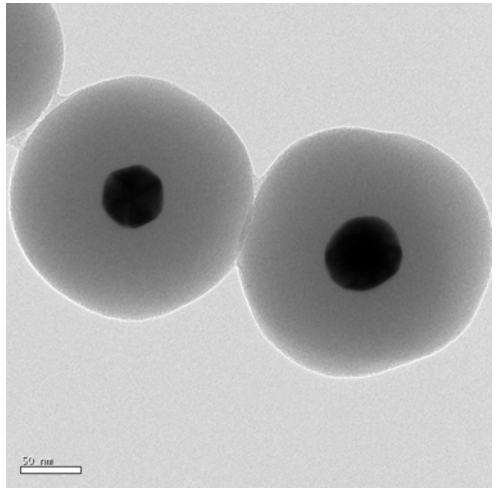

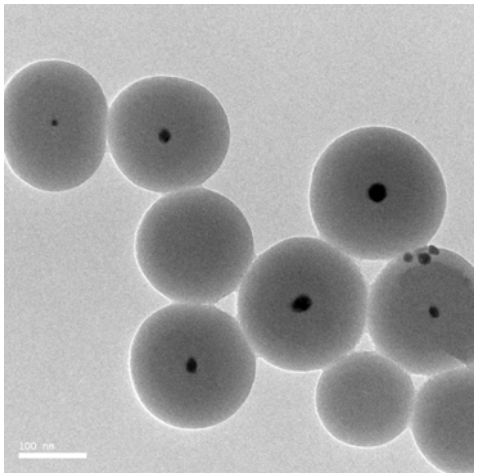

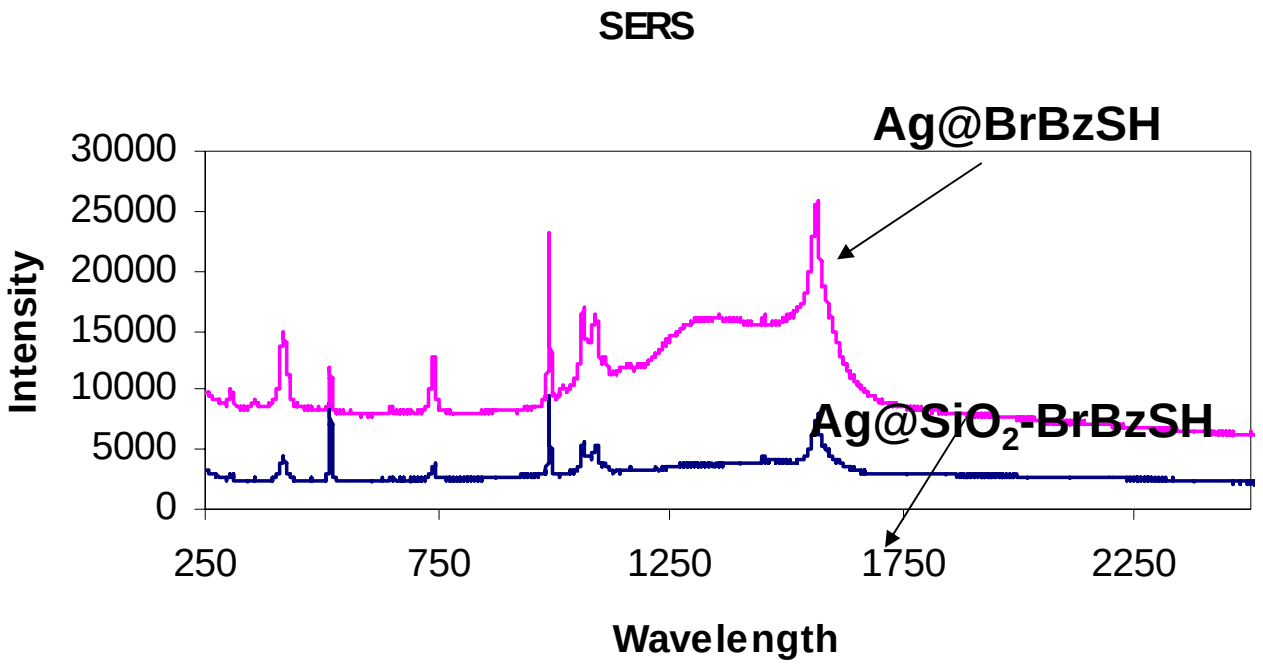
SERS
Ag@BrBzSH
Ag@SiO2-BrBzSH
Intensity
30000
25000
20000
15000
10000
5000
0
250
750
1250
1750
2250
Wavelength

Core-Shell Nanoparticles

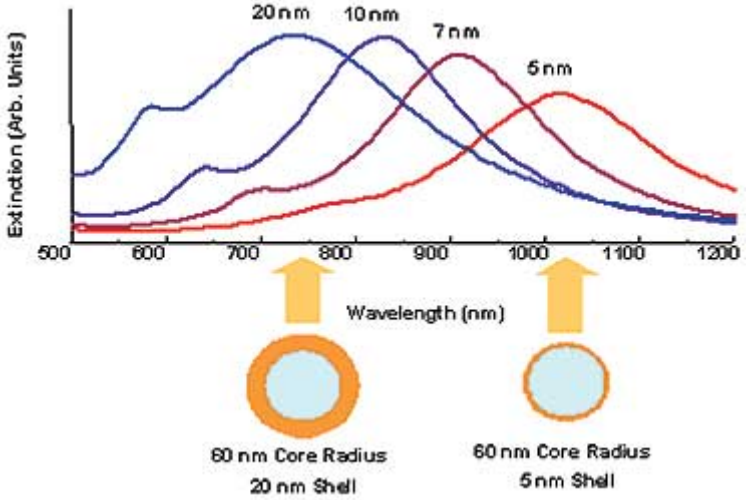

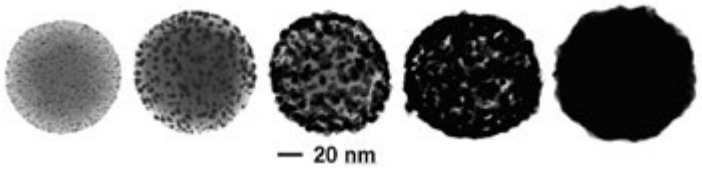

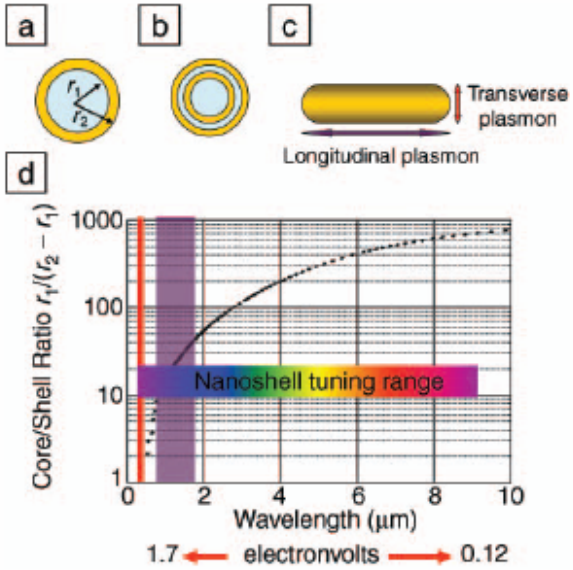

Figure 1. (a) Schematic illustration of a silica-core, gold-shell nanoshell, indicating inner (r_1) and outer (r_2) radii of the shell layers. (b) Depiction of a four-layer, concentric nanoshell. (c) Schematic illustration of a metallic nanorod. (d) Plot of nanoshell resonance as a function of core and shell dimensions, overlaid with reported spectral ranges of nanorod resonances (red, transverse plasmon; purple, longitudinal plasmon), and reported nanoshell and concentric nanoshell combined spectral range of plasmon response.

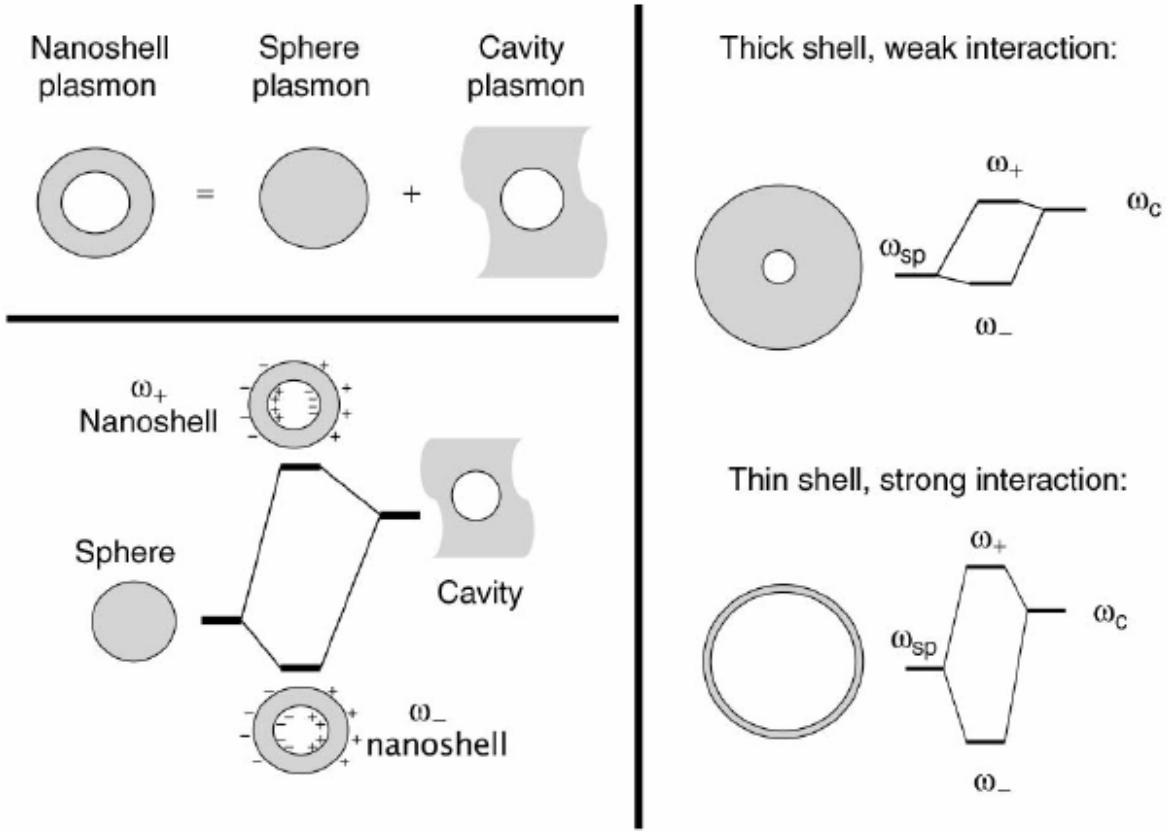

Figure 2. Plasmon hybridization and the sphere–cavity model for nanoshells: the interaction between a sphere (resonance frequency, ω_{sp}) and a cavity plasmon (resonance frequency, ω_c) is tuned by varying the thickness of the shell layer of the nanoparticle. Two hybrid plasmon resonances, the ω_- "bright," or "bonding," plasmon and the ω_+ "dark," or "anti-bonding," plasmon resonances are formed. The lower-energy plasmon couples most strongly to the optical field.

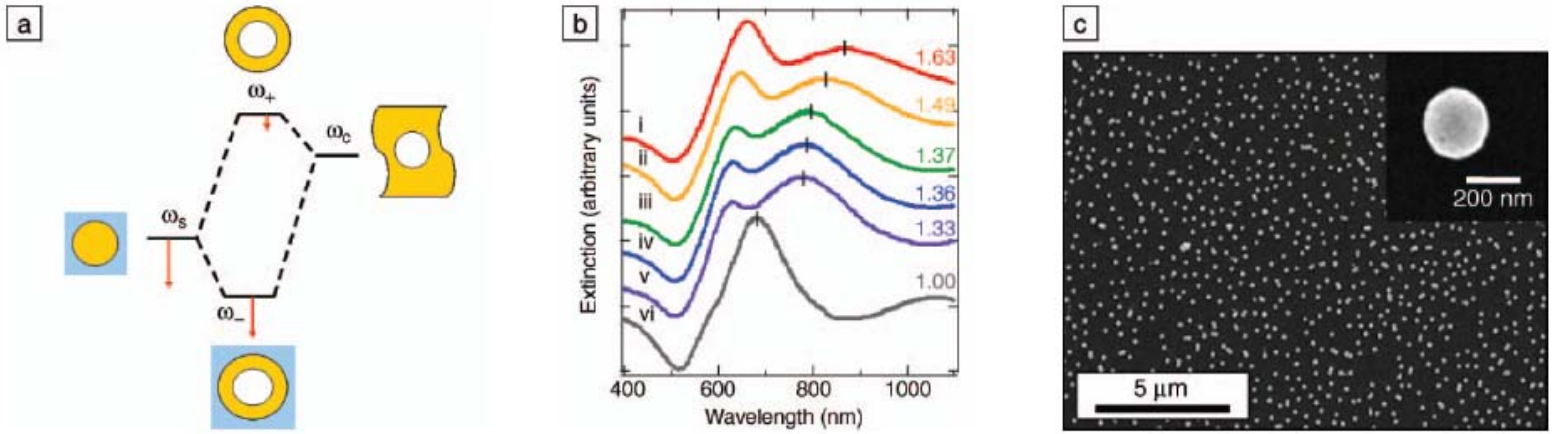

Figure 5. (a) Plasmon hybridization picture applied to surface plasmon resonance sensing with nanoshells: the low-energy "bonding" plasmon, ω_-, is sensitized to changes in its dielectric environment. The blue background schematically denotes the embedding medium for the nanoparticle. (b) Experimental curves showing plasmon resonance shifts for nanoshell-coated films in various media: (i) carbon disulfide, (ii) toluene, (iii) hexane, (iv) ethanol, (v) H_2O, and (vi) air. The index of refraction for each embedding medium is noted on the far right of the spectra. Spectra are offset for clarity. (c) Scanning electron micrograph of nanoshells deposited onto a poly(vinyl pyridine) functionalized glass surface, as used to acquire data in (b). Inset: individual nanoshell.

Preparation of Fe_3O_4@Ag/Au

1. *To the magnetic nanoparticle suspension obtained from commercial company, add 50 ml of a solution of Au (III) salt or Ag (I) salt at concentration of 0.01–1% mmol/L , shaking for 30 minutes, allowing Au (III) or Ag (I) ion to absorb on the surface of magnetic nanoparticle sufficiently,*
2. *Then adding 15–40 ml of reducing agent, such as hydroxylamine hydrochloride at concentration of 40 mmol/L, reacting for 5–40 minutes.*
3. *Further adding 1–10 ml of a solution of Au (III) salt or Ag (I) salt at concentration of 0.01–1%, shaking for 10 minutes, coating a reduced layer of gold or silver on the surface of the magnetic nanoparticle, forming super-paramagnetic composite particles having core/shell structure, separating magnetically, washing repeatedly with distilled water.*

.

Nanorods

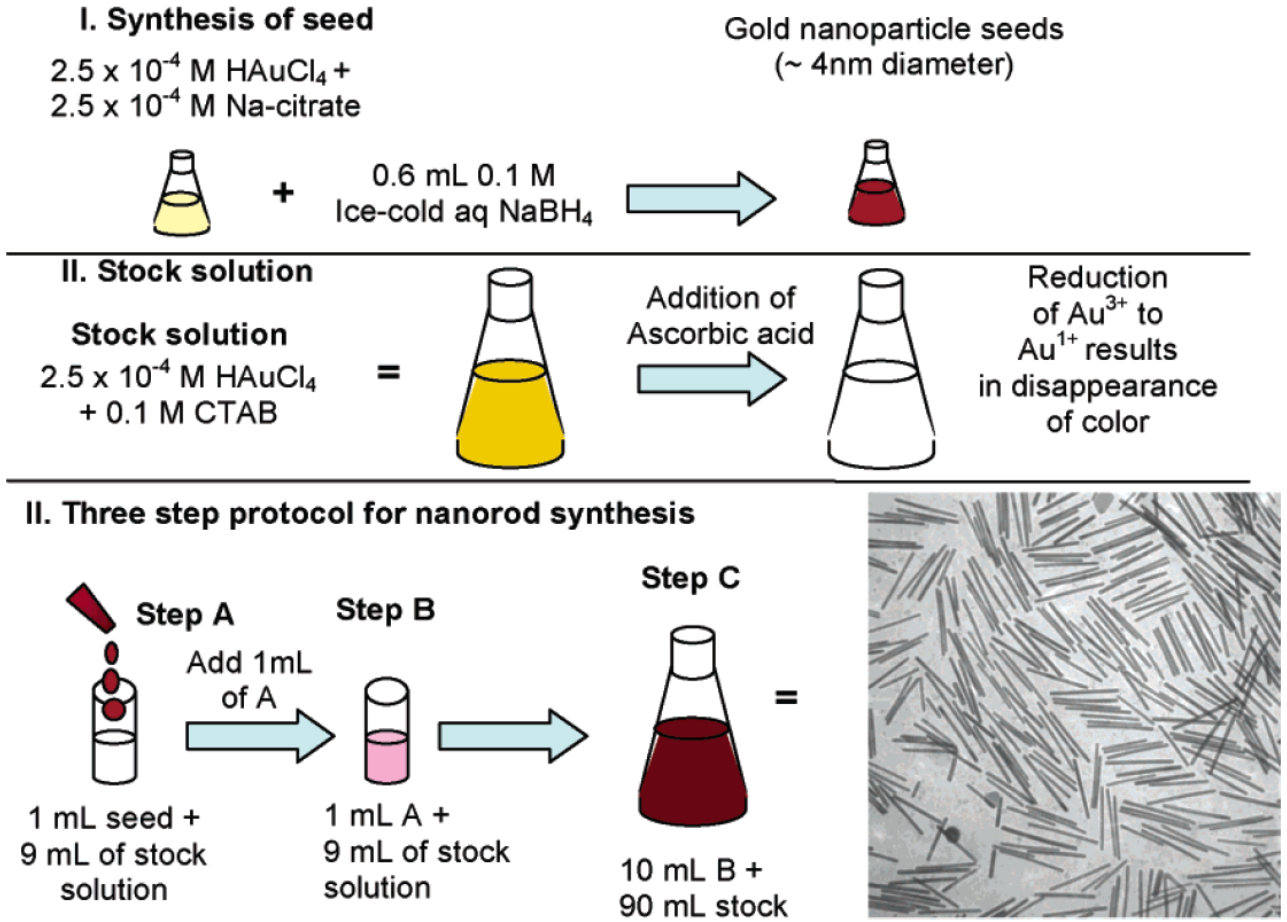

Figure 2. Seed-mediated growth approach to making gold and silver nanorods of controlled aspect ratio. The specific conditions shown here, for 20 mL volume of seed solution, lead to high-aspect ratio gold nanorods. (bottom right) Transmission electron micrograph of gold nanorods that are an average of 500 nm long.

J. Phys. Chem. B **2005,** *109,* 13857−13870

Directional Growth

Cetrimonium bromide ($(C_{16}H_{33})N(CH_3)_3Br$) (CTAB)

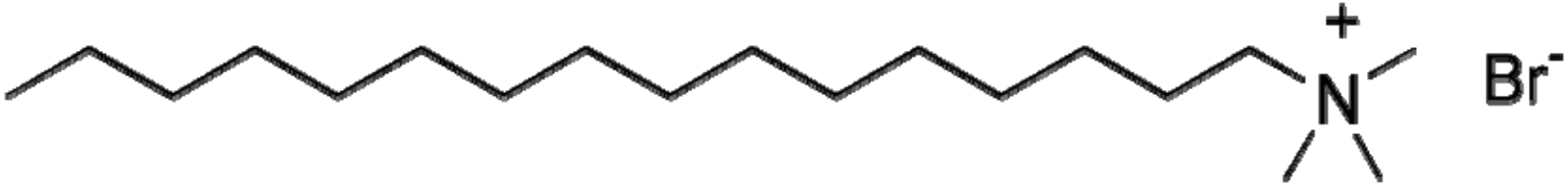

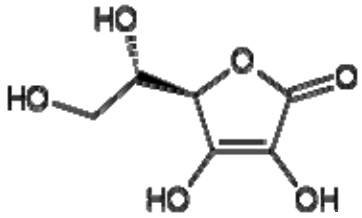

Ascorbic acid

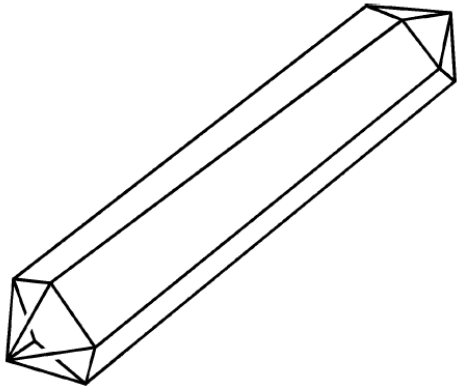

Figure 5. Cartoon of the crystallography of gold nanorods. The direction of elongation is [110]. The cross-sectional view is a pentagon; each end of the rod is capped with five triangular faces that are Au{111}. The sides of the rods are not as well-defined; either Au{100} or Au{110} faces, or both.

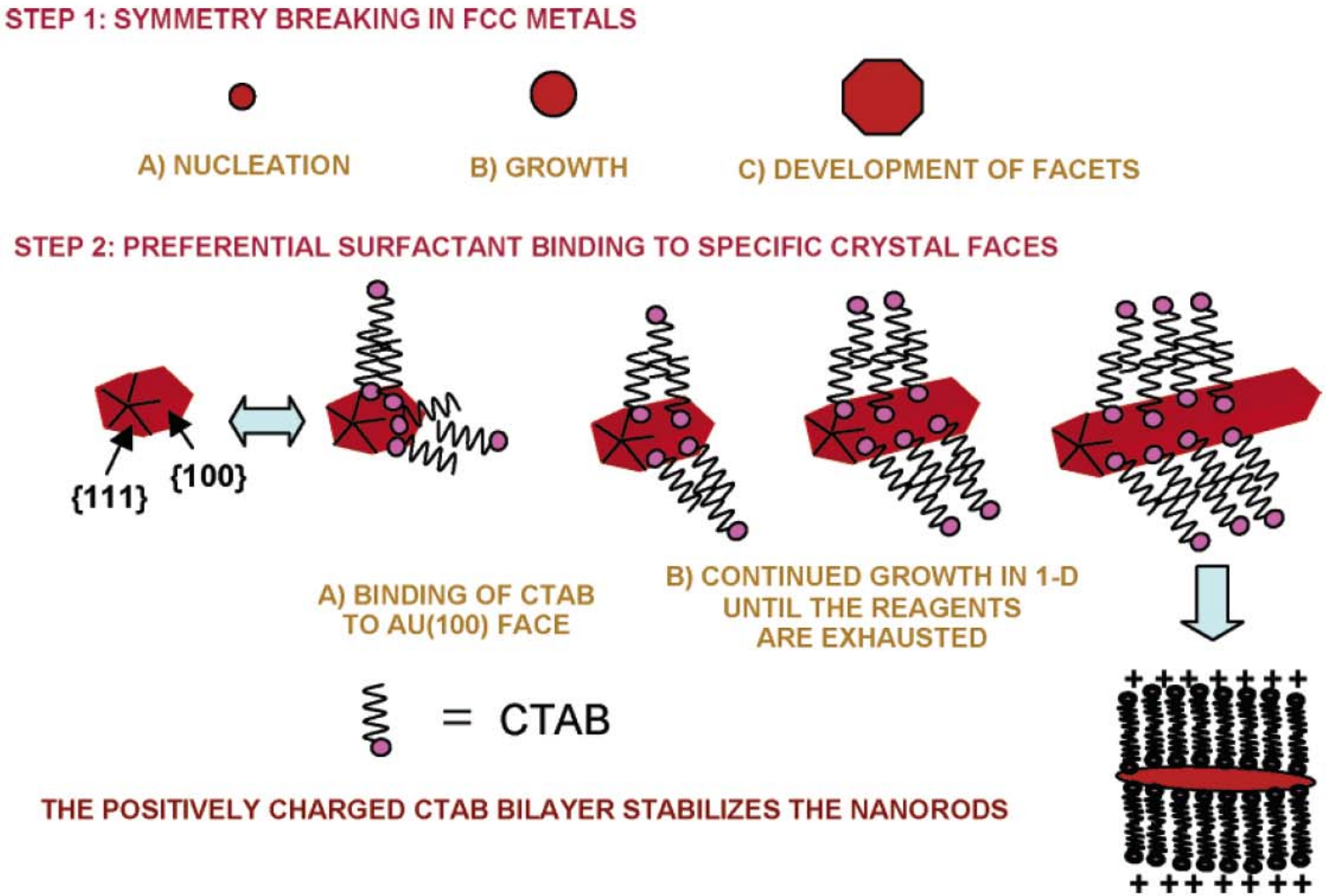

Figure 8. Proposed mechanism of surfactant-directed metal nanorod growth. The single crystalline seed particles have facets that are differentially blocked by surfactant (or an initial halide layer that then electrostatically attracts the cationic surfactant). Subsequent addition of metal ions and weak reducing agent lead to metallic growth at the exposed particle faces. In this example, the pentatetrahedral twin formation leads to Au {111} faces that are on the ends of the nanorods, leaving less stable faces of gold as the side faces, which are bound by the surfactant bilayer.

Nanorods

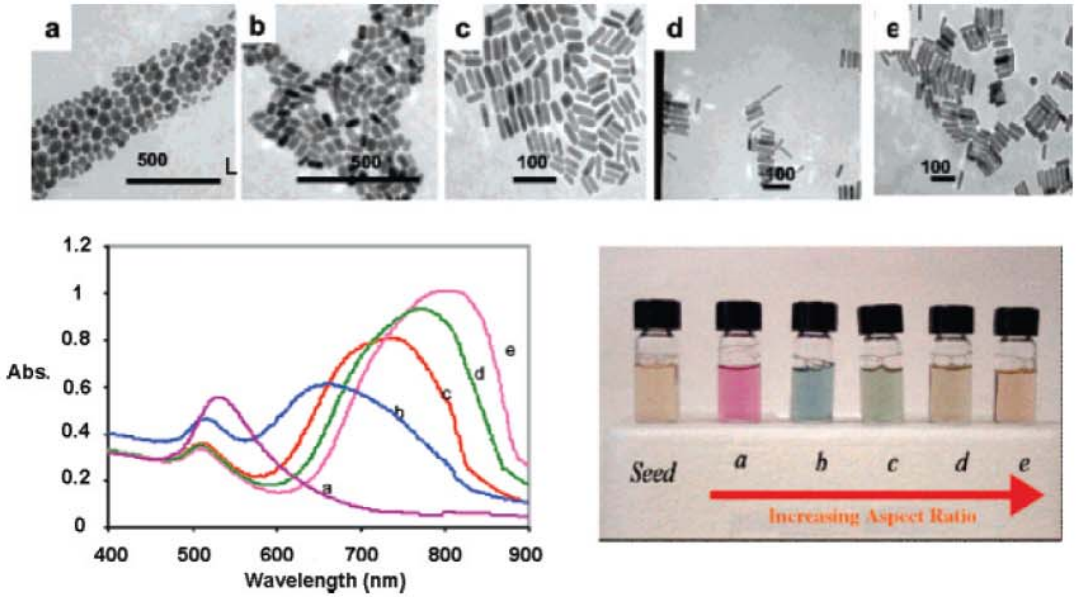

Figure 3. Transmission electron micrographs (top), optical spectra (left), and photographs (right) of aqueous solutions of Au nanorods of various aspect ratios. The seed sample has an aspect ratio of 1. Samples a, b, c, d, and e have aspect ratios of 1.35 ± 0.32, 1.95 ± 0.34, 3.06 ± 0.28, 3.50 ± 0.29, and 4.42 ± 0.23, respectively. Scale bars: 500 nm for a and b, 100 nm for c−e. Reprinted with permission from ref 16. Copyright 2005 American Chemical Society.

Nanocube and Nanorice

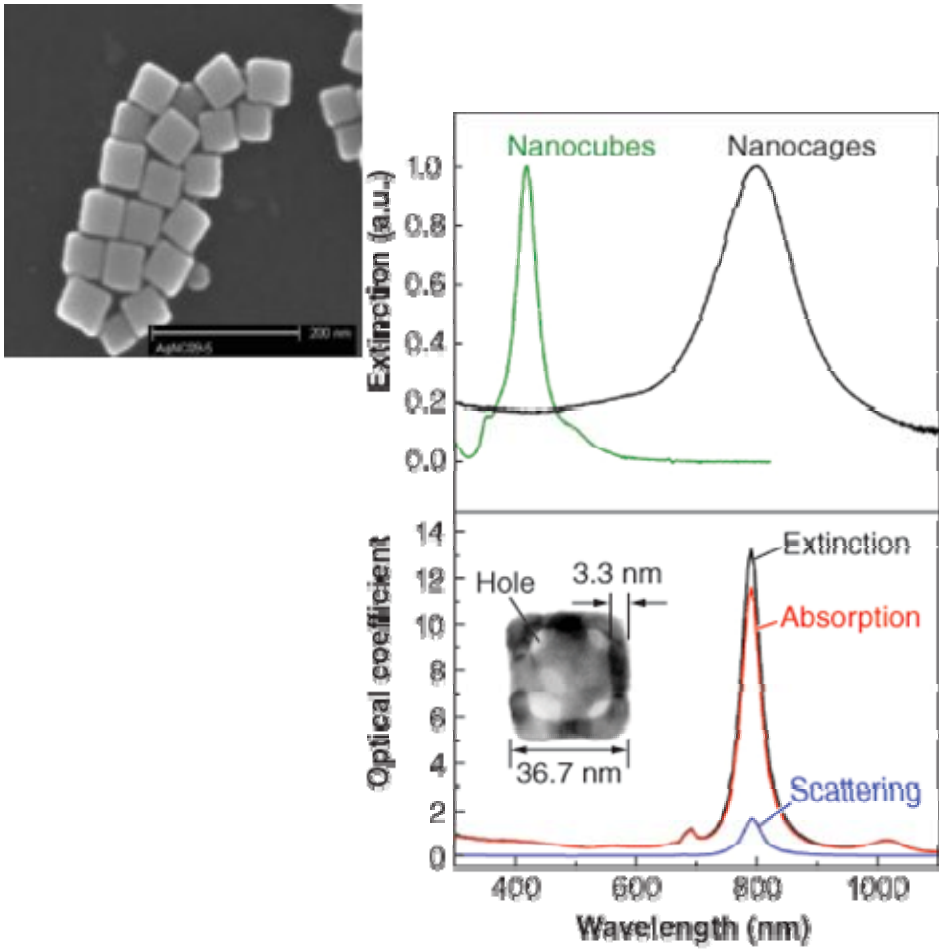

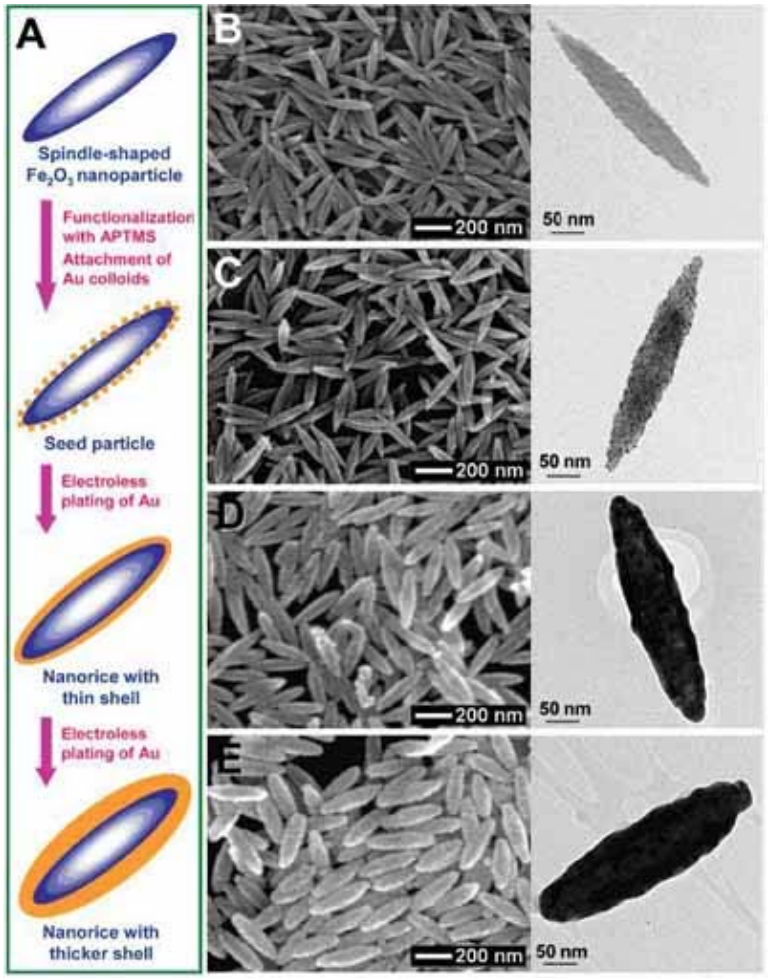

The graphic above depicts various magnitudes of nanorice, which is a rice-shaped nanoparticle with a non-conducting core made of iron oxide and covered by a metallic shell made of gold. Scientists plan to attach the nanorice to scanning probe microscopes to obtain very clear image quality that surpasses today's technology. For the Air Force, this technology could be used as a tool to develop new high-speed optoelectronic materials and to monitor chemical reactions. (Graphic provided by Prof. Naomi Halas)

Synthesis of CdSe Quantum Dots

Synthesis of TOPO/HDA capped quantum dots of CdSe

Cadmium acetate (0.107g, 0.4mmol) and oleic acid (0.27mL, 0.4mmol) in 1:2 ratio were placed in a two neck flask degassed and refilled with nitrogen, stirred at 120-130 ^{0}C under nitrogen atmosphere for 2-3 hours, obtained a clear light yellow solution. Then a mixture of capping reagent i.e. 6g of hexadecylamine (HDA) and 6g of tri-octylphosphine oxide (TOPO) prepared in separate flask was added at the same temperature and stirring was done for another 30min at temperature ~ 350 ^{0}C. The temperature was reduced and TOPSe was added at different temperatures at 250 ^{0}C through syringe immediately the color of reaction mixture became dark brown (TOPSe was prepared simultaneously in a separate vessel, appropriate quantity of Se (0.032g) powder was heated in 2mL tri-octyl phosphine (TOP) at 70-90 ^{0}C for about an hour to get a clear solution of TOPSe), stirring was continued for another 30min aliquots were taken from the reaction solution to monitor the reaction. The temperature of the reaction was reduced the stirring was done for another 1-2 hours. 50mL toluene was added before the cooling the reaction to prevent the solidification of TOPO and HDA. It was centrifuged at 3000rpm for 15min, a pallet was discarded, the supernatant solution was treated with the methanol for precipitation of CdSe nano-crystals, centrifuged at 7000rpm washed with methanol (3 x 6mL) to get product. A red residue was obtained which was re-dispersed in toluene.

Synthesis of CdSe Quantum dots

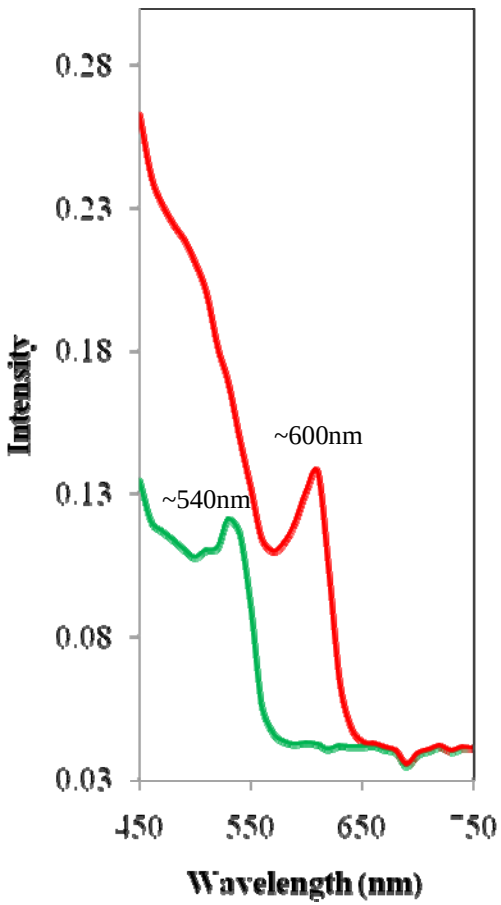

FWHM= ~28nm ± 2

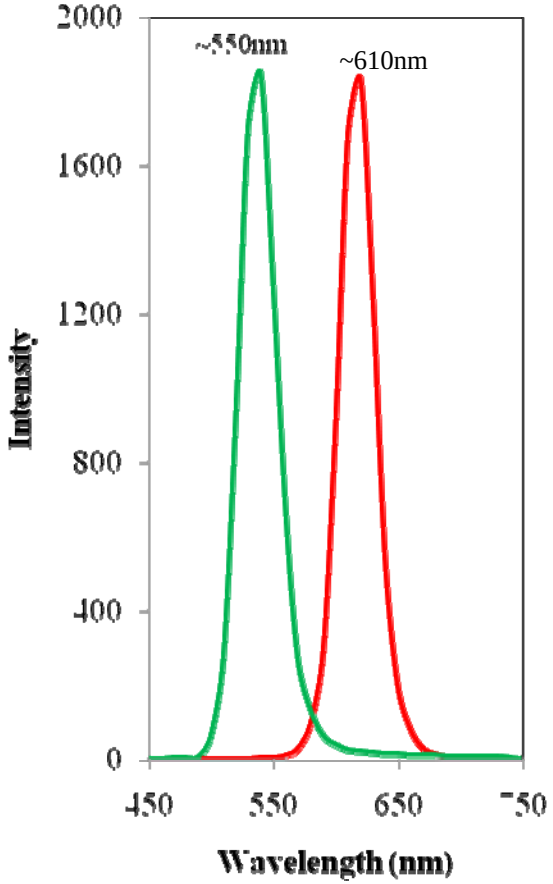

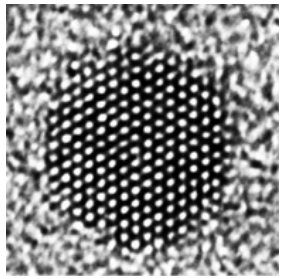

Cooperative UV and PL spectra of CdSe core

Synthesis of CdSe/ZnS Quantum Dots

20mL (31mg, 0.16 mmol) colloidal solution of CdSe QDs from stock solution (54mg dissolved in 35mL toluene) was placed in a two-neck flask. TOPO (6g) and HAD (6g) were added and then toluene was removed through vacuum, flask refilled with nitrogen. The reaction mixture was heated at 350 ^{0}C for two hours. In another flask zinc acetate in 1:3 ratio with respect of CdSe and was dissolved in 4mL of oleic acid stirred at 120 ^{0}C for 2 hours obtained a light yellow coloured solution and temperature reduced to 60-70 ^{0}C. After cooling to room temperature, TOPSe was mixed with Zn salt solution. And the mixture was injected slowly through syringe in to reaction solution of CdSe-TOPO at 180-200 ^{0}C. The stirring was done for another an hour. The similar procedure was followed for work up of reaction as avobe experiment. The final product was re-dispersed in toluene.

Light emission from CdSe/ZnSe Quantum dots

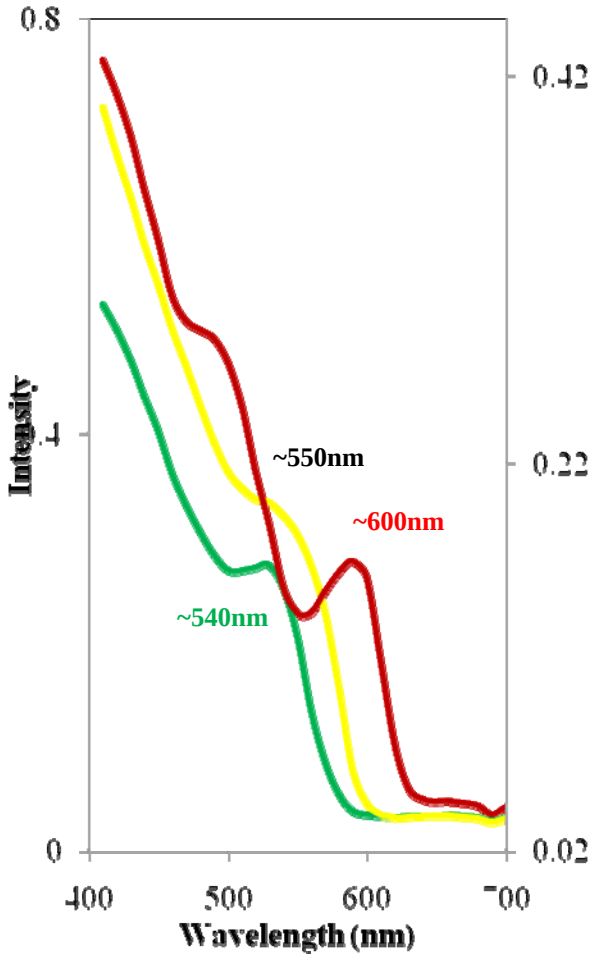

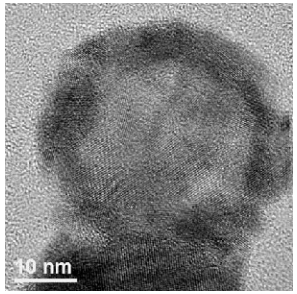

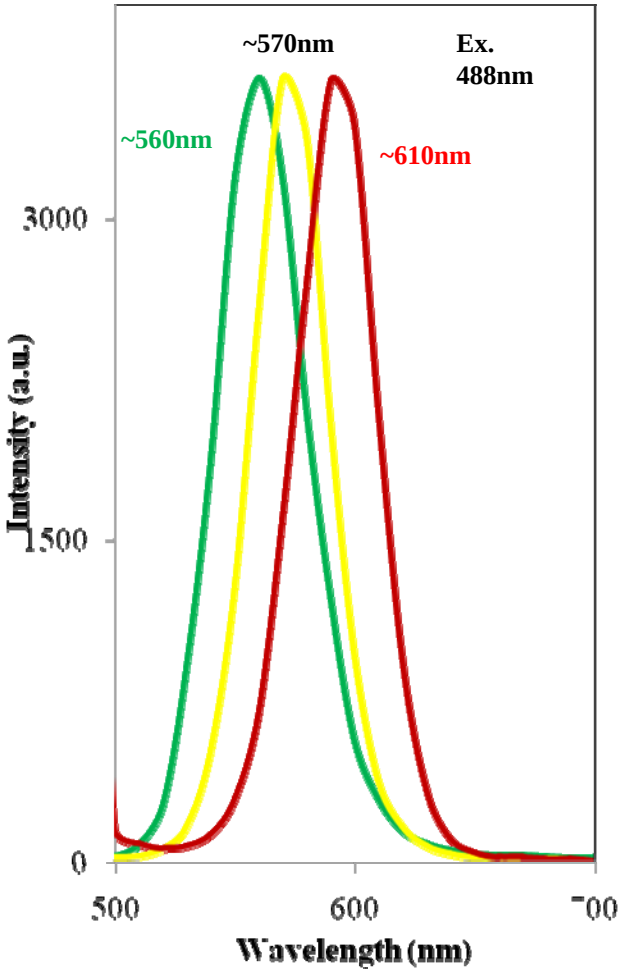

UV-Visible and PL spectra of CdSe/ZnSe re-dispersed in toluene

Carboxyl Presenting Surfaces

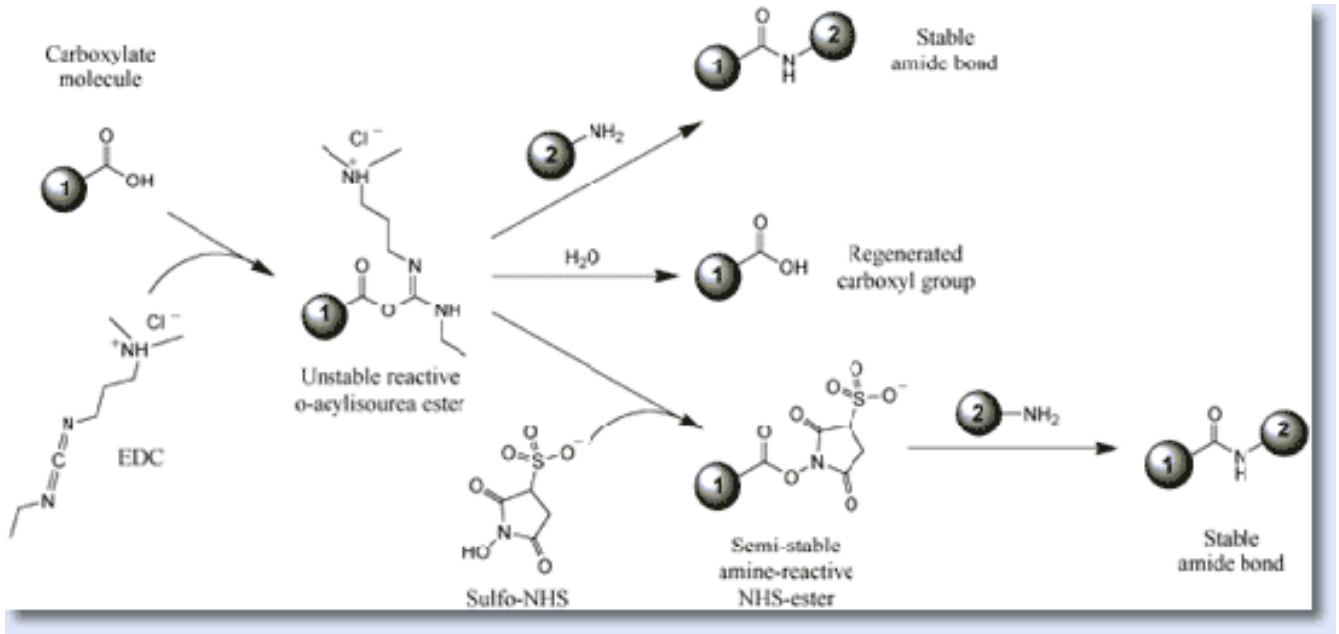

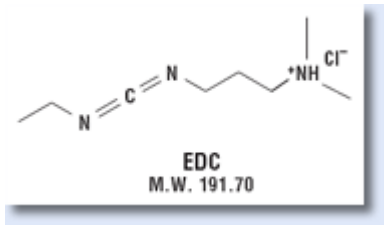

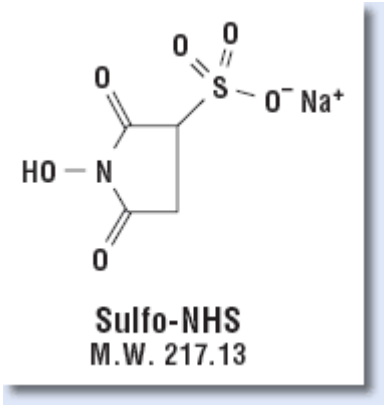

EDC (1-Ethyl-3-[3-dimethylaminopropyl]carbodiimide Hydrochloride)

Amine Presenting Surface

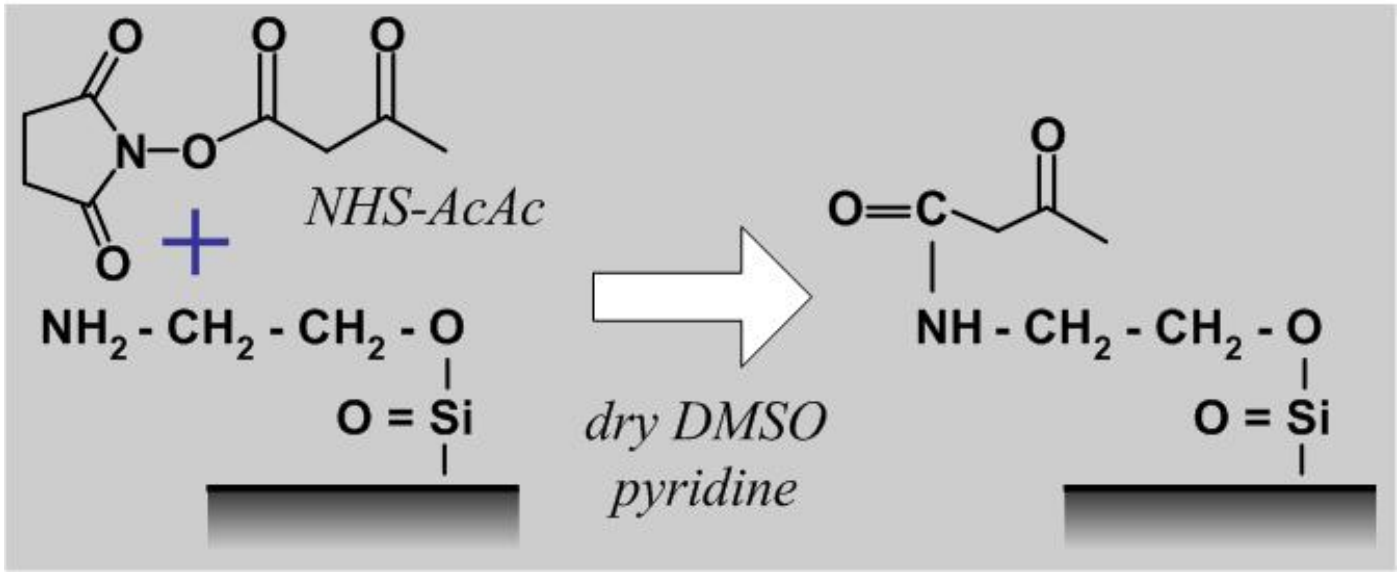

Sulfhydryl Labeling

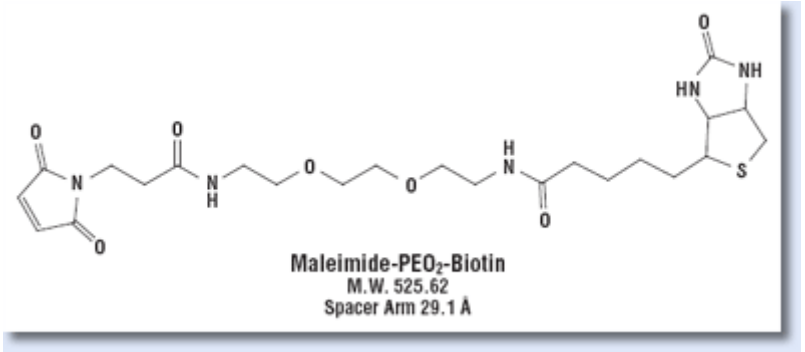

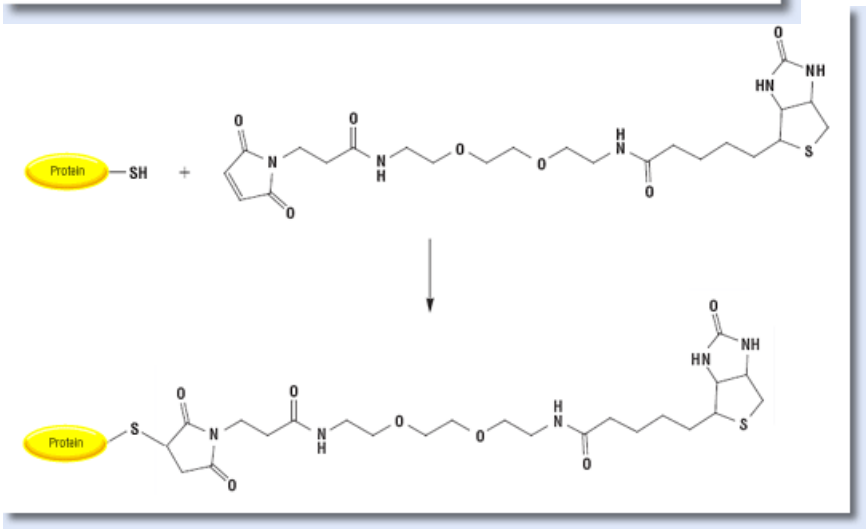

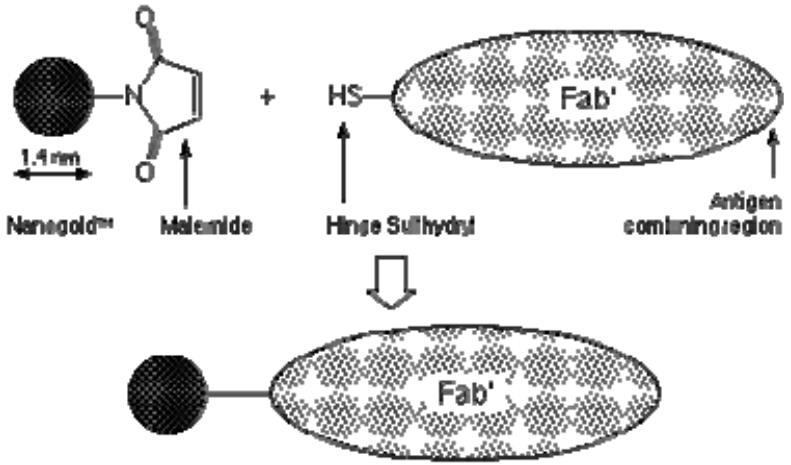

Silica Modification

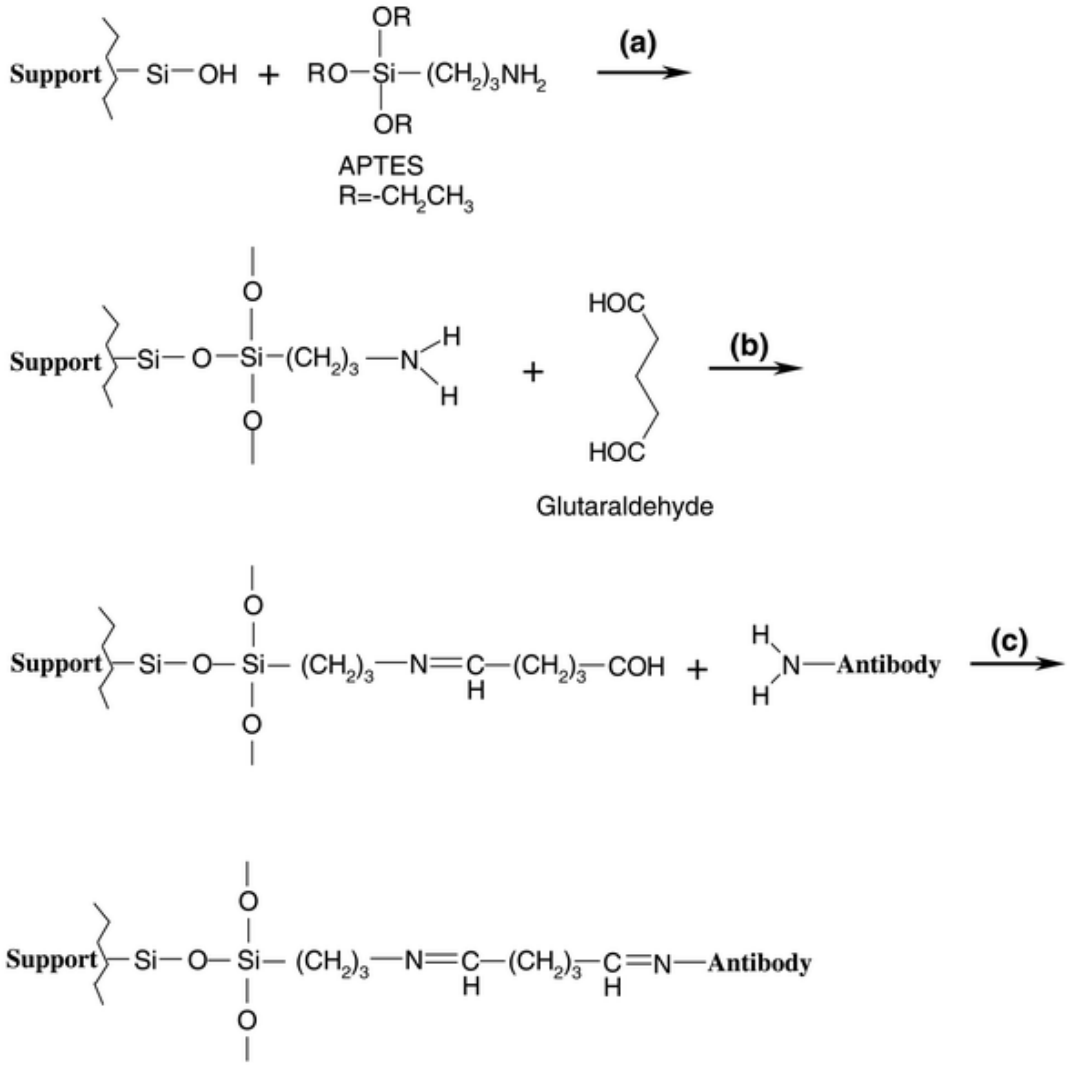

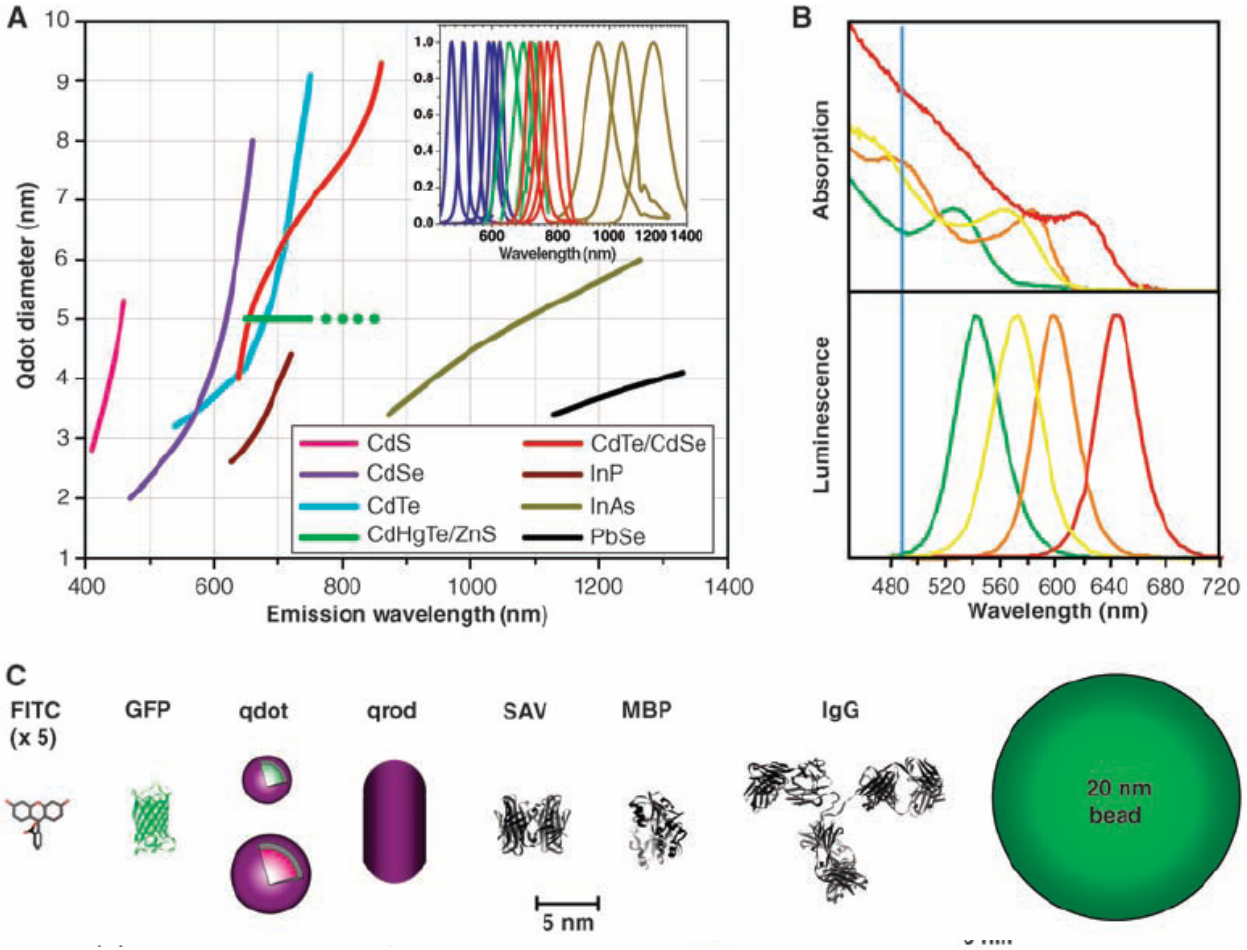

Fig. 1. (**A**) Emission maxima and sizes of quantum dots of different composition. Quantum dots can be synthesized from various types of semiconductor materials (II-VI: CdS, CdSe, CdTe…; III-V: InP, InAs…; IV-VI: PbSe…) characterized by different bulk band gap energies. The curves represent experimental data from the literature on the dependence of peak emission wavelength on qdot diameter. The range of emission wavelength is 400 to 1350 nm, with size varying from 2 to 9.5 nm (organic passivation/solubilization layer not included). All spectra are typically around 30 to 50 nm (full width at half maximum). Inset: Representative emission spectra for some materials. Data are from (*12*, *18*, *27*, *76*–*82*). Data for CdHgTe/ZnS have been extrapolated to the maximum emission wavelength obtained in our group. (**B**) Absorption (upper curves) and emission (lower curves) spectra of four CdSe/ZnS qdot samples. The blue vertical line indicates the 488-nm line of an argon-ion laser, which can be used to efficiently excite all four types of qdots simultaneously. [Adapted from (*28*)] (**C**) Size comparison of qdots and comparable objects. FITC, fluorescein isothiocyanate; GFP, green fluorescent protein; qdot, green (4 nm, top) and red (6.5 nm, bottom) CdSe/ZnS qdot; qrod, rod-shaped qdot (size from Quantum Dot Corp.'s Web site). Three proteins—streptavidin (SAV), maltose binding protein (MBP), and immunoglobulin G (IgG)—have been used for further functionalization of qdots (see text) and add to the final size of the qdot, in conjunction with the solubilization chemistry (Fig. 2).

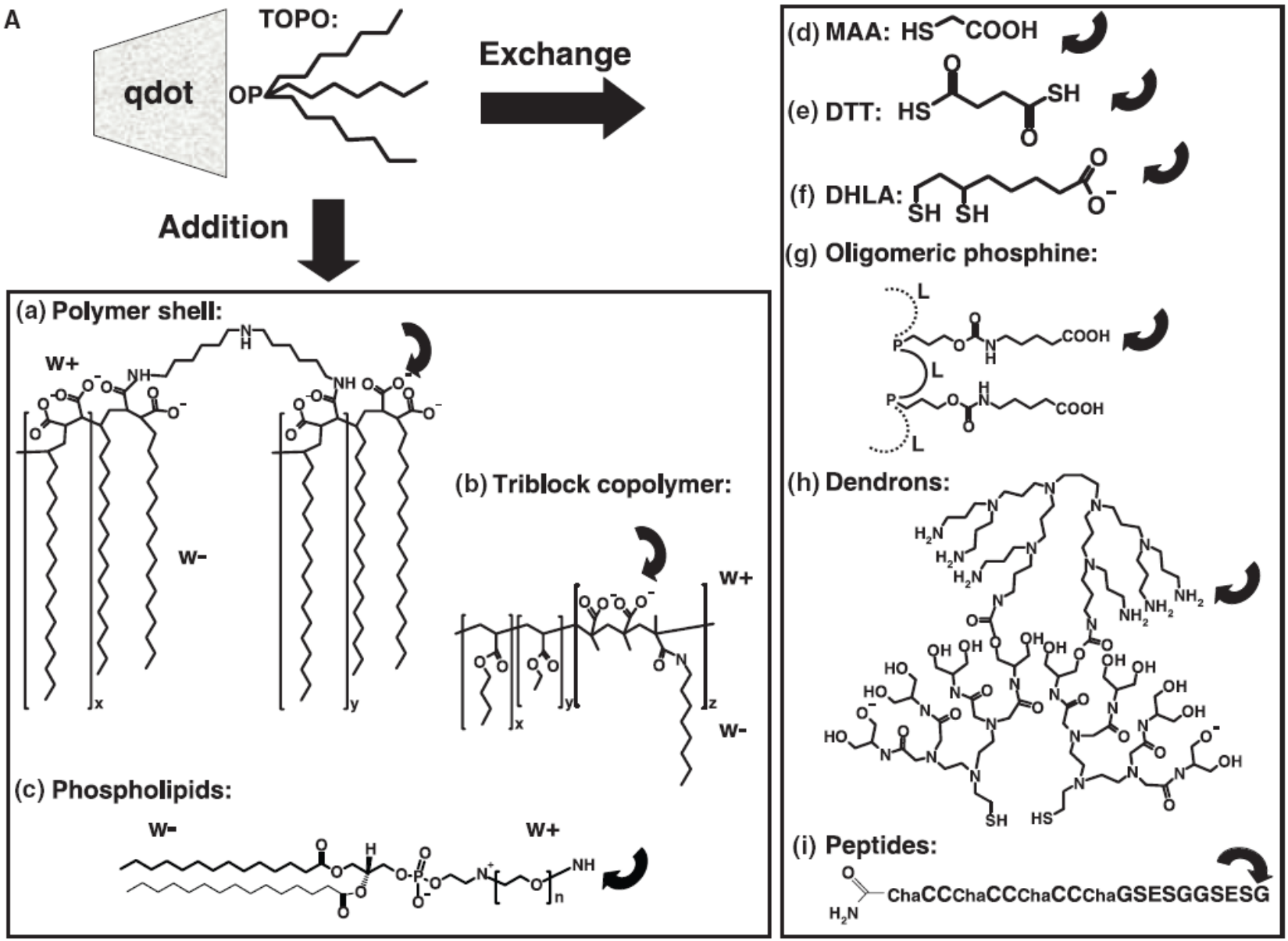
A
qdot
TOPO:
OP
Exchange
Addition
(a) Polymer shell:
W+
W-
(b) Triblock copolymer:
W+
W-
(c) Phospholipids:
W-
W+
(d) MAA: HS COOH
(e) DTT: HS SH
(f) DHLA: SH SH
(g) Oligomeric phosphine:
COOH
COOH
(h) Dendrons:
(i) Peptides:
ChaCCChaCCChaCCChaGSESGGSESG

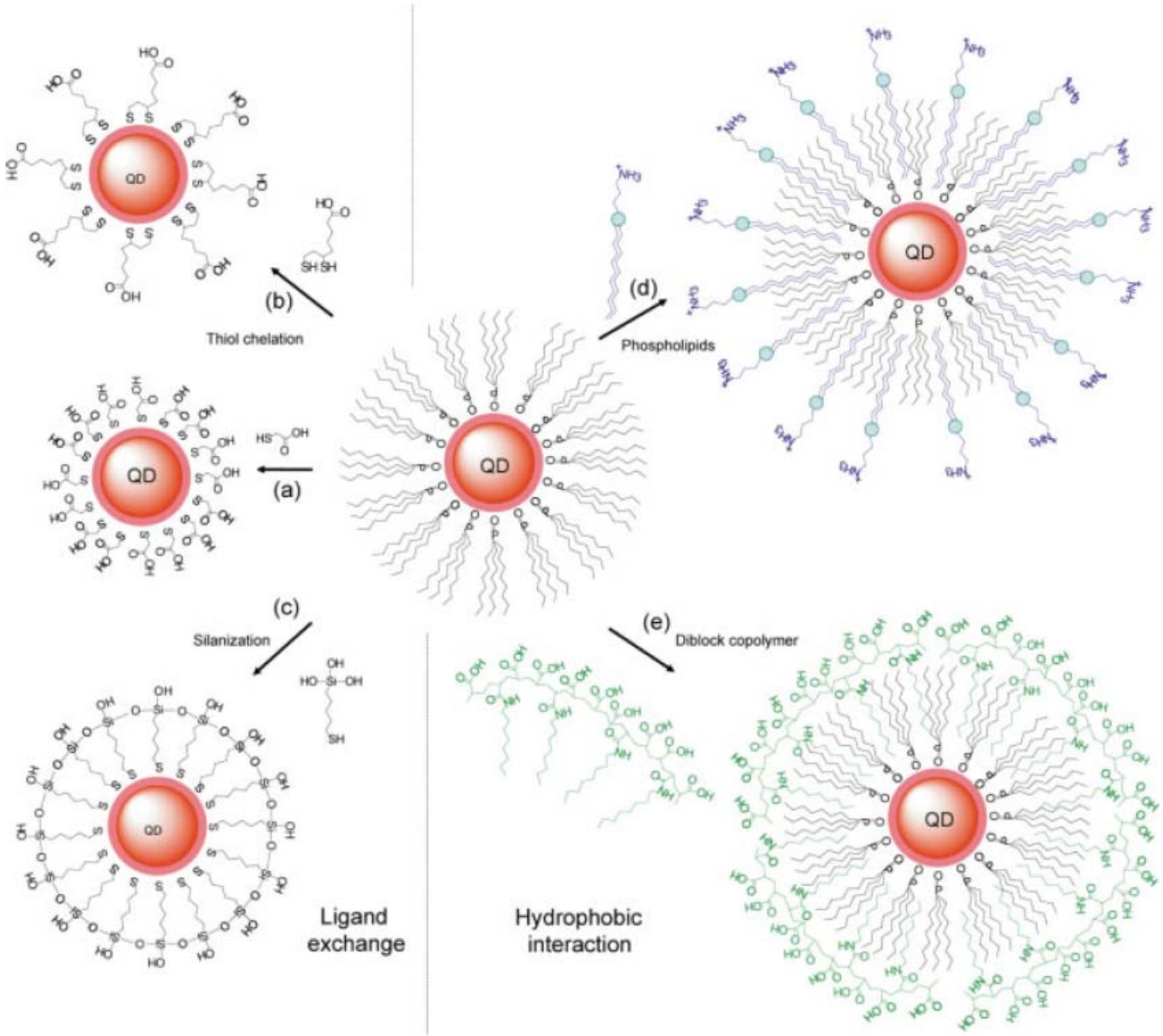
QD
(a)
(b)
Thiol chelation
(c)
Silanization
Ligand exchange
(d)
Phospholipids
(e)
Diblock copolymer
Hydrophobic interaction

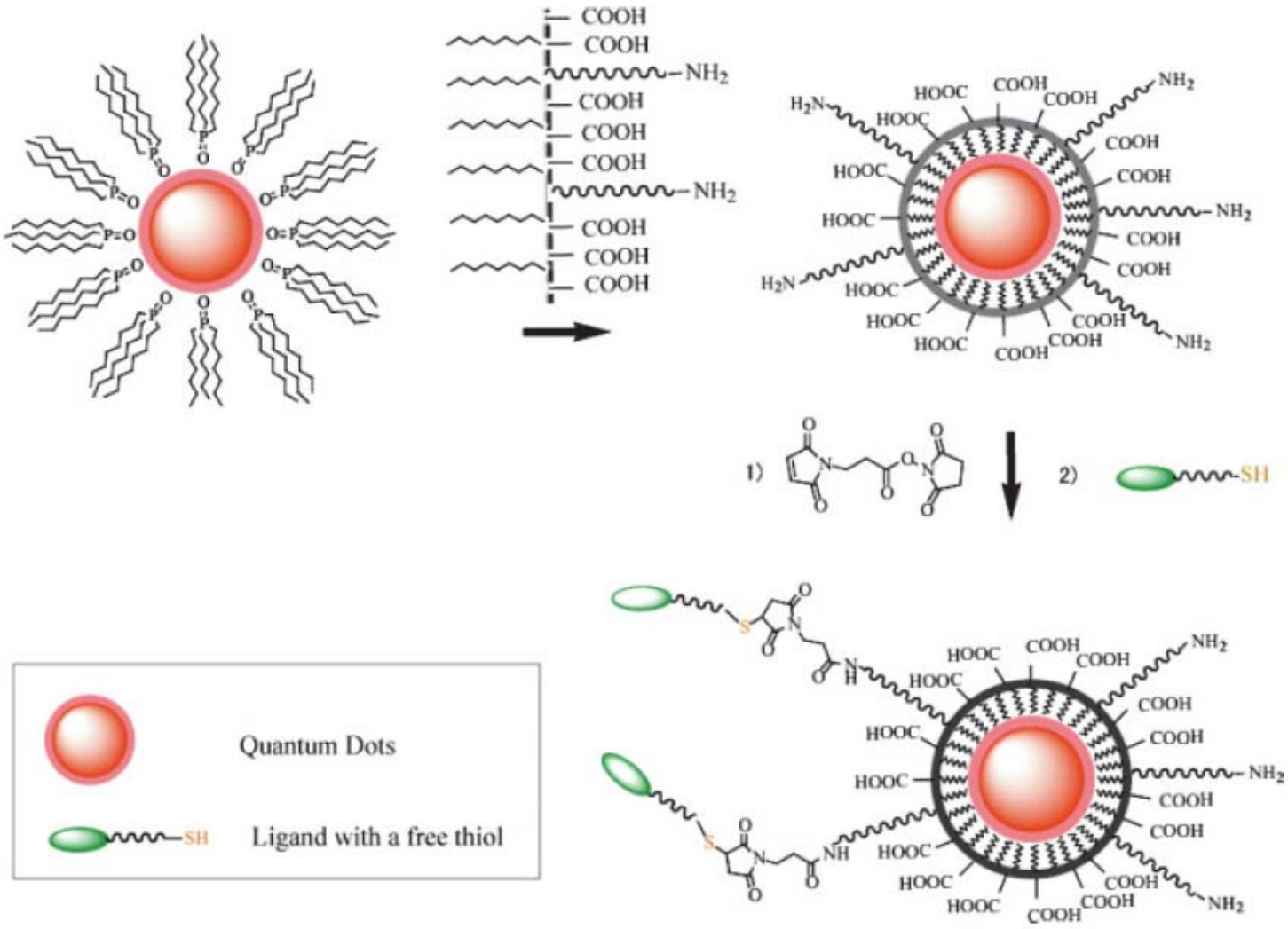

FIGURE 3 Maleimide functionalized QDs for conjugating thiol-containing ligands. TOPO stabilized QDs are coated with a primary amine functionalized tri-block amphiphilic copolymer for producing water-soluble QDs, which facilitate further conjugation to ligands with free thiols through bi-functional cross-linkers.

Cells incubated with tiopronin coated QDs

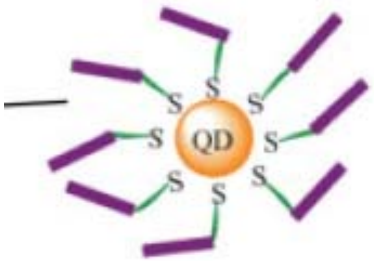

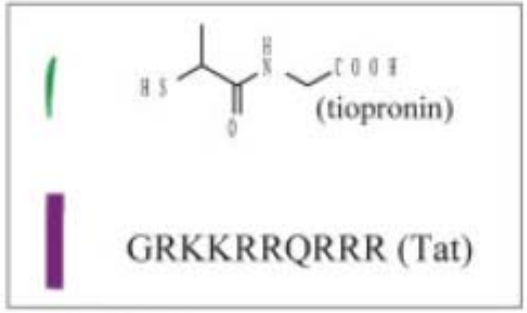

Cells incubated with Tat functionlized QDs

Scheme 1. Modular Design of Hydrophilic Ligands with Terminal Functional Groups Used in This Study

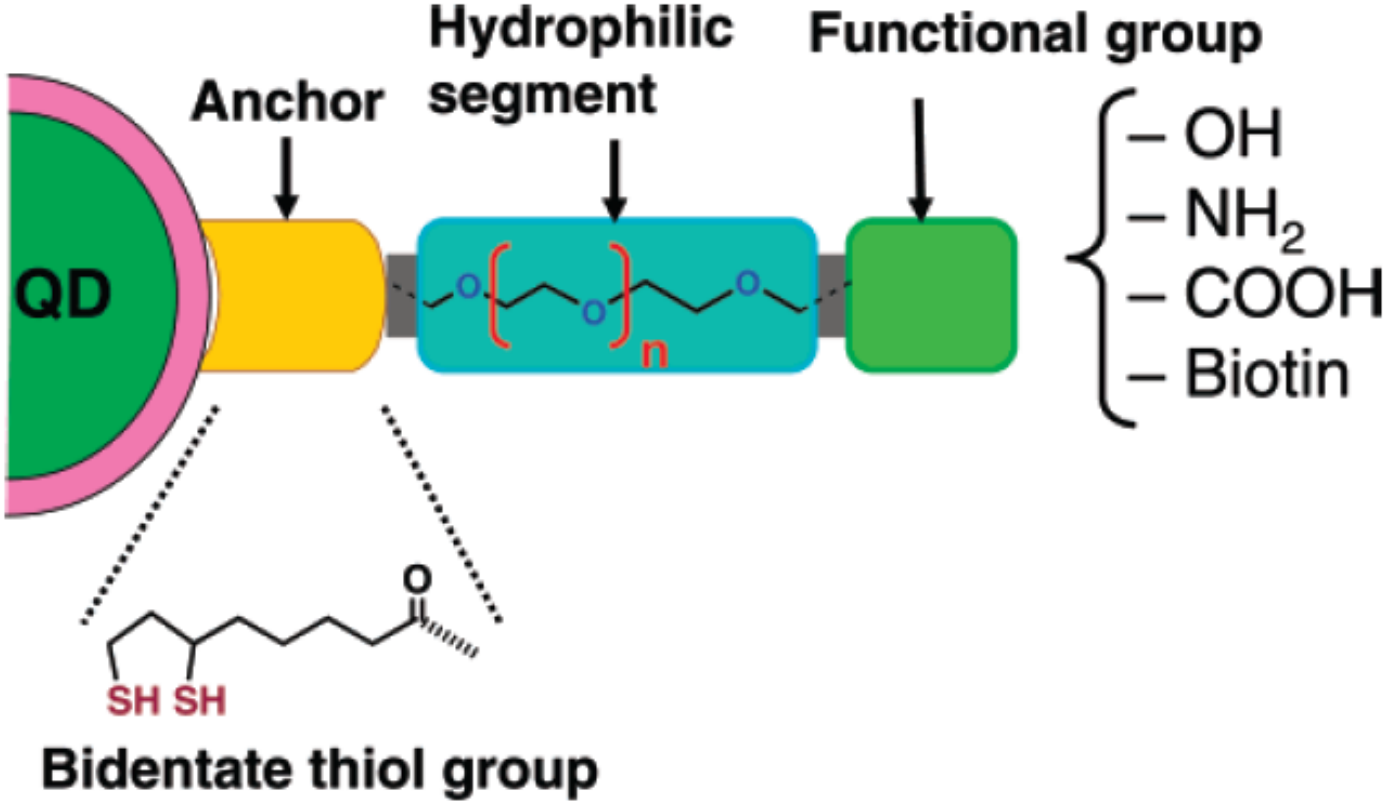

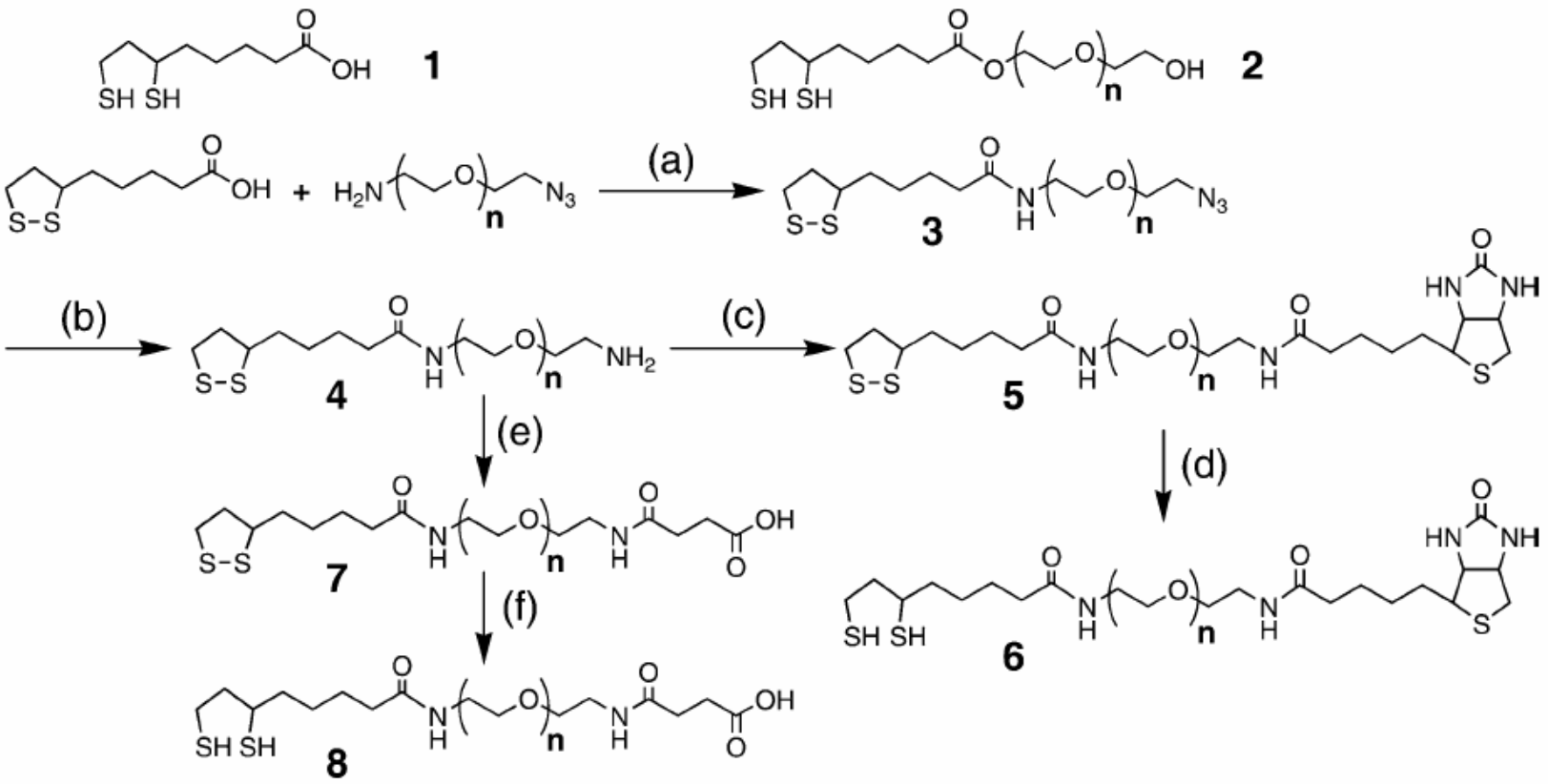

Figure 1. Chemical structures and synthetic routes of the surface ligands used in this study: (a) DCC, DMAP, CH_2Cl_2; (b) PPh_3, H_2O, THF; (c) biotin *N*-hydroxysuccinimide ester, Et_3N, DMF; (d) $NaBH_4$, EtOH, H_2O; (e) succinic anhydride, pyridine; (f) $NaBH_4$, EtOH, H_2O.